The Pennsylvania State University

The Graduate School

College of Engineering

CHARACTERIZATION OF VAPOR DEPOSITED

THIN FILMS OF MAGNESIUM AND MAGNESIUM ALLOYS

A Thesis in

Engineering Science and Mechanics

by

Robert Gresh

Submitted in Partial Fulfillment

of the Requirements

for the Degree of

Master of Science

August 2014

The thesis of Robert Gresh was reviewed and approved* by the following:

Barbara Shaw
Professor of Engineering Science and Mechanics
Thesis Advisor

Mark Horn
Professor of Engineering Science and Mechanics

Elizabeth Sikora
Research Associate, Engineering Science and Mechanics

Judith A. Todd
P. B. Breneman Department Head Chair
Professor of Engineering Science and Mechanics

*Signatures are on file in the Graduate School

ABSTRACT

Magnesium and magnesium-aluminum alloy thin films were created by physical vapor deposition using a dual gun electron beam physical vapor deposition (EBPVD) system for the purpose of evaluating their corrosion properties. A surface profilometer was used to measure the thickness of the films, which was then used to calculate the deposition rate. Energy dispersive x-ray spectroscopy (EDS) was used to determine the composition of thin films. The cross sections of thin films were analyzed using a field-emission scanning electron microscope (FESEM) to provide information about the structure and morphology of the films. X-ray diffraction (XRD) was used to measure the x-ray spectra of thin films and determine the phases and crystal structures present in the thin films. Electrochemical testing was conducted to determine the corrosion characteristics of the samples. The open circuit potential (OCP) was measured along with corrosion rates calculated from polarization resistance (PR) and electrochemical impedance spectroscopy (EIS) data.

Magnesium films were deposited with deposition rates ranging from 9.27 to 126.60 Å/s and angles from 0° to 38°. Magnesium films with low deposition rates (less than 20 Å/s) showed a denser morphology with columns of 500-700nm diameter and a preferred orientation to the (0002) plane of the hcp magnesium structure. Higher deposition rates (40 to 126 Å/s) for magnesium films resulted in a less dense morphology with thin columns of 200-300nm diameter and a preferred orientation of the (103) plane for hcp magnesium crystal structure. The magnesium-aluminum films were produced using the two gun system with deposition rates ranging from 14.42 to 34.58 Å/s and with compositions ranging from 2.97 to 58.71 wt. % Al. The best Mg-Al film had an open circuit potential of -1.856 V and a corrosion rate of 5.85 mpy. These characteristics make this film an ideal candidate for a protective coating.

TABLE OF CONTENTS

LIST OF FIGURES

LIST OF TABLES

ACKNOWLEDGEMENTS

encouragement and prayers. Thanks to my grandparents and the rest of my family for simply being the best family in the world.

I would like to thank God for blessing me with all of the people mentioned above and for giving me the strength and wisdom that I need each day.

Chapter 1

Introduction

1.1 Problem Statement

Magnesium-aluminum alloys are of interest due to the high strength-to-weight ratio and electrical properties of the alloys. Thin film Mg-Al alloys can be produced and tested at varying thicknesses and compositions using Electron Beam Physical Vapor Deposition (EBPVD). Collecting data on the properties of these films could lead to further research and applications as a protective coating.

1.2 Design Needs

Magnesium is a lightweight structural material and a very active metal. Because it is active, it rapidly corrodes in many applications and must be protected to increase the lifetime of magnesium components. One way to reduce the corrosion rate is to alloy magnesium with metals that are more resistant to corrosion. Aluminum is a desirable element to alloy with magnesium because it can increase corrosion resistance by enhancing the performance of the protective oxide that forms on the surface of the material during corrosion, while allowing magnesium to retain its mechanical properties. Different concentrations of alloying material can change the way the resulting film grows and thus the structure of the film. As a result, properties of alloys with different compositions can vary significantly.

Once created, Mg alloy thin films were characterized to determine thickness, surface morphology, microstructure, and electrochemical properties pertaining to the corrosion rate. The goal is to produce an alloy with a uniform surface morphology and microstructure that can be used to protect structural components from corrosion. Electrochemical testing was conducted using a potentiostat to measure open circuit potential, Polarization Resistance and Electrochemical Impedance Spectrum. A profilometer was used to measure thickness quickly and accurately. Energy Dispersive X-ray Spectroscopy was used to measure the composition of the films, Scanning Electron Microscopy was used to analyze surface morphology while crystal structure was examined using X-Ray Diffraction.

1.3 Objective

The objective of this research was to develop a magnesium-aluminum thin film that acts as a protective coating to slow down corrosion of magnesium structural materials. EBPVD was used to produce different films by varying deposition parameters. These films were characterized to gain an understanding of how the EBPVD parameters control film growth and how the different film properties affect the electrochemical properties of the film.

Chapter 2

Literature Review

2.1.1 Magnesium Introduction

Magnesium exhibits a useful combination of properties as a lightweight structural material. It has been used for decades in structural components of aircraft because of its lightweight and high specific strength. Despite the high specific strength, low density and cheap cost of magnesium, it has not been widely used in applications that don't have strict weight limitations because it is highly susceptible to corrosion. Recently, interest in magnesium has risen as fuel emission restrictions have been increased on automobiles because using magnesium can increase fuel efficiency by decreasing the weight of the vehicle [1]. Techniques that reduce corrosion on magnesium are used to increase the lifetime of magnesium structural members and make them more cost efficient. In this section, properties of magnesium and corrosion protection techniques are reviewed.

Magnesium is the 8th most common element on earth and as such it is readily available and inexpensive. A list of advantages and disadvantages was created by B. L. Mordlike and T. Ebert in their article *Magnesium: Properties – Applications – Potential*:

Table 2-1 Advantages and Disadvantages of Magnesium and Magnesium Alloys. Advantages and disadvantages taken from Mordlike et al. [1].

Advantages and Disadvantages of Magnesium and Magnesium Alloys	
Advantages	**Disadvantages**
- lowest density of all metallic constructional materials; - high specific strength; - good castability, suitable for high pressure die-casting; - can be turned: milled at high speed; - good weld ability under controlled atmosphere; - much improved corrosion resistance using high purity magnesium; - readily available; - compared with polymeric materials: - better mechanical properties; - resistant to ageing; - better electrical and thermal conductivity; - Recyclable.	- low elastic modulus; - limited cold workability and toughness; - limited high strength and creep resistance at elevated temperatures; - high degree of shrinkage on solidification; - high chemical reactivity; - in some applications limited corrosion resistance

The disadvantage of magnesium that this thesis addresses is the limited corrosion resistance, which is due in part to magnesium's electrochemical potential being lower than that of other structural materials. Pure magnesium is rarely used in structural applications because it is so susceptible to corrosion. Alloying magnesium with other metals allows its strength properties to be retained while decreasing its corrosion rate resulting in a significantly increased lifetime. The elements that are most commonly alloyed with magnesium are aluminum, zinc, rare earths, manganese and lithium.
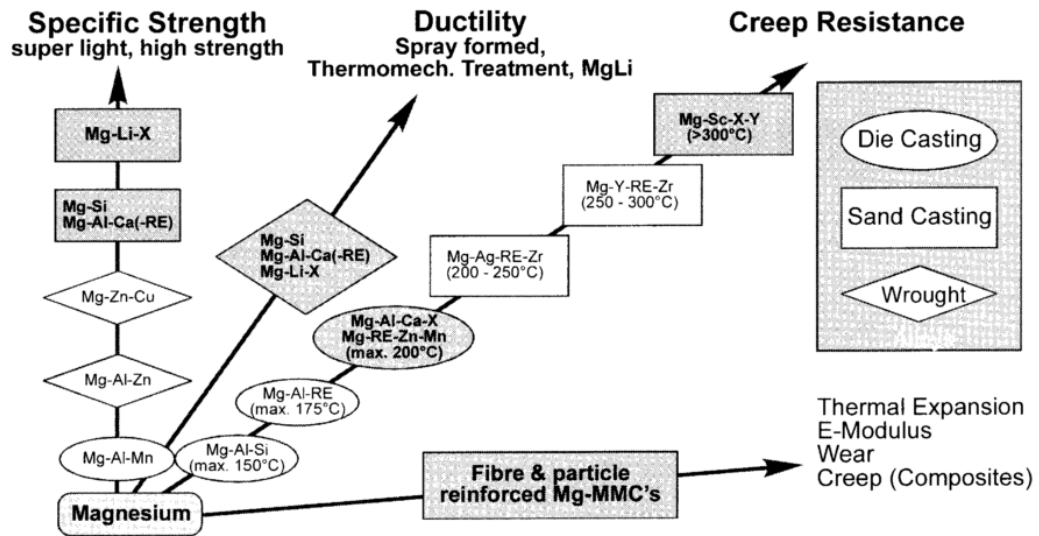
Figure 2-1 Magnesium Alloys by Formation and Properties [1]

Alloying aluminum with magnesium improves the castability, strength properties and

corrosion resistance, while decreasing creep resistance and ductility. Figure 2-1 shows some of

the directions of magnesium alloy development of sand-cast, wrought, and die-cast alloys. The

most common structural magnesium alloy is AZ91 (90% Mg-9% Al- 1% Zn); as it exhibits

improved corrosion resistance, maintains high strength and is easily die-cast [2] [3]. Even with its

improved corrosion resistance, AZ91 is susceptible to corrosion and should be protected from

harsh environments. Alloying materials must be high in purity as even a small amount of iron,

nickel, or copper can significantly increase the corrosion rate of magnesium and magnesium

alloys. Conversely, adding a small amount of manganese to a magnesium alloy can help to

increase resistance to stress corrosion cracking [4].

2.1.2 Magnesium Structure

The crystal structure of pure magnesium metal is hexagonal close-packed (hcp). The primary slip planes of magnesium are (0001) and (1120), and the secondary slip planes are (1010), (1120), (1011) and (1120) [5] [6] [7] [8]. Bulk magnesium alloys nearly all exhibit this hcp crystal structure [1]. Because of this hcp structure, magnesium has very limited ductility.

In pure magnesium thin films grown on a (111) polished silicon substrate, X-Ray Diffraction (XRD) reveals a strong peak of the (0002) plane, which corresponds to an hcp structure.
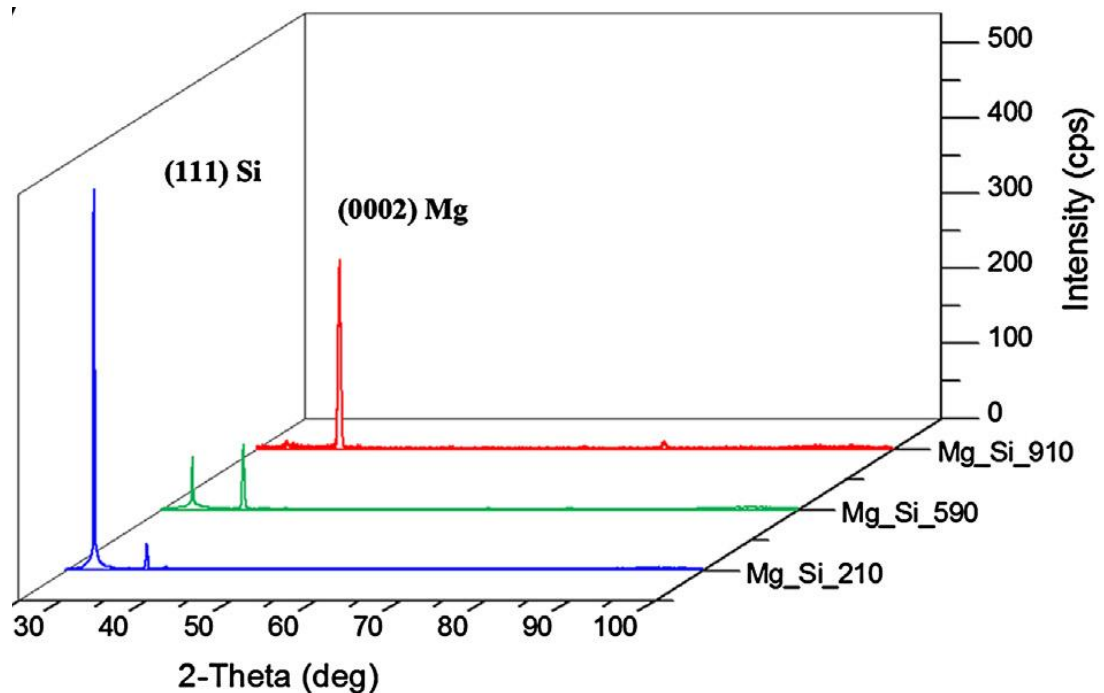
Figure 2-2 X-Ray Diffraction Patterns of pure magnesium deposited on (111) polished silicon using RF magnetron sputtering. Three films are shown with thickness of 210nm, 590nm, and 910nm [8].

Research performed by Kanagasundar Appusamya et al. [8] showed that (0002) tended to dominate pure magnesium thin films with increasing film thickness. The x-ray diffraction

patterns for pure Mg thin films are shown in Figure 2-2. They also found that the grain size

increased with increasing film thickness [8]. A study by C. Blawert et al. [9] showed similar

findings. Blawert compared the diffraction patterns of films deposited via DC Magnetron

Sputtering (MS), Ion Beam Sputtering (IBS) and Vacuum Arc Deposition (VAD). A 3-micron

pure magnesium thin film was deposited using each method. In each case, the (002) magnesium

peak dominated and the hexagonal magnesium phase was the only phase found in the film

(Figure 2-3).
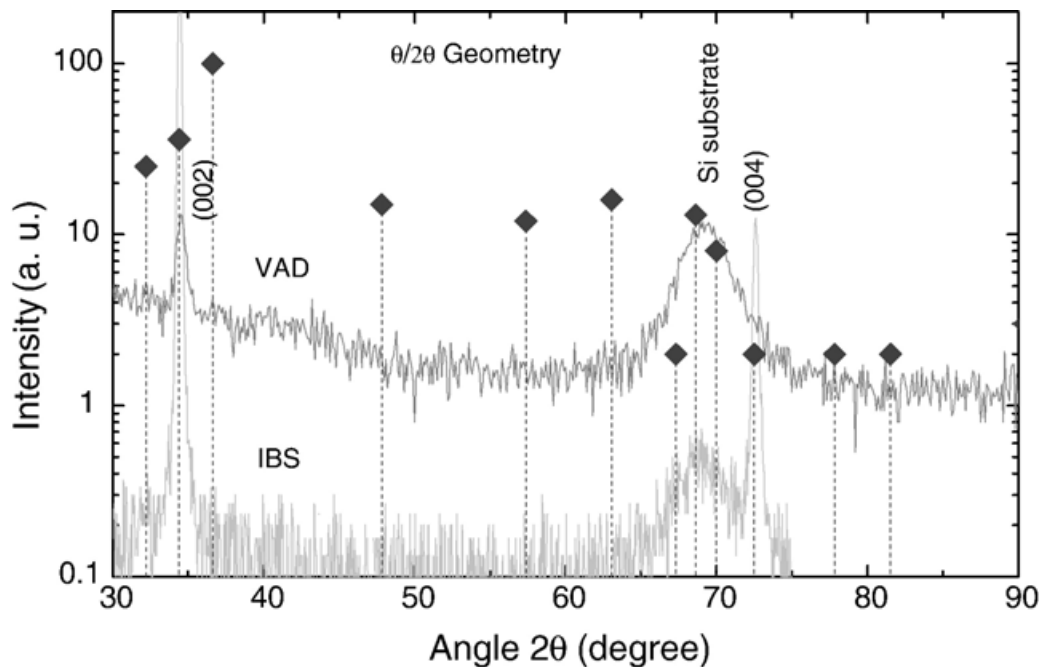
**Figure 2-3 XRD spectra measured in Bragg–Brentano geometry. The
diamonds represent expected geometries for magnesium. Films were prepared by
Vacuum Arc Deposition (VAD) and Ion Beam Sputtering (IBS). The (002) and (004)
peaks dominate the pattern [9].**

Research by Sean Pursel et al. [10] showed the same trend. Magnesium was deposited onto a glass substrate using Electron Beam Physical Vapor Deposition (EBPVD). The resulting thin films showed a preferred orientation of the (002) plane.
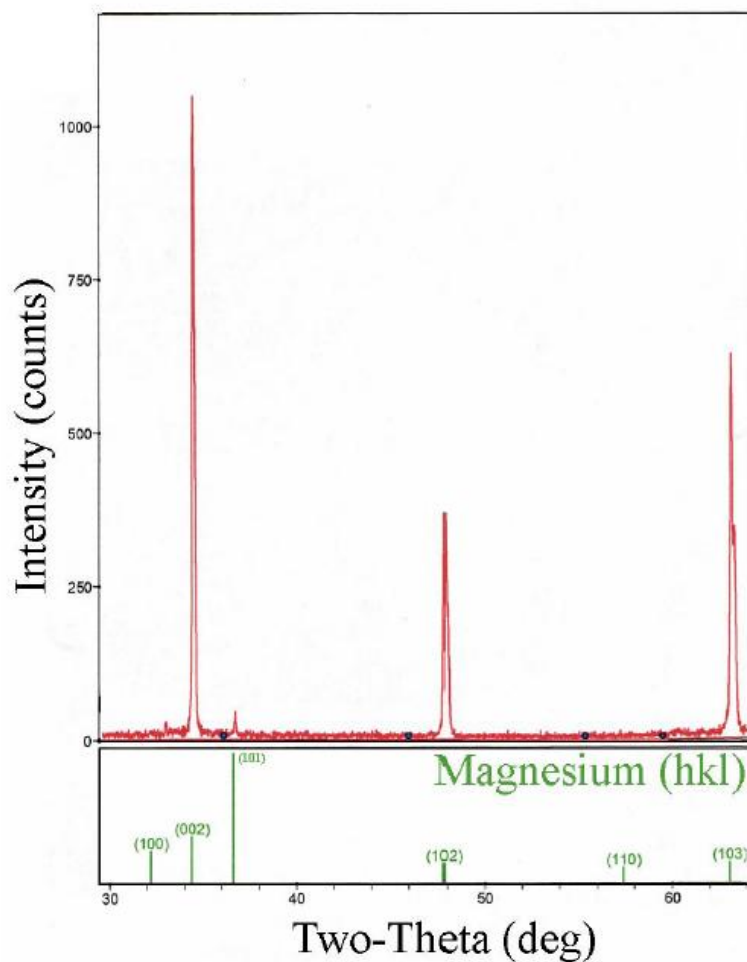
Figure 2-4 XRD pattern of a pure magnesium thin film deposited onto a glass substrate using EBPVD [10].

Stormer et al. [11] performed research on pure magnesium thin films deposited via magnetron sputtering onto silicon substrates. Films were grown at different angles to a thickness of 3μm. XRD was then performed on the films to determine the crystal structure. All of the films exhibited an hcp crystal structure. Films had a strong (002) diffraction peak and the line intensity decreased with increasing deposition angle as shown in Figure 2-5. Potentiodynamic polarization

was used to determine the corrosion potential and corrosion rate. The corrosion rates and corrosion potentials measured were significantly lower (335.1 to 537μm/year and -1736 to -1880mV) for the thin films than for the target material (1421μm/year and -1539mV). Trends showed that an increase in deposition angle or pressure lead to a decrease in the corrosion potential and an increase in corrosion rate and surface roughness. A film deposited at an angle of 0° and 0.2Pa had a corrosion rate of 335.1μm/year and a corrosion potential of -1735mV. A film deposited at 70° and 0.2Pa had a corrosion rate of 531.9μm/year and a corrosion potential of -1867.7mV. The increase in corrosion rate is due to an increase in surface area due to the increased roughness of the film. The shift in corrosion potential cannot be explained by an increase in surface area, "the decrease of the potential might be the result of the much finer microstructure of the coatings (column diameter ~0.5μm), with a large number of disturbed grain boundaries exposed to the electrolyte [11]."
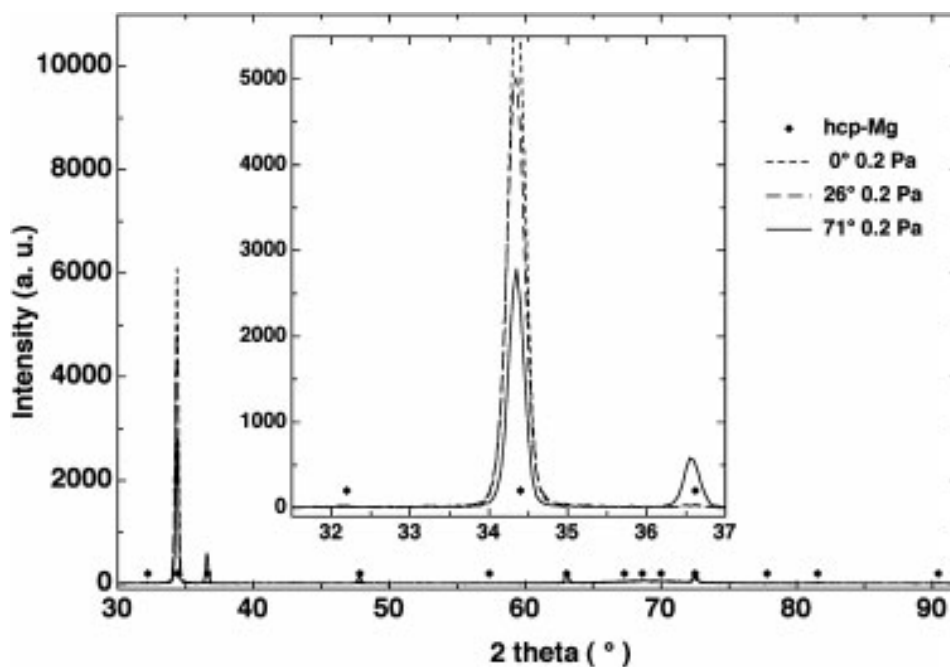
Figure 2-5 X-Ray Diffraction patterns of pure Mg thin films prepared by magnetron sputtering at 0.2 Pa in Ar and at varying deposition angles. The (002) peak decreases with increasing deposition angle. Figure from [11].

2.1.3 Magnesium Scanning Electron Microscopy

Scanning Electron Microscopy (SEM) was used to image bulk materials as well as thin film samples. Scanning Electron Microscopes are capable of magnifications of over 200,000 times, which allows for the observation and analysis of the microstructure of the morphology and growth characteristics of a sample.

Pursel studied the effects of substrate temperature on the structure and growth of pure Mg thin films deposited with EBPVD [10]. He found that the Mg films deposited at room temperature showed a very preferential growth normal to the substrate. Deposition at 160 °C resulted in a reduced sticking coefficient and a very thin film. Growth being quenched at -80 °C resulted in a less preferred orientation with planes pointing in many different orientations. This is due to decreased surface mobility which results in greater effects from shadowing during deposition.
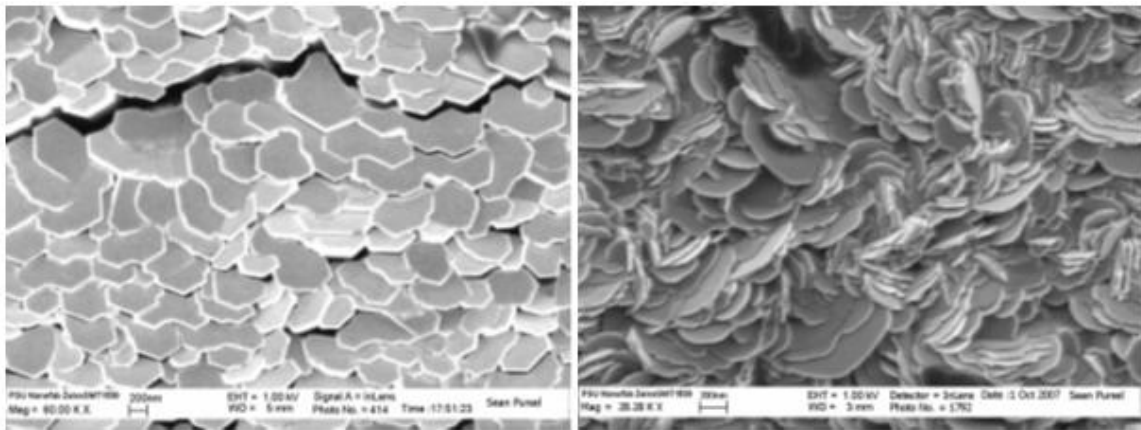
Figure 2-6 Top down FESEM images of pure Mg thin films. The left image is of a film grown at room temperature. The film on the right was deposited with quenched growth at -80 °C. [10]

Pictures of thin films were taken as they were deposited at 10Å/s with deposition time of up to 2 minutes. A pure Mg thin film showed 3D nucleation as it grew. A Mg-Y-Ti alloy showed 2D nucleation, which results in a more uniform growth, a more uniform film structure, and fewer voids. This uniform structure results in a more uniform corrosion mechanism and a lower corrosion rate.
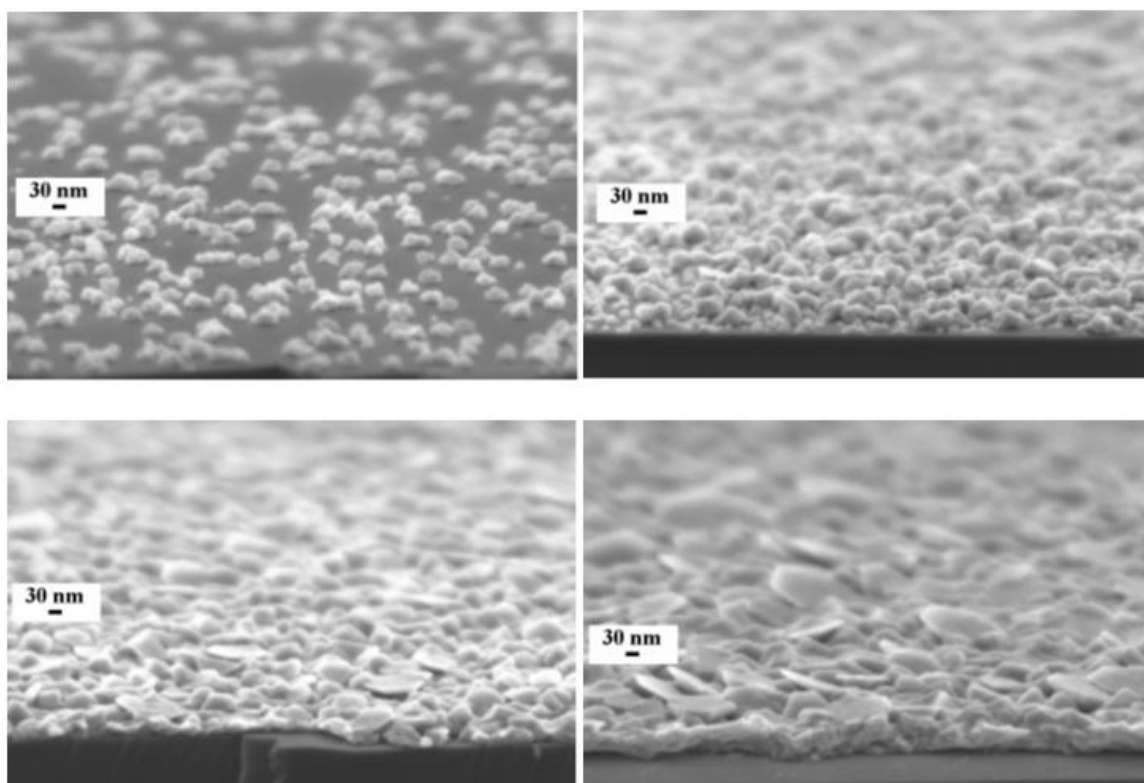
Figure 2-7 Cross-Sectional images of a pure Mg deposition. The pictures were taken with increasing deposition time from the top left to the bottom right. The film was deposited at 10A/s for 2 minutes. [10]

Pure Mg thin films tend to grow in columns or nanoblades. These nanoblades have an hcp structure and tend to grow facing the direction of the Mg vapor flux during deposition. Depending on the angle of deposition, the nanoblades will grow at an angle and be subject to self-shadowing of other blades as the film grows. Yuping He and Yiping Zhao studied this behavior by depositing Mg at an angle of 80° on to a flat, fixed (non-rotating substrate). Films were grown at a fixed rate of 50Å/s to a thickness of 5µm. During deposition, the surface mobility and self-shadowing compete with one another. Shadowing leads to the formation of columns parallel to the direction of vapor flux. These columns or "nanoblades" can be clearly observed in Figure 2-8. Surface mobility promotes the formation of a structure aligned with the substrate normal [12].
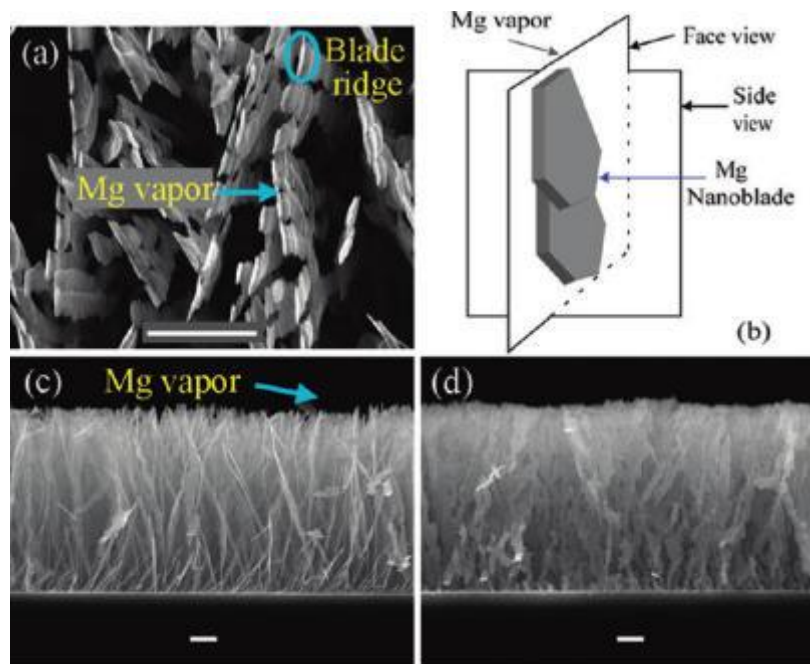
Figure 2-8 SEM images of a pure Mg film deposited using Oblique Angle Deposition. (a) Top down SEM image that shows the edge of a Mg nanoblade; (b) shows the hexagonal shape of the Mg nanoblades and the side view and face view orientations of pictures (b) and (c), (c) side view and (d) face view SEM images [12].

Blawert deposited pure Mg using DC Magnetron Sputtering (MS), Ion Beam Sputtering (IBS) and Vacuum Arc Deposition (VAD). For the MS formed film, the surface was very rough and the hexagonal structure of magnesium can be clearly observed on the surface (Figure 2-9). For the IBS film, the hexagonal structure can still be observed, but the surface is smoother and the hexagonal shape cannot be seen as clearly. The VAD film did not exhibit the hexagonal surface structure and was the smoothest of all the films. This corresponds to a change from columnar film growth to layer-by-layer growth with increasing average ion energy. The average energy per deposited particle increases from 5–10 eV for MS to 8–15 eV for IBS to 15– 45 eV for VAD [9]. Corrosion rate measurements were taken using potentiodynamic polarization in 0.5% NaCl solution at a pH of 11. Blawert concluded that, "MS and IBS with similar surface roughness have similar corrosion rate of 260 and 293 μm/year while the smoother VAD specimen has only 144 μm/year, suggesting that this is most likely a roughness and no texture effect." However, the corrosion potential for each method was measured to be -1725mV ±20 mV. This is 200mV lower than as-cast Mg and is likely caused by the preferred orientation of the thin films.
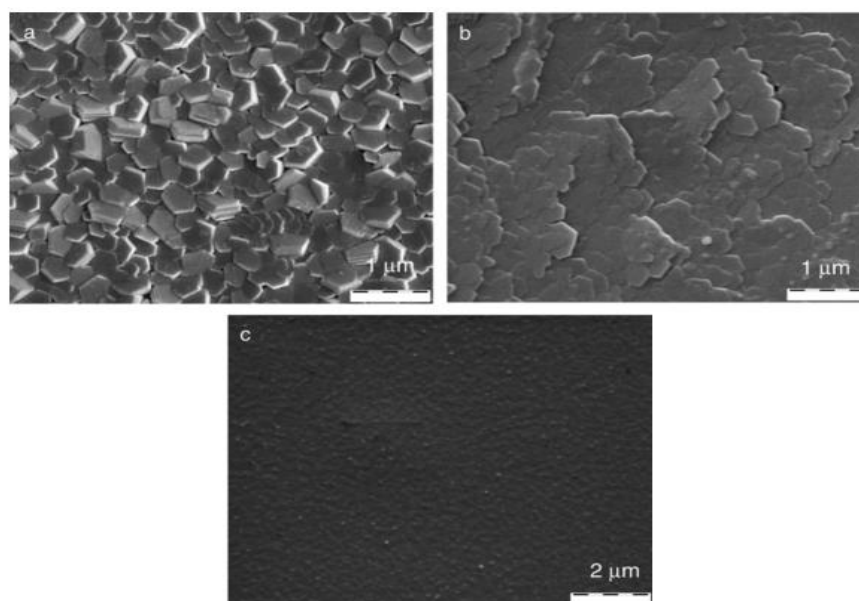
Figure 2-9 Top down view of pure Mg films deposited by (a) MS, (b) IBS, and (c) VAD. Image from C. Blawert [9].
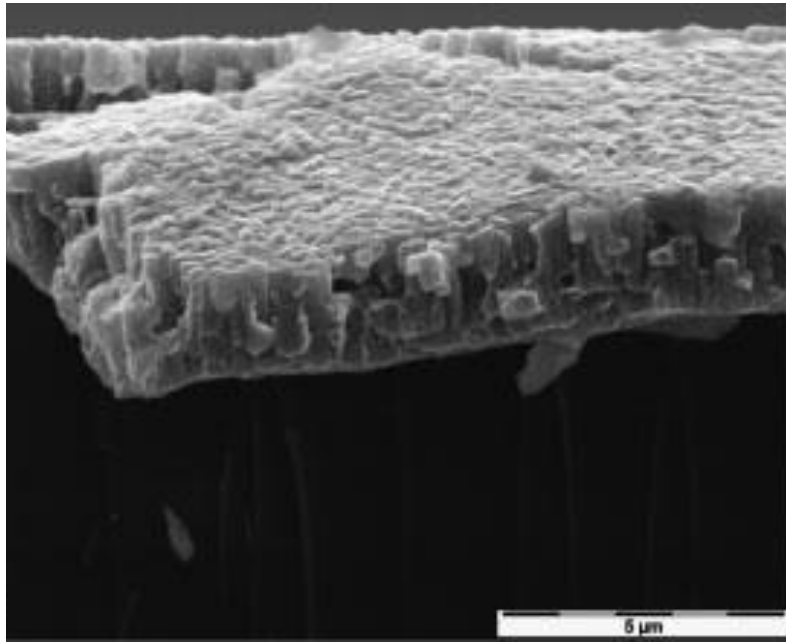
Figure 2-10 SEM image of the cross-section of a 3μm thick pure Mg thin film deposited by magnetron sputtering at a deposition angle of 0° and a pressure of 0.2 Pa. The columnar growth can be seen. Image from [11].

M. Stormer et al. found that thin films deposited by magnetron sputtering in a 0.2 Pa low pressure argon atmosphere at about 12Å/s at an angle of 0° lead to a columnar growth of the thin film. Films were grown to a thickness of 3μm [11]. The films were not dense and had voids due to shadowing effects. This structure, pictured in Figure 2-10, is typical of a low-temperature deposition described in the structure zone model. The low temperature does not allow the adatoms to diffuse during deposition and leads to the columnar growth seen in Figure 2-10.

The structure zone model is used to describe growth mechanisms of thin films [13]. The model is organized by T/T_m, where T_m is the melting temperature of the source material. At low temperature, $T/T_m < 0.1$, the growth is dominated by atomic shadowing and the structure consists of thin, isolated columns. For T/T_m between 0.1 and 0.3, surface diffusion is increased and the structure consists of columnar grains. Zone 3, which is T/T_m of 0.3 to 1.0, the surface diffusion is

rapid and grain boundaries and dislocations are mobile. In Zone 3, the recrystallization and grain growth become important.

2.2.1 Aluminum

Aluminum is the third most abundant element in the earth's crust and the most abundant metallic element in the earth's crust [14].Although it is abundant on earth, aluminum is rarely found in nature in its elemental state because it is highly reactive. In nature, it exists almost entirely in mineral compounds. Aluminum was discovered in 1825 by Hans Christian Oersted in an impure form. In 1827, aluminum was isolated by Friedrich Wohler by extracting pure aluminum from aluminum chloride. For the next 60 years, aluminum was a more valuable and rare metal than gold or silver because it was so expensive to fabricate. In the 1880s, the Hall-Heroult process was developed independently by Charles Mart Hall and Paul Heroult. The Hall-Heroult process allows for the extraction of aluminum by dissolving alumina, Al_2O_3, in molten cryolite, Na_3AlF_6, and then by electrolyzing so that aluminum collects at the cathode.

Since the development of the Hall-Heroult process, aluminum has become a major engineering material (Figure 2-11). Aluminum has a density of 2.7 g/cm^3. This makes it among the lightest engineering material as it is significantly less dense than steel, which has a density of 7.83 g/cm^3. In addition to being lightweight, aluminum demonstrates a variety of useful properties including reflecting visible light, radiant energy, heat waves, and electromagnetic waves; it can also absorb these waves if it is anodized. Aluminum can be a good electrical and thermal conductor, but it can be alloyed to have high electrical resistance. Aluminum is also nonferromagnetic, nonpyrophoric and nontoxic, all desirable properties.

Aluminum has more than three hundred commercial alloy compositions and even more variations exist in specialized applications. Aluminum is easily incorporated in wrought or cast alloys and these alloys often strengthen some of aluminums many desirable properties. The majority of aluminum is used as wrought alloys which include foil, extrusions and rolled plate. Cast aluminum alloys have a low melting point and are easy to form, but are often limited by

their low tensile strength. Aluminum alloys are typically used as a structural material where lightweight is desired, because aluminum's only mechanical advantage over steel is its lightweight. Therefore, aluminum is often used in aerospace, cycling and automotive applications where reducing weight can increase the efficiency of the vehicle.
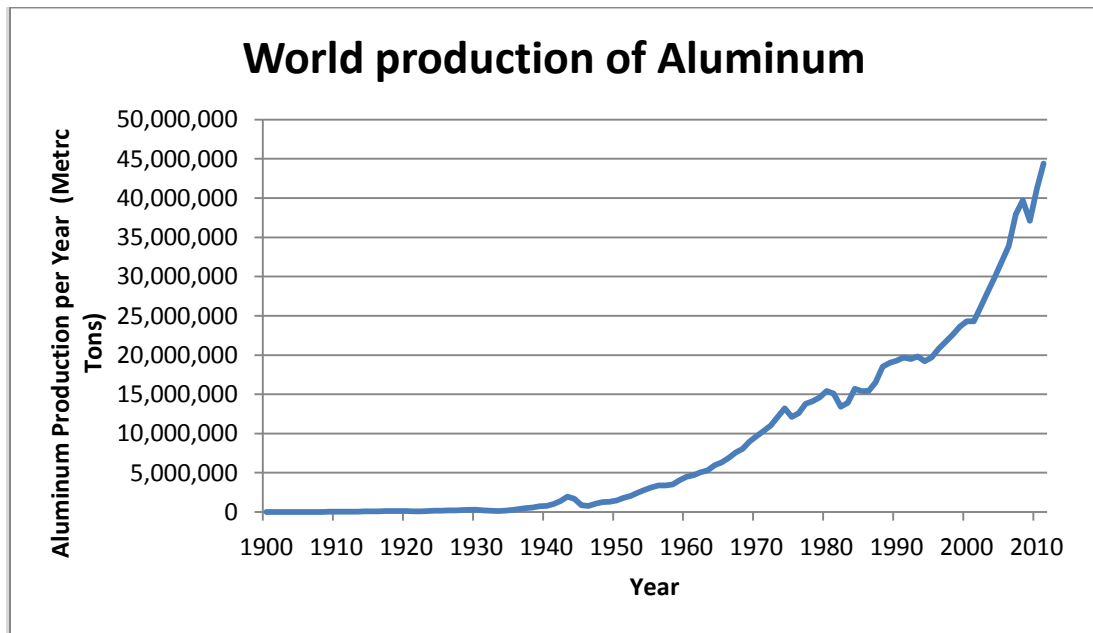
Figure 2-11 World Production of Aluminum (data from U.S. Geological Survey [15]).

2.2.2 Aluminum Microstructure

Aluminum exhibits a face-centered cubic (fcc) crystal structure with a slip plane and twinning plane in the (111) orientation [16]. Y. Xiong et al. created aluminum thin films using plasma assisted atomic layer deposition (a form of CVD). These films were deposited onto glass and p-Si substrates. Xiong was interested in the electrical resistivity of the films and they found that in order to get low resistivity it was important to anneal the sample to get an enlarged crystal size. The pure Al films showed the (111), (200), (220) and (311) planes, which are characteristic of an fcc crystal structure (Figure 2-12).
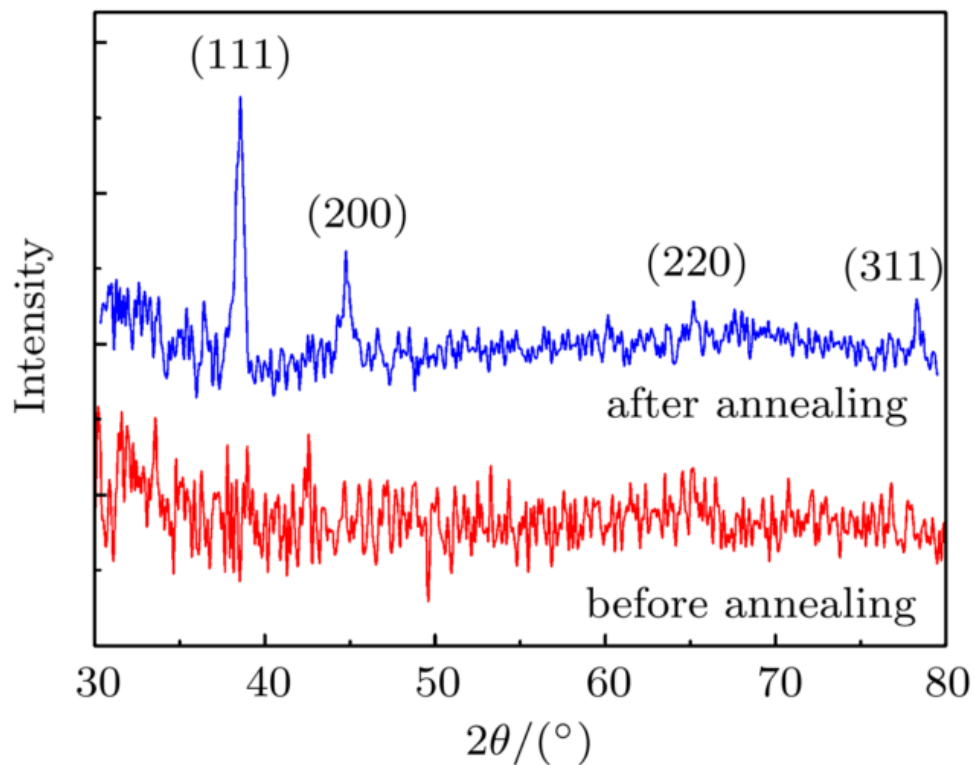
Figure 2-12 XRD spectra taken from a pure Al film deposited via plasma assisted atomic layer deposition. The pattern is characteristic of a face-centered cubic crystal structure [17].

Arthur J. Learn wrote a review of aluminum metallization for use with silicon devices. He compared several physical vapor deposition methods and found that aluminum could be used in silicon devices with the primary concern being the corrosion protection of aluminum. Aluminum was found to be suitable for deposition methods and provided good adhesion and electrical properties [18].
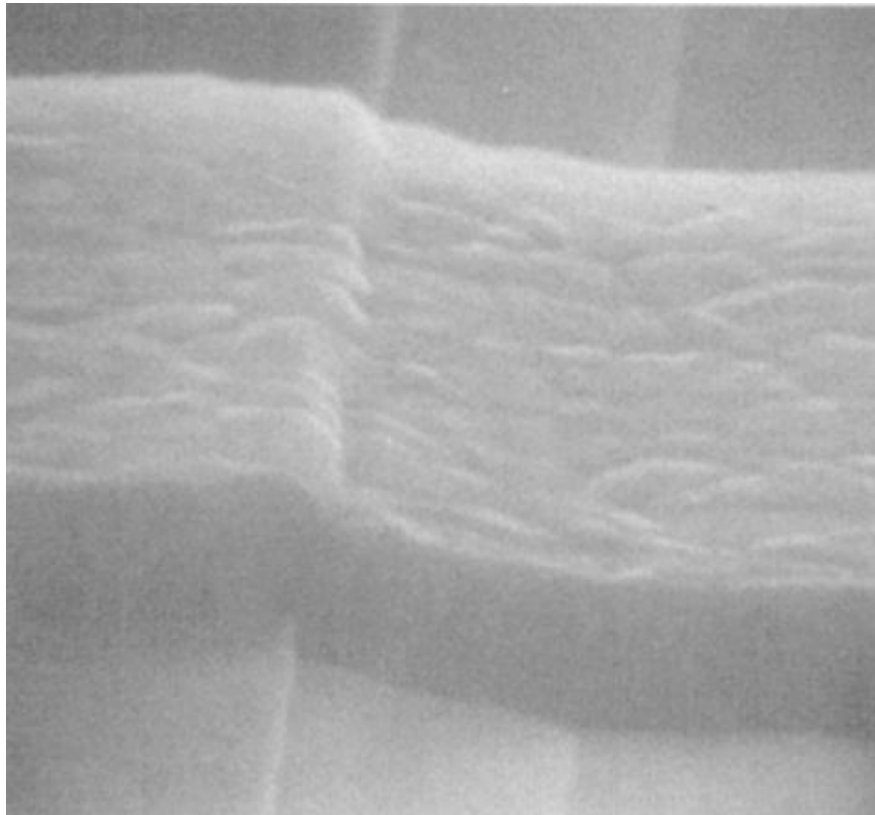
Figure 2-13 Pure Aluminum deposited on a silicon substrate at 300C [18].

2.3 Magnesium Alloys

Magnesium is not generally found in structural applications in its pure form. Most of Mg used in industry is alloyed with other metals. Aluminum is the most popular metal to alloy with Mg due to its low density, availability, and positive effects on the corrosion and strength properties [1] [19] [20] [21]. Zn is also frequently alloyed with Mg due to its similar properties, which include being very active and having a hexagonal close-packed (hcp) crystal structure. The Mg alloys are used as structural components in aircraft and high performance automobiles, where weight is a major factor in design. In these applications safety is important and as a result the condition of these structural members must be closely monitored. Magnesium is very susceptible to corrosion and many of its alloying elements help to protect it and increase the lifetime of the material.

2.3.1 Bulk Magnesium Alloys

The corrosion behavior of magnesium alloys can be improved by reducing the concentration of impurities such as iron, copper, and nickel. AZ91D is one of the most common Mg-Al alloys and it has been found that phases such as Al_8Mn_5 and Al_6Mn have a negative impact on the performance on these films, while the β-$Mg_{17}Al_{12}$ phase acts as a corrosion barrier [22].

S.S. Cho et al. compared three binary Al-Mg alloys with 5, 15 and 30 atomic percent magnesium. Ingots were prepared by melting the pure metals together in the desired proportions. Composition was then confirmed with chemical analysis [23]. X-ray diffraction patterns of the Al-Mg ingots are shown in Figure 2-14. All of these patterns show diffractions peaks from the α-Mg and β- $Mg_{17}Al_{12}$ phases. S.S Cho et al. analyzed the x-ray diffraction patterns and found that the α-Mg peaks are consistent with a hexagon close-packed structure with lattice parameters of a=0.3203nm, c=0.5203nm,and c/a =1.624. The β-$Mg_{17}Al_{12}$ phase peaks were consistent with a cubic structure with a=1.063nm. As Al content increased the amount of β-$Mg_{17}Al_{12}$ phase present in the ingot increased.
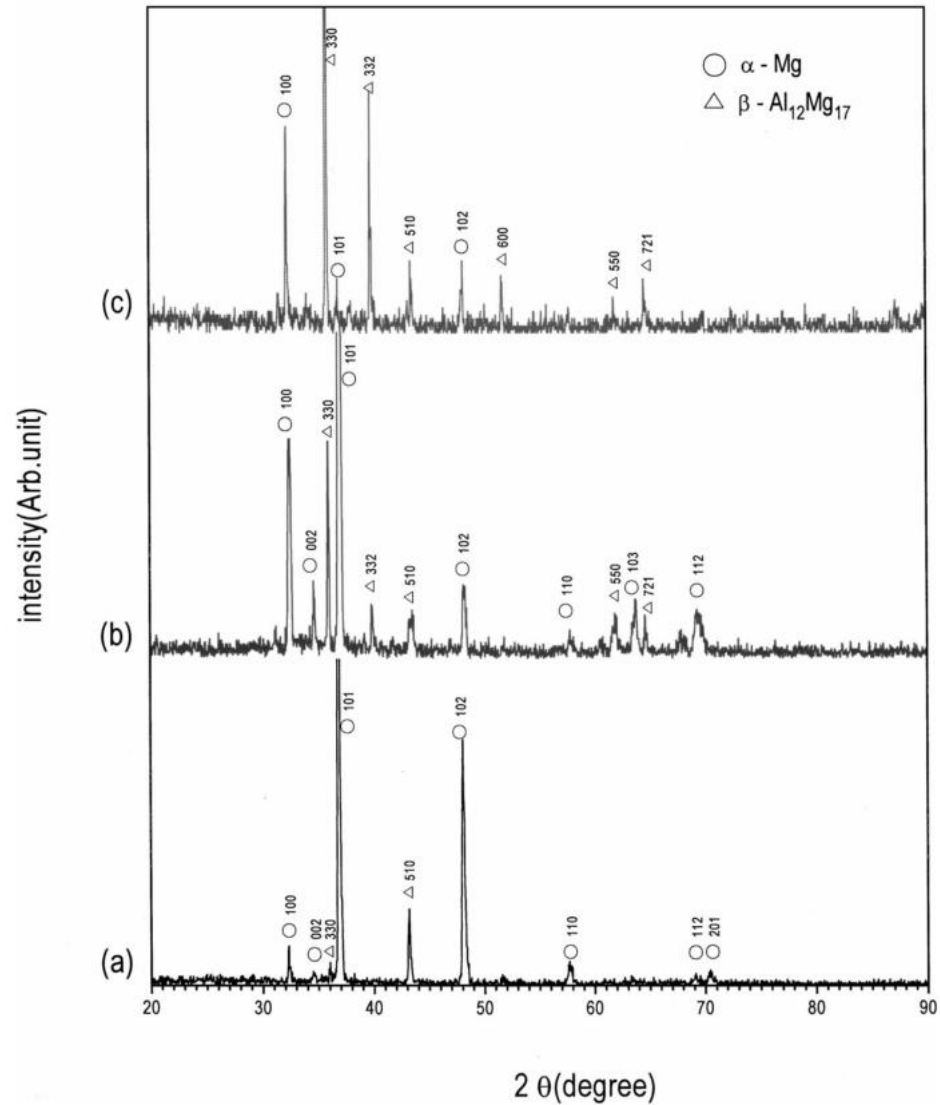
Figure 2-14 X-Ray Diffraction patterns of Mg-Al ingots containing 5, 15, and 30 atomic percent for (a), (b), and (c) respectively. Figure from [23].

Cho also analyzed flakes that were formed through rapid solidification processing (RSP). RSP results in increased solid solubility and refinement of microstructural features. These flakes were formed with the same target composition of 5, 15, and 30 atomic percent. The XRD data (Figure 2-15) showed that because of the rapid solidification effect, supersaturated solid solutions were formed with Al dissolved into Mg. This conclusion was inferred from the observable shift in

the α-Mg phase to higher angular positions that indicated a decrease in the lattice parameters. It was observed that the Mg-15Al alloy demonstrated the maximum decrease, with α-Mg phase lattice parameters of a=0.3168 nm, c=0.5156 nm, and c/a=1.627 [23].
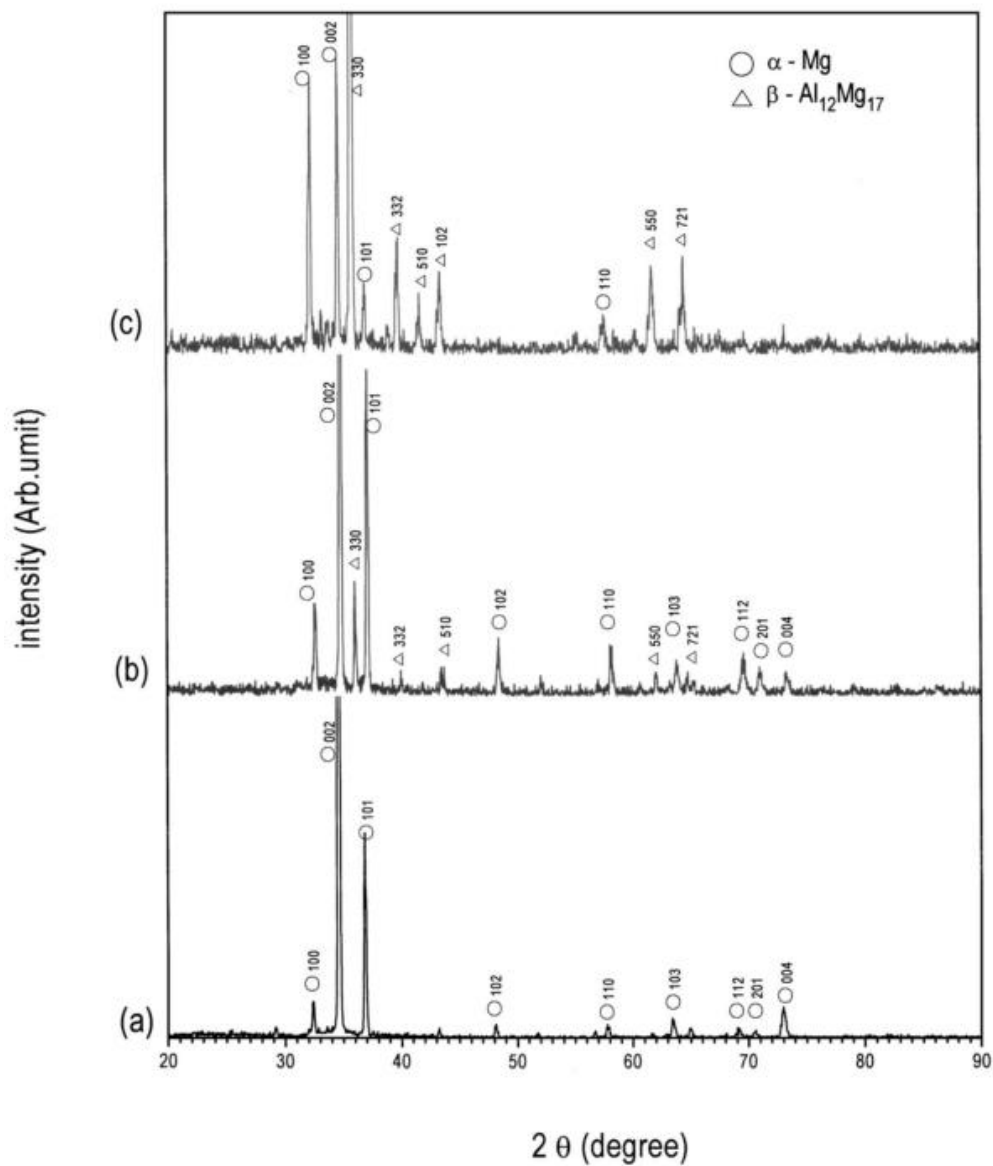
Figure 2-15 X-Ray Diffraction patterns of Mg-Al flakes formed by RSP containing 5, 15, and 30 atomic percent for (a), (b), and (c) respectively. Figure from [21].

A study performed by Shuhua Cai et al. showed that the alloying of Mg with Zn can have a positive effect on the corrosion performance of the material. Mg-Zn alloys with Zn content from 1 to 7 wt. % were made using high purity magnesium and high purity zinc ingots. The ingots were melted together in an electronic resistance furnace at 800°C and then cast into a steel mould. The compositions were measured using inductively coupled plasma atomic-emission spectrometry. The microstructure of the as-cast Mg-Zn alloys consists of α-Mg and intermetallic Mg-Zn phase along the grain boundary. The grain size decreased with increasing Zn content from 350μm for pure Mg films, 100μm for Mg-1Zn, 55μm for Mg-5Zn, and 56μm for Mg-7Zn (Figure 2-16). The decrease in grain size is significant up to 5% Zn and then the improvement drops off with further increase in Zn content.
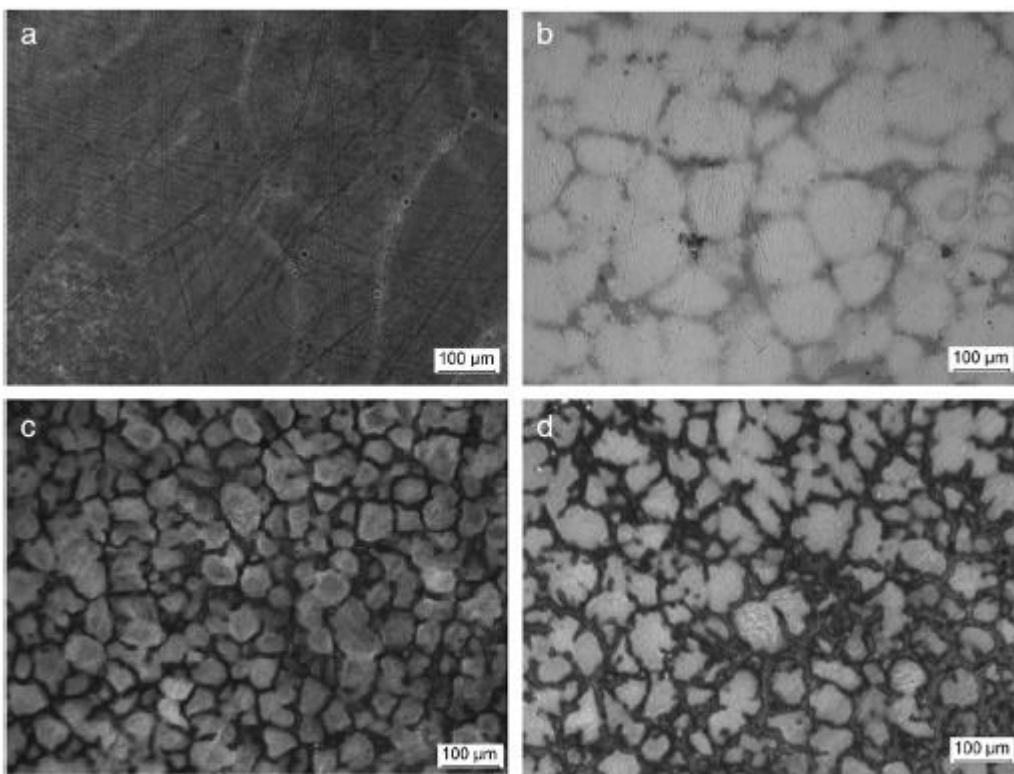
Figure 2-16 Optical micrographs of (a) pure Mg, (b) Mg-1%Zn, (c) Mg-5%Zn, (d) Mg-7%Zn. The grain size decreases significantly with the increase to 5% Zn. Image from [24].

Weight loss experiments were performed on the pure Mg and Mg-Zn alloys and it was found that the corrosion rate decreased with increasing Zn content up to 5% Zn. Additional Zn leads to an increase in the corrosion rate due to micro-galvanic corrosion that occurs between the Mg phase and the intermetallic Mg-Zn phase. The corrosion rate calculated from a weight loss experiment was 34.78mm/yr for pure Mg; and 2.01mm/yr, 1.26mm/yr, and 3.18mm/yr for 1% Zn, 5% Zn and 7% Zn respectively. Potentiodynamic testing was performed on the specimens in simulated body fluid with a pH of 7.4. Results showed that the Mg-5Zn alloy had the noblest corrosion potential, the lowest anodic current and the highest breakdown potential (Figure 2-17). This results in the best corrosion resistance and suggests that the Zn can help to form a passive layer to protect the alloy from corroding.
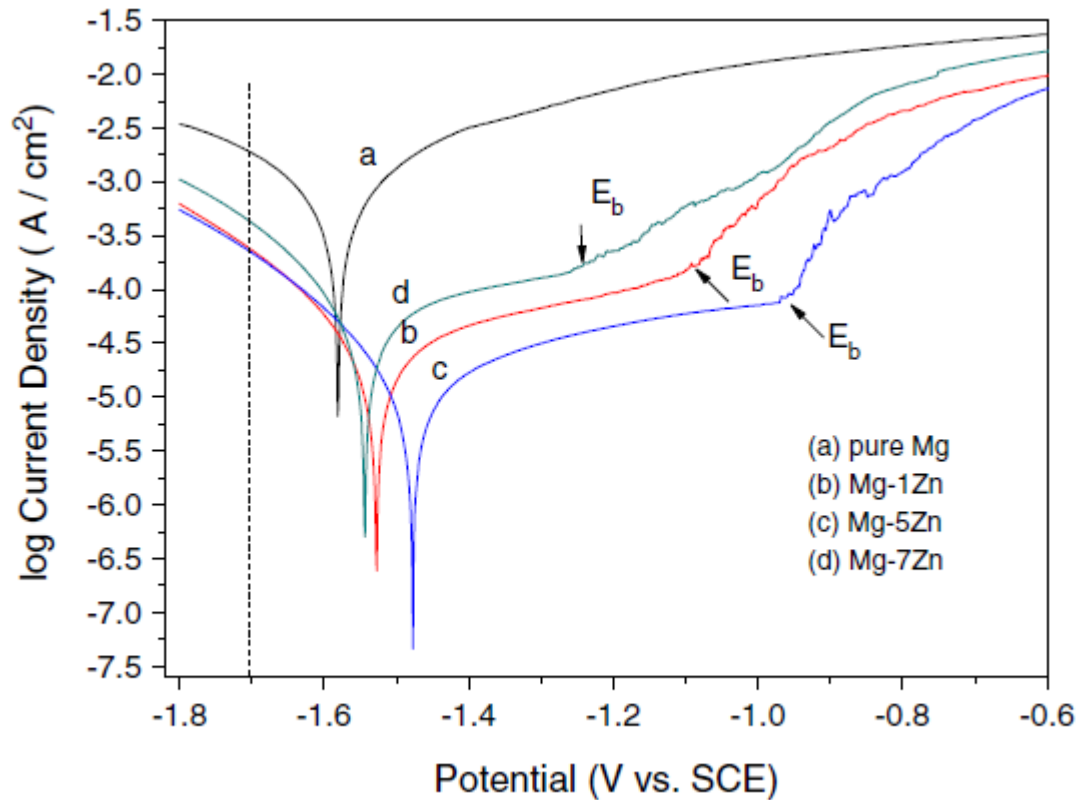
Figure 2-17 Potentiodynamic polarization curve of pure Mg and Mg-Zn alloys. Image from [24].

2.3.2 Magnesium Alloy Thin Films

A lot of research has been done on magnesium alloy thin films. One of the significant characteristics of thin films is that alloys can be created that cannot be formed using bulk methods such as casting. Thin films do not have to follow the rules of solid solubility. The way that the alloys form in vapor phase is much different than how they would form in a liquid state. This means that materials with unique characteristics can be made using deposition techniques and as a result it is a promising area of research.

An article by Charles Olk and Daad B. Haddad discusses an array of magnesium-aluminum thin film alloys. Their research into the magnesium-aluminum system was prompted by the fact that AZ91 is used in 90% of all magnesium cast products [7]. However, the use of these alloys is limited by their high reactivity and susceptibility to galvanic corrosion. It is useful to develop an understanding of the structural and compositional phases that can improve the properties of these alloys. Old and Haddad grew thin films on sapphire substrates with a mask, consisting of a 10 X 10 array of holes, was placed over the substrate prior to deposition. The films were deposited at a pressure of $\sim$ 4x10-9 Torr and a temperature of 200°C using magnetron sputtering in an argon atmosphere. The deposition rates measure in the center of the sapphire substrate was 5.4Å/s for Mg and 2.4Å/s for Al. This deposition method yielded 100 different samples, each with a unique composition. Composition ranged from 23.3 atomic percent Al to 73.9 atomic percent Al. The phases and mixed phases identified in this work were Al, Al plus amorphous, amorphous plus β-$Mg_{17}Al_{12}$ phase, and Mg + β-$Mg_{17}Al_{12}$ phase.

The XRD analysis of these samples showed that at less than 23.3% Al, films showed a mixture of the Mg and $Mg_{17}Al_{12}$ phases. With increasing composition the $Mg_{17}Al_{12}$ phase began to dominate, becoming the only phase present in the films between 40% and 50% Al. Further,

increasing the Al content lead to an amorphous Mg-Al film before the Al phase began to show in

the XRD pattern at 73.9% Al [7].
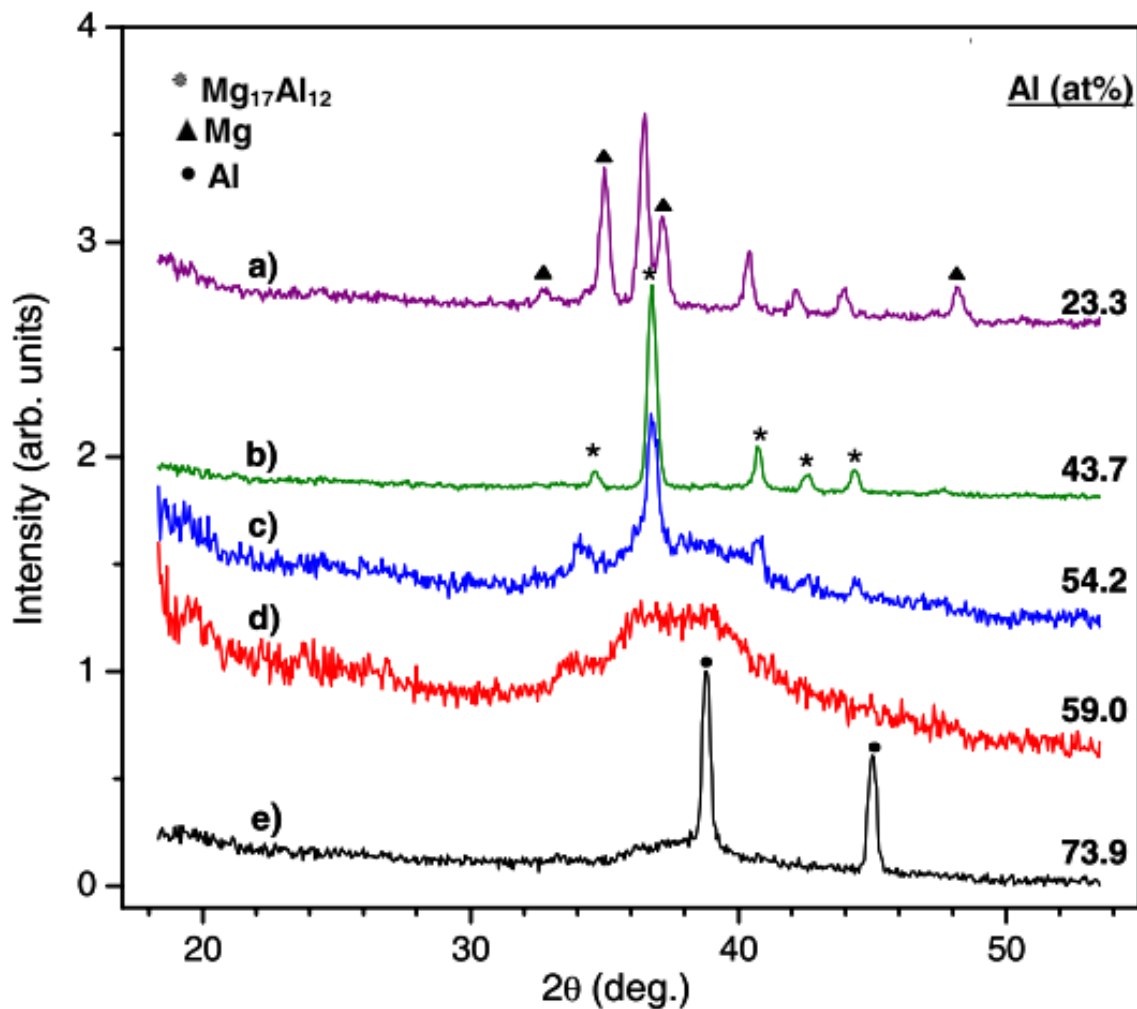
Figure 2-18 Several XRD patterns of thin films arranged by atomic % Al. The Mg peaks can be seen in the 23.3% Al. The Mg peaks disappear with increasing Al content and the $Mg_{17}Al_{12}$ phase dominates in the 43.7% and 54.2% Al films. The 59% Al film has an XRD pattern that suggests an amorphous structure. At 73.9% Al the Al phase begins to dominate. Figure from [7].

Chapter 3

Experimental

3.1 Electron Beam Physical Vapor Deposition

For this research, EBPVD was used to fabricate magnesium alloy thin-films for characterization of Mg-Al and Mg-Al-Zn thin films. The EBPVD system allows for control of the composition and microstructure of the thin films through control of the deposition parameters. The EBPVD system was designed at Penn State and features two Telemark Model 272/258 Single Pocket Electron Beam Guns that were operated at 9.8kV, quartz crystal microbalances to measure deposition rate, and a high vacuum chamber that can pump down to a pressure of under 3.E-6 Torr. The system is made up of the following key components:

- Source Material
- Substrate
- Vacuum System
- High Voltage Supply
- Electron Beam Guns
- Deposition Controllers

3.1.1 Source Material

In this research magnesium of 99.94% purity from Alfa Aesar and 99.5% weight percent aluminum from Alfa Aesar were used as source materials for depositing films of pure metals or binary systems. In addition, materials of 99% Mg- 1% Zn and 97% Mg- 3% Zn (weight percent)

from LTS research Laboratories were used to deposit Mg-Zn and Mg-Al-Zn thin films. All of the

materials were of high purity and were placed in 100cc graphite crucibles from Kamis Inc. for

deposition. For each material at least one run was performed to experimentally determine the

power at which the material evaporated at a desired rate. This made it possible to closely control

the deposition rate of each material during later runs in order to target specific thickness and

composition. The aluminum melted in the crucible prior to evaporating. The magnesium and

magnesium-zinc alloys (Figure 3-1) evaporated directly from solid.
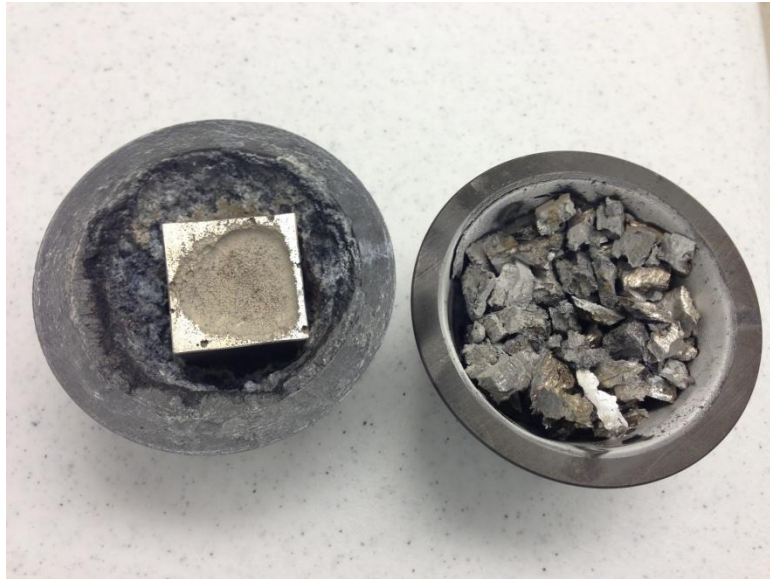
Figure 3-1 Graphite crucible liners for use in the EBPVD system. The source materials shown have already been deposited in the system. The material on the left is pure Mg and on the right is 97% Mg and 3% Zn.

3.1.2 Substrate

Materials were deposited onto six-inch diameter single crystal silicon wafers with a 100

nm oxide layer on the surface. The wafers were cleaved into several pieces and then were

mounted onto a 22 inch galvanized steel bar purchased from Home Depot. Seven pieces were

numbered 1 through 7 and placed across the beam before being taped on across the center of each

wafer as shown in Figure 3-2. The tape across the center of each wafer would later serve to

protect the wafer during deposition so that after deposition, the tape can be removed and the

thickness of the film could be measured using a profilometer.
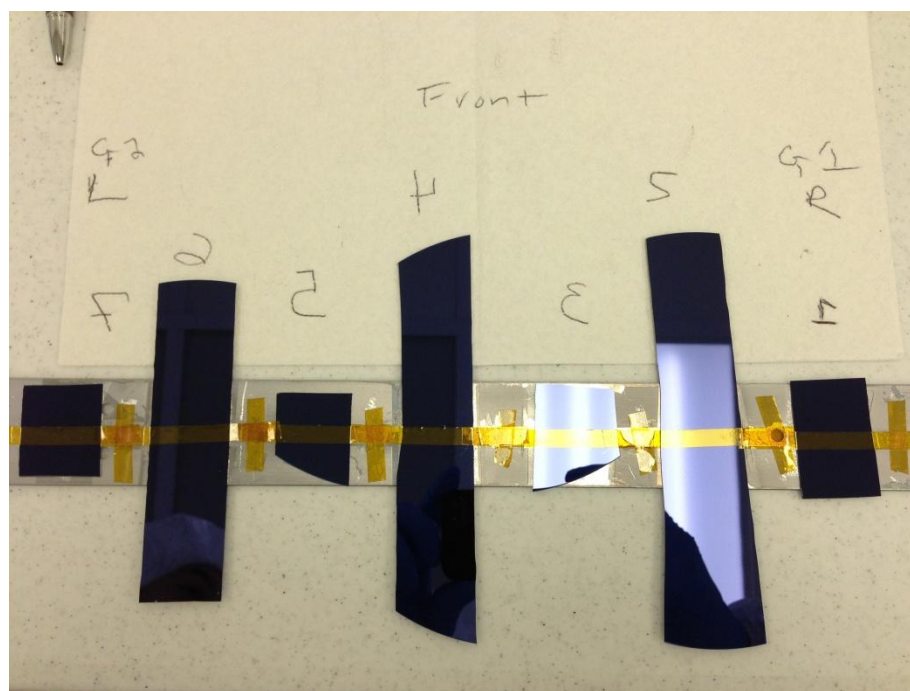
Figure 3-2 The bar setup used to hold the silicon wafer for deposition. The silicon oxide wafer was broken into pieces and then attached to a bar using Kapton tape as shown. The pieces were labeled directly on the back of the wafer using a diamond scribe. The piece labeled 1 was place in the system above Gun 1, which was used to deposit pure Mg and Mg alloys. Piece 7 was place above Gun 2 which was used to deposit Al. Pieces 2, 3, and 4 are large and were used for electrochemical testing.

The steel bar was then mounted approximately 13 inches above the source material with

the wafer labeled "1" on the right side of the chamber (above gun 1) and the wafer labeled "7" on

the left side of the chamber (above gun 2) as shown in Figure 3-3. This setup was designed to use

substrate materials efficiently while spreading them out to get a gradient of composition for

binary thin film depositions.

Figure 3-3 This picture shows the positioning bar within the chamber immediately after a deposition. The bar covers nearly the entire width of the chamber and as a result a gradient of composition, deposition rate, and thickness is achieved in a single run.

3.1.3 System Details

The vacuum system includes a Leroy-Somer SD-700 roughing pump, CTI-Cryogenics Cryo-Torr 8 High Vacuum Pump, and stainless steel bell jar (Figure 3-4). The roughing pump allows the chamber to be pumped down from atmospheric pressure, which is about 760 Torr, to under 100 mTorr. Once the system has reach 100 mTorr, a valve system allows the roughing pump to be sealed off and then the system is opened up to the cryopump, which will take it down to $3\text{x}10^{-6}$ Torr, which is high vacuum and will allow the deposition process to take place.

Figure 3-4 The EBPVD system is picture here. The vacuum chamber can be seen at the center. The cryopump is beneath the chamber and capable of the pumping the system down to a base pressure of under 3E-6 Torr.

A high voltage system provides the power that is necessary to operate the electron beam emitters. A 10 kV Telemark Model TT-10/15 Electron Beam Power Supply is connected to the electron beam emitters within the high vacuum chamber. The maximum current of this power supply is 1 Amp, which makes it a 10 kW power supply.

The system contains two Telemark Model 272/258 Single Pocket Electron Beam Guns within the chamber, each with their own electromagnet that allows the beam to be directed onto the surface of the source material. The electromagnets are controlled using a Telemark TT-

8/10/15 Power Supply Controller in order to center the beam on the source material. The gun on the right side of the chamber is referred to as "Gun 1" and it was used to deposit magnesium and magnesium alloys. The gun on the left side of the chamber is referred to as "Gun 2" and it is used to deposited aluminum, tin, and other materials that are to be combined with magnesium.

Figure 3-5 Deposition controllers for the EBPVD system. The Telemark Model (top) and the Telemark Model 860 (bottom) are both capable of controlling the power transferred to the electron guns, the deposition rate (by varying the power), and measure rate and thickness using quartz crystal microbalances within the chamber.

A deposition controller is used for each electron beam to control the power that is supplied to each electron beam emitter. Gun 1 is controlled by a Telemark Model 880 Deposition Controller and Gun 2 is controlled by a Model 860 Deposition Controller (picture in Figure 3-5). By adjusting this power, the electron beam can be used to evaporate a wide range of metals and the deposition rate can be controlled to within a few angstroms per second (1 Angstrom is 1×10^{-10} meters). The instantaneous deposition rate is measured by two quartz crystal monitors, one situated above each deposition crucible. By keeping track of the deposition rate, the thickness is also estimated and films can be grown to a target thickness.

**Figure 3-6 Kurt J. Lesker G075K ion gauge is used to
measure the pressure in the chamber during deposition.**

A Kurt J. Lesker G075K ion gauge (Figure 3-6) was used to identify a base pressure of

less than 5E-6 Torr prior to deposition. The average base pressure for the system is 3.6E-6 Torr.

The pressure rises during deposition to be on the order of 1E-5 Torr, depending on the material

and the deposition rate. Higher deposition rates resulted in higher pressure and materials that

deposited at high temperature such as aluminum and tin, would cause a rise in pressure. Quartz

crystal monitors using 6 MHz Maxtek gold-coated quartz crystals were used to monitor the

deposition rate and thickness of the film in real time. One quartz crystal monitor was used for

each deposition controller. The monitor above Gun 1 used a density of 1.73g/cm^3, the density of

magnesium; and the Gun 2 monitor was set to aluminum or tin depending on the source material

being deposited. Depositions were run to a target thickness on the Gun 1 quartz crystal monitor,

this thickness was usually 1 micron. The Gun 1 rate for magnesium alloys was maintained

between 15-20 angstroms/second. For Gun 2 the rate depended on the material and the desired

composition of the thin film. For Al and Sn, depositions were run at a rate of 1-6

angstroms/second depending on the desired composition.

3.1.4 EPBVD Geometry

The geometry of the EBPVD system has some significant effects on deposition. When a material is deposited the vapor forms a plume above the source material. The shape of this plume and the location of the substrate in relation to the plume determined the amount of vapor flux that is intercepted by the substrate at that location. As a result, geometry has a significant impact on deposition rate and final thickness of the sample. The cosine model is used for modeling the shape of an EBPVD vapor plume. The vapor intensity of the plume can be expressed by Equation 3-1. $I(\alpha)$ is the vapor intensity in a direction α degrees from the normal, I_0 is the vapor intensity at $0°$ and n is an empirical parameter that depends on the rate of evaporation.

Equation 3-1 The vapor intensity of an EBPVD vapor plume according to the cosine model.

$$I(\alpha) = I_o \cdot \cos^n \alpha \quad \left[\text{kg/m}^2\text{s} \right]$$

The range of the vapor plume is expressed in Equation 3-2. In this equation, $r(\alpha)$ is the range of the vapor plume in a direction α degrees from the normal, r_0 is the range of the vapor plume at $0°$ (which is assumed to be equal to the substrate height), and n is an empirical parameter that depends on the deposition rate and material being evaporated. This simple mathematical expression also assumes a pure point source. In the case of our system, we do not have a pure point source because we oscillate a beam of about 1mm by 3mm over a large crucible. This will modify this simple model for the shape of the plume. Examples of 2D profiles of vapor plumes are shown in Figure 3-7.

Equation 3-2 The range of an EBPVD vapor plume according to the cosine model.

$$r(\alpha) = r_o \cdot \cos^n (\alpha) \quad \left[\text{m} \right]$$
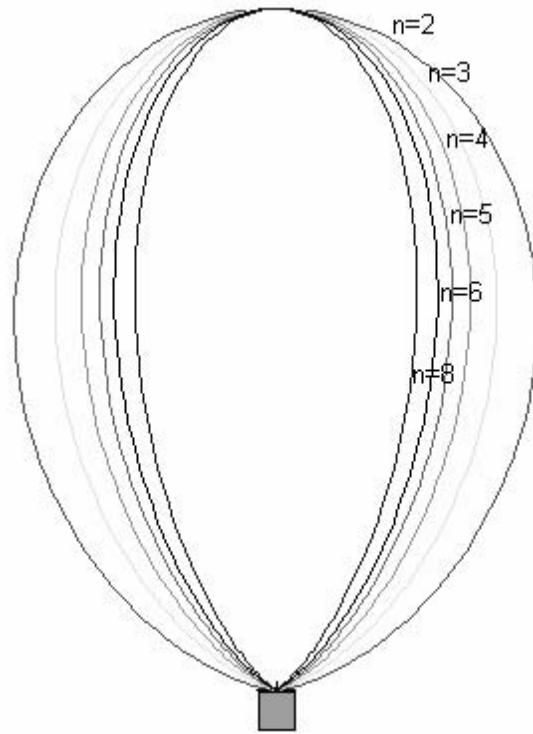
Figure 3-7 2D profiles of the vapor plume according to the cosine model. The effect of changing n values is shown. Figure from [25].

For a flat plate that is stationary above the source material the equation for the relative coating thickness is as follows:

Equation 3-3 The ratio of coating thickness as position S to the thickness at position S0.

$$\frac{d_s}{d_{so}} = \frac{1}{\left(1+\left(\frac{r_s}{h_v}\right)^2\right)^{\frac{n+3}{2}}}$$

In Equation 3-3, d_s is the local film thickness, d_{so} is the film thickness for $\alpha = 0$, r_s is the distance on the substrate from the point of maximum thickness, h_v is the height of the substrate over the source material. This shows that there is a relationship between r_s, h_v and d_s such that as the substrate is moved away from the source, the thickness will decrease.

3.2 Profilometry

After a film has been deposited on the surface of the substrate and removed from the vacuum chamber, profilometry was performed to measure the thickness of the film. The wafer is placed into a Tencor Alpha Step 500 Surface Profiler contact profilometer, which measures the thickness of the film by dragging a stylus across the surface and measuring the difference in the depth of the stylus. Prior to depositing on the substrate, a small piece of glass is attached with Kapton tape. After deposition, the glass piece is removed and the profilometer is able to measure the difference between the surface of the substrate and the surface of the film. This thickness measurement is necessary because the thickness of each piece can be measured individually and it accounts for differences in distance, angle, and contribution from a second source material for each piece.

3.3 Energy Dispersive Spectroscopy

Energy Dispersive Spectroscopy is used for qualitative and quantitative analysis of elements in a sample. During EDS, a sample is bombarded by a beam of electrons and the energy of emitted X-rays is measured to obtain chemical analysis. The energy of emitted x-ray photons can be matched to the K-alpha and L-alpha transitions to identify each element in a sample. In order to obtain a quantitative analysis of the sample, the intensity of each peak is measured using the counts per second and taking into account each element found in the sample, the composition can be obtained by using standards of know composition in a database. EDS is capable of identifying and quantifying all elements except for H, He and Li [26]. With the recent advent of the silicon drift detector; in the energy dispersive X-ray spectrometer, higher throughput is achieved. This higher throughput allows for quantitative accuracy and precision equivalent to that

of electron-excited wavelength dispersive spectroscopy (WDS) [26]. This ability of the EDS

detector to measure k-ratios equivalent to WDS was shown by Ritchie et. al [27] as shown in

Figure 3-8.

Figure 3-8 Comparison of k-ratios measured by WDS and EDS (Ritchie et. al. [27]).

For quantitative analysis, an accuracy of ± 1% can be achieved. The mass concentration

of an element is proportional to the relative intensity of that element's X-ray line [28]. This

relationship is due to the fact that the incident electrons penetrate to the same depth regardless of

the composition. The INCA software performs quantitative analysis by using this proportion and

comparing the intensity of each element to standards of known composition. In order to make this

comparison several corrections are made by the software to remove background noise. This

technique allows compositions for multiple samples produced in a single physical vapor deposition to be obtained very quickly.

For this research, a Quanta 200 SEM, shown in Figure 3-9, was used with an accelerating voltage of 10 keV and working distance of the beam at 12.2mm to collect EDS spectra.
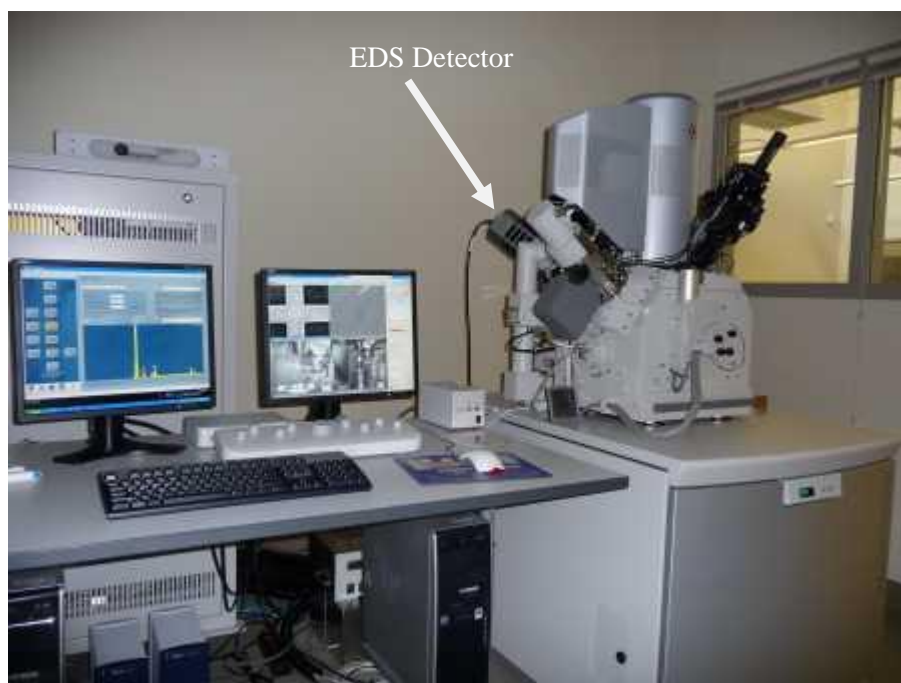
Figure 3-9 Quanta 200 SEM with EDS detector. The EDS detector is attached on the back of the chamber.

Two spectra were collected at a magnification of 5,000 times for each sample. The qualitative and quantitative analysis was performed by the INCA software package. The INCA software automatically identifies the elements present in a sample by matching the X-ray peaks to the specific energies of the elements. The elements can then be corrected manually if necessary. Once the quantitative analysis is complete, the software can analyze the spectra using the identified elements to determine element mass concentration. Positions 1 through 7 were analyzed with EDS for each run to identify the different compositions created in the run as each position gets

further away from gun 1 and closer to gun 2. Samples were mounted on pegs and secured by double-sided carbon tape and a corner of the surface was painted with colloidal graphite to make an electrical connection.

3.4 X-Ray Diffraction

X-ray diffraction is an analytical technique that uses an x-ray beam to determine the crystal structure, identify phase composition, and measure preferred orientation and crystallinity. The beam of incident x-rays is diffracted in many directions by the sample. The angles and intensities of the diffracted beams can be measured to identify the crystal structure of the sample. Samples were cleaved into 1 cm^2 pieces and placed onto a zero background glass slide before being placed into the diffractometer. The diffractometer used for this research was a PANalytical XPert Pro MPD that uses a copper source and a theta-theta goniometer (Figure 3-10). The diffractometer was used in the grazing incidence (GIXRD) mode in order to prevent the beam from penetrating through the film and into the silicon substrate.
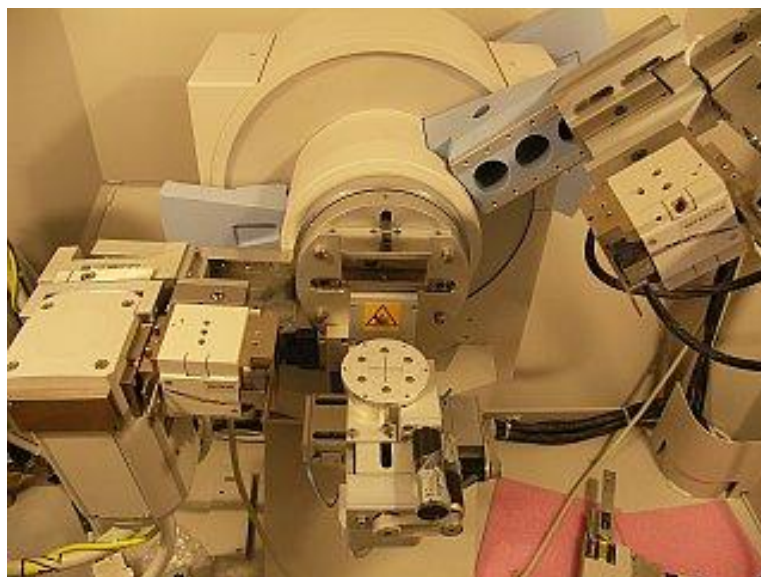
Figure 3-10 PANalytical XPert Pro MPD used to perform Grazing Incidence X-Ray Diffraction on thin films.

3.5 Field Emission Scanning Electron Microscope

A field emission scanning electron microscope (FESEM) is used to image materials by scanning the material with a beam of electrons. In this project, secondary electron imaging was used to study the morphology of the film surfaces and the growth characteristics of the film cross sections. The Leo 1530 Field Emission Scanning Electron Microscope is a high resolution, software controlled microscope. It is able to provide high resolution imaging at accelerating voltages as low as 1 kV. It features a high resolution Annular In-lens secondary electron detector that can be used to image at a resolution as high a 5nm for conductive samples. High resolution images can be obtained with magnifications as high as 200,000 times. It can also use a conventional Everhart-Thornley detector and an annular back-scattered electron detector. Electrons are generated by a Schottky type field emission gun which is then focused and formed by a magnetic lens.
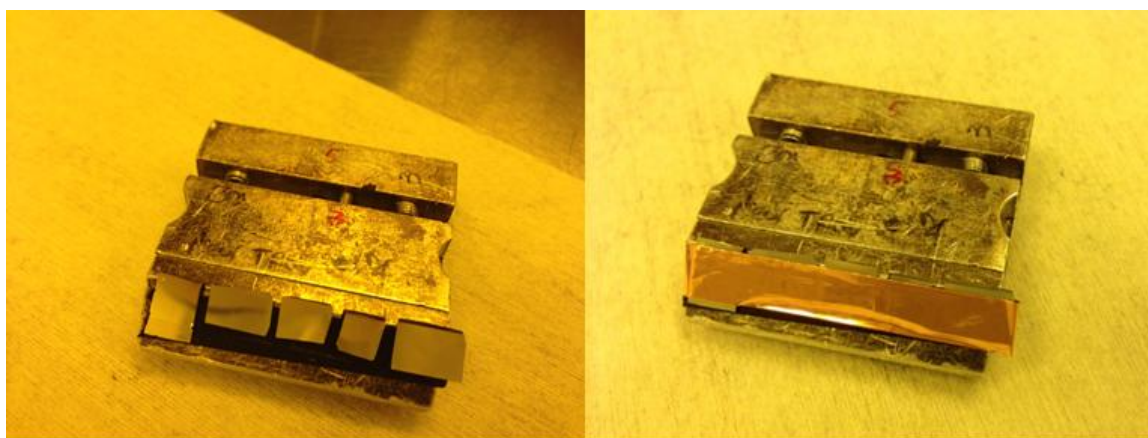
Figure 3-11 Mounting tool for the LEO FESEM. Samples were attached to the base using carbon tape and then secured with a layer of copper tape that held the samples in place firmly and provided conductive contact to the thin film to avoid charging during imaging.

Samples were cleaved into small pieces of approximately 1 cm^2 and mounted onto a substrate holder with double-sided carbon tape. Copper tape was then placed over the surface of the sample in order to make conductive contact with the thin film. The film stuck out of the top of the copper tape leaving an area of the surface to image along with the cross section of the film as shown in Figure 3-11. The films were then loaded into the chamber and tilted by 10 degrees to allow the surface to be examined along with the cross section.

3.6 Electrochemical Testing

Electrochemical testing was conducted to determine the corrosion characteristics of the samples. The tests were conducted on a Gamry Reference 3000 Potentiostat, which is connected to a computer that uses the Gamry Instruments Framework software to run electrochemical experiments. Gamry Echem Analyst was used to analyze the electrochemical data and Microsoft Excel 2007 was used to create plots and tables of the data. Three types of electrochemical tests were performed on each thin film sample. First open circuit potential (OCP) measurements were made before each test. This allowed the OCP to be indentified and the electrochemical cell to stabilize. Next a polarization resistance test was run that could be used to calculate the corrosion rate of a sample. OCP was run again for 2 minutes following the polarization resistance test. Next electrochemical impedance spectroscopy was done to provide another way to calculate polarization resistance and corrosion rate values. Finally, OCP was run for 5 minutes after the EIS test was completed.

3.6.1 Sample Preparation

Samples at positions 2, 4, and 6 (on the positioning bar) were used for electrochemical testing. The samples were cleaved into two 2-inch sections that could be used for corrosion testing. 3M™ electroplating tape 470 was then laid on a piece of wax-paper and two 0.603 cm^2 holes were punched into the tape using a standard hole-punch. The tape was then removed from the wax paper and placed onto the sample on the surface of the film. This left two areas exposed where the holes were punched. These areas would be used for testing by fitting an O-ring from the cell around the hole. A 6-inch piece of copper tape was attached to an exposed region of the film and folded over onto itself and attached to the backside of the wafer. This piece of copper provided a way to connect the electrode to the film. A second piece of electroplating tape was placed over the exposed region of the sample, including the copper tape. Figure 3-12 shows a thin film ready for electrochemical testing. The film was then carefully fitted against the O-ring of the MPM flat cell.

Figure 3-12 Thin film prepared for electrochemical testing. Multiple test areas were able to be placed on a single thin film. The electroplating tape asks as a mask so that only the exposed area is tested. The copper tape provides electrical contact to the surface of the thin film.

3.6.2 Electrochemical Cell Setup

For each electrochemical experiment, an electrochemical MPM flat cell was used with artificial seawater as an electrolyte. Three electrodes are required for the experiments, a reference electrode, counter electrode, and working electrode. A saturated calomel electrode (SCE) was used as the reference electrode. The working electrode was the thin film sample and a graphite plate was used as the counter electrode. The experiments were conducted at ambient lab temperature, which is about 25°C.

3.6.3 Open Circuit Potential

The open circuit potential is the potential of the working electrode relative to the reference electrode when no external potential or current is applied to the cell. The first experiment that is run in the sequence of corrosion experiments is a measurement of the open circuit potential. This potential value will provide a reference point for the following experiments. Open circuit potential experiments were performed for 20 minutes before and after each set of polarization resistance and EIS experiments.

3.6.4 Polarization Resistance

In a polarization resistance test, the voltage is varied around the open circuit potential and the resulting current is recorded, then a linear graph of potential (V vs. SCE) vs. current density is generated by the Gamry Echem Analyst. The R_p can be found from the slope of this graph through 0 current density and used to determine corrosion current density i_{corr} by using the Stearn Geary equation (Equation 1).

$$i_{corr} = \frac{\beta_a \beta_c}{2.3(\beta_a + \beta_c)R_p}$$

Equation 3-4 Calculation of corrosion current density from polarization resistance

Where i_{corr} is the corrosion current density (A/cm^2), R_p is the polarization resistance ($\Omega*cm^2$) (which is determined by taking the slope of the polarization curve, β_a is the anodic Tafel slope (V/decade) and β_c is the cathodic Tafel slope (V/decade). It is common practice to estimate both Tafel slope values to be 0.1 V/decade. Once the corrosion resistance is determined by plugging R_p into Equation 1, the corrosion rate can be determined using Equation 2.

$$r = \frac{K * i_{corr} * EW}{\rho}$$

Equation 3-5 Calculation of corrosion rate from corrosion current density

In Equation 2, r is the corrosion rate in units determined by the constant, K, i_{corr} is the corrosion current density ($\mu A/cm^2$), EW is the equivalent weight, and ρ is the alloy density (g/cm^3). Equivalent weight and alloy density can be determined from the properties of the alloying materials and the ICP data. The corrosion current density is taken from the experimental data and the calculations of Equation 1. K is a constant that can be varied to allow the equation to output corrosion rates in different units. In this research, a K value of 0.129 was used to yield a corrosion rate in mils per year (mpy).

3.6.5 Electrochemical Impedance Spectroscopy

Electrochemical impedance spectroscopy (EIS) can be used to determine the corrosion rate of a metal sample in an electrolyte. During EIS a sinusoidal current is applied to the sample as a function of frequency the impedance is measured. The R_p can be determined from the Bode plots that are generated by the Gamry Analyst software using the EIS data. The R_p value is calculated by subtracting the solution resistance, R_s, from the Zmod value at the lowest measured frequency value. This gives an R_p value in units of Ω which is then multiplied by the sample area (0.603 cm^2) to get a value in $\Omega*cm^2$. Once the R_p is calculated it can be plugged into Equation 1 to find the corrosion current density, which can then be used in Equation 2 to determine the corrosion rate, in the same way that was described for polarization resistance. EIS experiments were run with a DC voltage of 0V vs. Open Circuit Potential, an AC Voltage of 10 mV rms, and initial frequency of 100,000 Hz and a final frequency of 0.03 Hz.

Chapter 4

Results and Discussion

This section will provide an overview of the process used to develop and characterize each thin film sample. The process begins with the deposition of the sample on the EBPVD system. For each deposition, the deposition rate and pressure were monitored in real-time. These were controlled in order to target a particular deposition rate or composition by mixing materials during a two-gun run. After deposition, the films were tested using profilometry to measure thickness. This thickness was then used to calculate an average deposition rate for each sample. This provided a true measure of the average deposition rate over the course of the deposition and can be compared to the deposition rate measured by the QCM during deposition at a particular spot in the chamber. The deposition rate as a function of the geometry of the chamber was measured to see the effect of deposition angle on the deposition rate and other thin film characteristics.

After the thickness was measured for each chamber position during an alloy deposition, binary and ternary samples such as Mg-Al and Mg-Al-Zn films were analyzed via EDS for composition analysis. This provided the chemical composition for each sample that was used in further discussions of the thin film properties. Thin films were then analyzed using FESEM in order to observe the structure of the cross section and the surface morphology of each film. These observations provide information on defects in the films and check for a columnar growth or dense layer-by-layer growth. Films were then analyzed by GIXRD in order to determine the phases and crystallographic planes present in the microstructure. This also showed if precipitates were forming on the within the grain or in the grain boundaries after deposition.

Finally, the corrosion measurements were taken on the thin films. This allowed the corrosion rate data to be compared to all of the previous data (composition, deposition rate, microstructure, growth method, etc.) to search for trends that affect the corrosion rate.

4.1 EBPVD Calibration and Geometry

Single gun depositions were conducted for each pure material that was going to be used for alloy formation in order to get an idea of the deposition rates that could be maintained for each material. Pure Mg runs were performed at various deposition rates to see if the deposition rate measured by the QCM during deposition was the same as the deposition rate calculated by measuring the thickness of each sample using profilometry and then dividing that by the total deposition time for that sample. The deposition rates measured by the QCM were significantly lower than the calculated deposition rates for the thicker samples in each run. This effect increased with increasing deposition rate. For example, the pure Mg deposition performed on December 4, 2013 had a maximum deposition rate measured on the QCM of 75 Å/s and the maximum calculated rate was 128 Å/s for Position 3 as shown in Table 4-1. The deposition rate tends to decrease as the deposition angle and distance increase. This trend is stronger for higher rate depositions. Lower rate depositions have a more uniform deposition rate across all 7 positions.

Table 4-1 Depositon Rates of pure Mg and Mg-Zn films deposited using Gun 1. Deposition rate is calculated from the thickness measured using profilometry and then divided by the deposition time. The table shows that the deposition rate tends to decrease as angle and distance from source material increase. The source material for gun 1 is located between positions 1 and 2.

Calculated Deposition Rates of Gun 1 Depositions (Å/s)								
Date	Material	Position 1	Position 2	Position 3	Position 4	Position 5	Position 6	Position 7
8/9/2013	Mg	99.69	94.97	87.88	72.92	58.04	51.18	43.60
10/15/2013	Mg	43.91	42.68	43.14	52.71	53.42	46.89	42.00
12/4/2013	Mg	126.60	127.40	128.19	111.67	92.38	74.81	52.00
12/10/2013	Mg	10.86	10.62	9.97	9.75	9.47	9.45	9.27
8/15/2013	Mg-Zn 97-3	73.07	71.58	61.85	51.73	49.04	40.89	32.95
8/26/2013	Mg-Zn 99-1	33.44	33.94	32.35	27.58	23.14	17.67	14.36
10/8/2013	Mg-Zn 99-1	26.92	26.27	24.29	23.76	19.02	18.02	15.42
4/3/2014	Mg	28.73	30.38	29.35	26.44	26.90	29.53	26.84

The data for the calculated deposition rates of the Gun 1 depositions can be seen in Figure 4-1. The runs with higher deposition rate show a sharp decrease in deposition rate across as the distance and deposition angle increase (Figure 4-2). The runs with lower deposition rates show less of an effect from deposition angle and distance (Figure 4-3). The ratio of Position 1 to Position 7 is shown in Table 4-2. The ratio for the film at a deposition rate of about 10 Å/s is 1.17 and ratio for the highest deposition rate, which was run at 126 Å/s, was 2.42. This implies that the plume shape of the deposition changes for Mg with a change in beam power and deposition rate. This finding matches the variation of thickness that is expected due to the changing plume shapes predicted by the cosine model. By increasing the deposition rate we have increased the n value of the cosine model (Equation 3-1 and Equation 3-2), which results in a narrower plume and a more significant change in thickness and deposition rate with changing position. In future work, the thickness and deposition rate data could be used to determine the n values for magnesium at various deposition rates.

Equation 4-1 The vapor intensity of an EBPVD vapor plume according to the cosine model.

$$I(\alpha) = I_o \cdot \cos^n \alpha \quad \left[\text{kg/m}^2\text{s} \right]$$

Equation 4-2 The range of an EBPVD vapor plume according to the cosine model.

$$r(\alpha) = r_o \cdot \cos^n(\alpha) \quad [\text{m}]$$

The run performed on October 15, 2013 is an outlier as the deposition rate is highest for the middle positions and then drops off on both sides. This is likely due to shadowing of Positions 1, 2, and 3 during this deposition due to the shutter being misplaced. As a result, the electrochemical values for Position 2 of the 10/15/2013 were not reliable and were not presented.

Table 4-2 Numerical analysis of the decrease in deposition rate from Position 1 to Position 7 for Gun 1 depositions.

Deposition Rate Analysis for Gun 1 Depositions				
Date	Material	Position 1	Position 7	Position1/Position 7
12/10/2013	Mg	10.86	9.27	1.17
10/8/2013	Mg-Zn 99-1	26.92	15.42	1.75
4/3/2014	Mg	28.73	26.84	1.07
8/26/2013	Mg-Zn 99-1	33.44	14.36	2.33
8/15/2013	Mg-Zn 97-3	73.07	32.95	2.22
8/9/2013	Mg	99.69	43.60	2.29
12/4/2013	Mg	126.60	52.00	2.42

Calculated Deposition Rates of Gun 1 Depositions
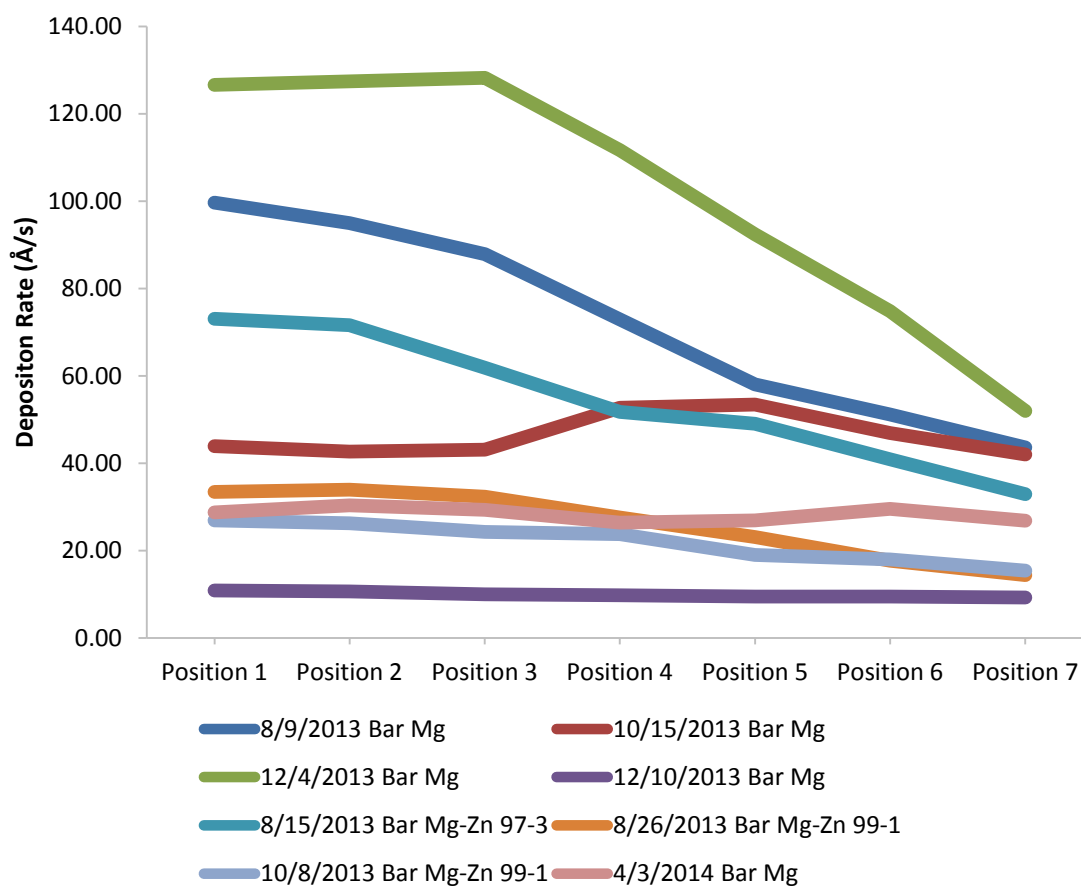
Figure 4-1 Chart showing the calculated deposition rates for single gun depositions performed on Gun 1. Each line shows the rate data for a single deposition.
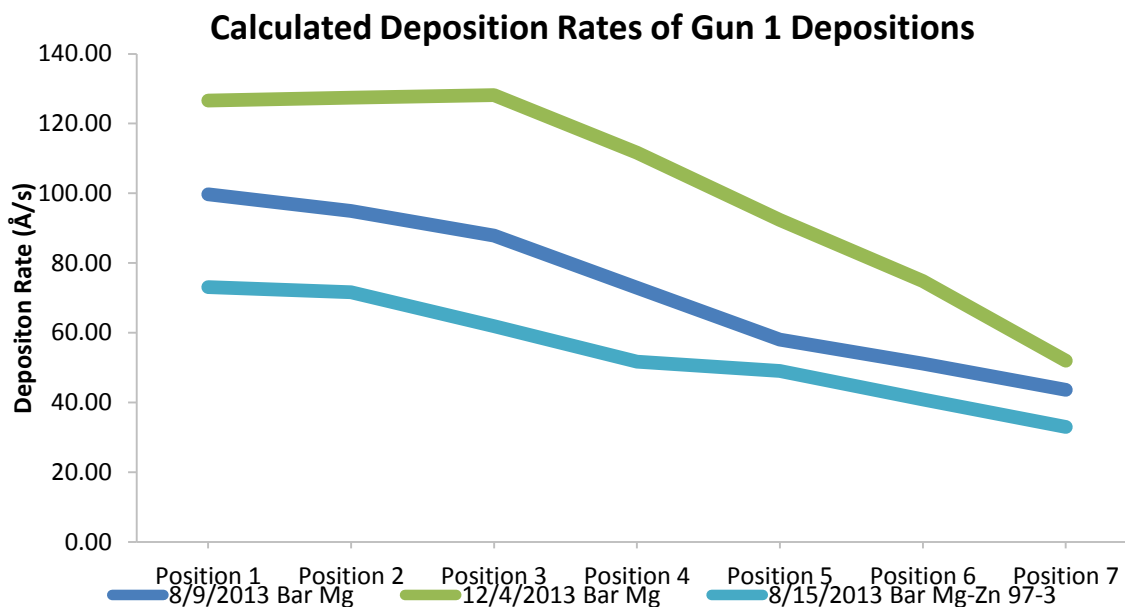
Figure 4-2 Chart showing the calculated deposition rates for single gun depositions performed at high deposition rates on Gun 1. Each line shows the rate data for a single deposition. The deposition rates decrease from Position 1 to Position 7.
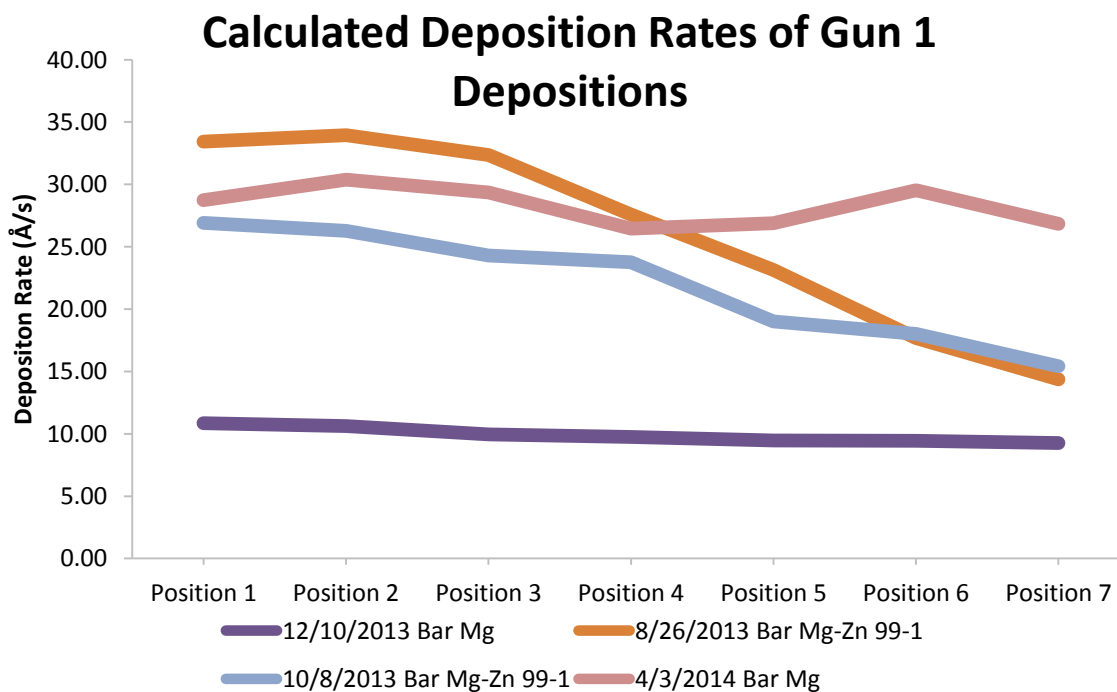
Figure 4-3 Chart showing the calculated deposition rates for single gun depositions performed at low deposition rates on Gun 1. Each line shows the rate data for a single deposition. The deposition rates decrease from Position 1 to Position 7. The decrease is not as significant for low deposition rates as it is for high deposition rates.

Pure Sn and Al deposition were done using just Gun 2. The maximum deposition rate

measured by the QCM for the pure Al deposition run on February 28, 2014 was 5.4 Å/s and the

highest calculated deposition rate was 10.07 Å/s for Position 7 as seen in Table 4-3.

Table 4-3 Depositon Rates of pure Al and pure Sn films deposited using Gun 2. Deposition rate is calculated from the thickness measured using profilometry and then divided by the deposition time. The table shows that the deposition rate tends to decrease as angle and distance from source material increase. The source material for gun 2 is located between positions 6 and7.

Calculated Deposition Rates of Gun 2 Depositions (Å/s)								
Date	Material	Position 1	Position 2	Position 3	Position 4	Position 5	Position 6	Position 7
8/29/2013	Al	5.34	7.71	8.41	10.70	10.99	13.33	11.77
2/22/2014	Al	1.18	1.78	2.56	2.60	1.70	2.12	2.64
2/24/2014	Sn	0.70	1.05	0.96	1.23	1.58	1.54	2.03
2/28/2014	Al	4.34	5.59	6.51	8.26	9.10	9.84	10.07

Table 4-4 Numerical analysis of the decrease in deposition rate from Position 1 to Position 7 for Gun 1 depositions.

Deposition Rate Analysis for Gun 2 Depositions				
Date	Material	Position 1	Position 7	Position 7/Position 1
2/24/2014	Sn	0.70	2.03	2.88
2/22/2014	Al	1.18	2.64	2.23
2/28/2014	Al	4.34	10.07	2.32
8/29/2013	Al	5.34	11.77	2.20

For the Gun 2 films the deposition rate decreases as angle and distance from source

material increase meaning that the rate decreases from Position 7 to Position 1. The trends for

Gun 2 can be observed in Figure 4-4. The deposition rate is highest at Position 7 and tends to

decrease as angle and distance decrease. The Position 7 to Position 1 deposition rate ratio is

shown in Table 4-4 and shows that the ratios are highest for Sn and higher for Al than they were

for Mg at low deposition rates (less than 40 Å/s), which implies that Sn and Al have a narrower

plume shape than Mg for low deposition rates (meaning that they have a higher n value at low

deposition rates). This significant change in rate allows for samples of varying composition to be produced in a single run. For the pure Al run performed on August 29, 2013, Position 6 actually has the highest deposition rate. It is possible that Position 7 was partially masked during this deposition due to the shutter that is used to mask the QCM being out of position.

Calculated Deposition Rates of Gun 2 Depositions
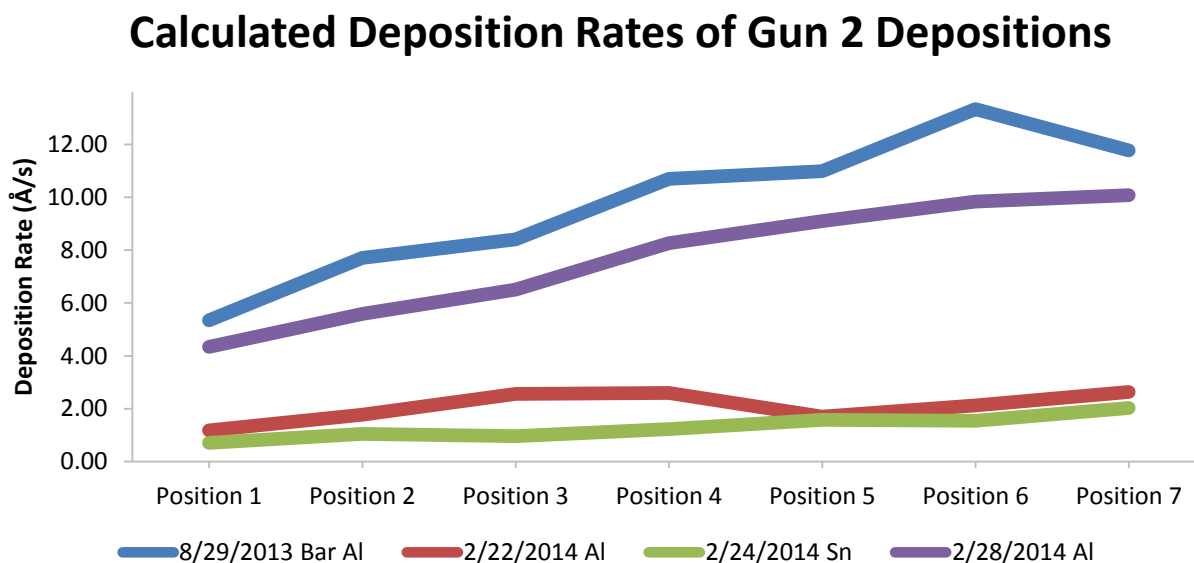
Figure 4-4 Chart showing the calculated deposition for single gun depositions performed on Gun 2. Each line shows the rate date for a single deposition. The deposition rates decrease from Position 7 to Position 1.

Additional analysis was done on the geometry and deposition rate of the pure Mg films. For binary or Mg-Zn thin films the effects of changing composition from position to position cannot be separated from the geometrical effects or the effect of deposition rate. For pure Mg films these parameters can be easily analyzed and compared. Films were prepared with target deposition rates of 7, 25, and 70 Å/s. The deposition rates of these pure Mg thin films calculated from the profilometry are shown in Table 4-5. The thickness measurements from the profilometry can be seen in

Table 4-6.

Table 4-5 Deposition Rate of Pure Mg Thin Films. The 10/15/2013, 12/4/2013, and
12/10/2013 films were deposited at target rates of 25, 7, and 70 Å/s respectively.

Deposition Rate of Pure Mg Thin Films by Position (Å/s)								
Date	Material	Position 1	Position 2	Position 3	Position 4	Position 5	Position 6	Position 7
10/15/2013	Mg	43.91	42.68	43.14	52.71	53.42	46.89	42.00
12/4/2013	Mg	126.60	127.40	128.19	111.67	92.38	74.81	52.00
12/10/2013	Mg	10.86	10.62	9.97	9.75	9.47	9.45	9.27

Table 4-6 Thickness of Pure Mg Thin Films. The thickness measurements shown were
taken from the average of two measurements of a profilometer. The 10/15/2013, 12/4/2013,
and 12/10/2013 films were deposited at target rates of 25, 7, and 70 Å/s respectively.

Thickness of Pure Mg Thin Films by Position (μm)								
Date	Material	Position 1	Position 2	Position 3	Position 4	Position 5	Position 6	Position 7
10/15/2013	Mg	3.43	3.33	3.37	4.11	4.17	3.66	3.28
12/4/2013	Mg	2.66	2.68	2.69	2.35	1.94	1.57	1.09
12/10/2013	Mg	2.35	2.29	2.15	2.11	2.05	2.04	2.00

The calculated deposition rates were higher than what was measured by the QCM during

deposition and the deposition rate decreases with increasing angle and distance from the chamber,

as discussed previously in this section. The 10/15/2013 run does not follow this behavior. It is

likely that the substrate was partially shadowed during this deposition. Because these are pure Mg

one can compare the thickness and deposition rate data to electrochemical data without having an

effect from changes in composition.

Several graphs have been prepared to compare deposition parameters to electrochemical

results. In these graphs, the corrosion data from the sample in position 2 from 10/15/2013 was

omitted due to it differing from the corrosion rates of the other samples by over an order of

magnitude. This was likely because of crevice corrosion due to leaking of the electrolyte around

the edges of the electroplating tape, which also means that an unknown area is being tested. The

first graph shows corrosion rate vs. deposition rate, which can be seen in Figure 4-5. Figure 4-6

plots the Corrosion Rate vs. Thickness. It appears that the corrosion rate of the thin films is

slightly higher with increasing thickness. However, this effect is small and is likely due to an

increase in surface area as the film surface becomes less ordered as it grows further from the substrate. The surface of these films will be examined later. Analysis did not find any correlation between corrosion rate and sample position (Figure 4-7).

Corrosion Rate vs. Deposition Rate
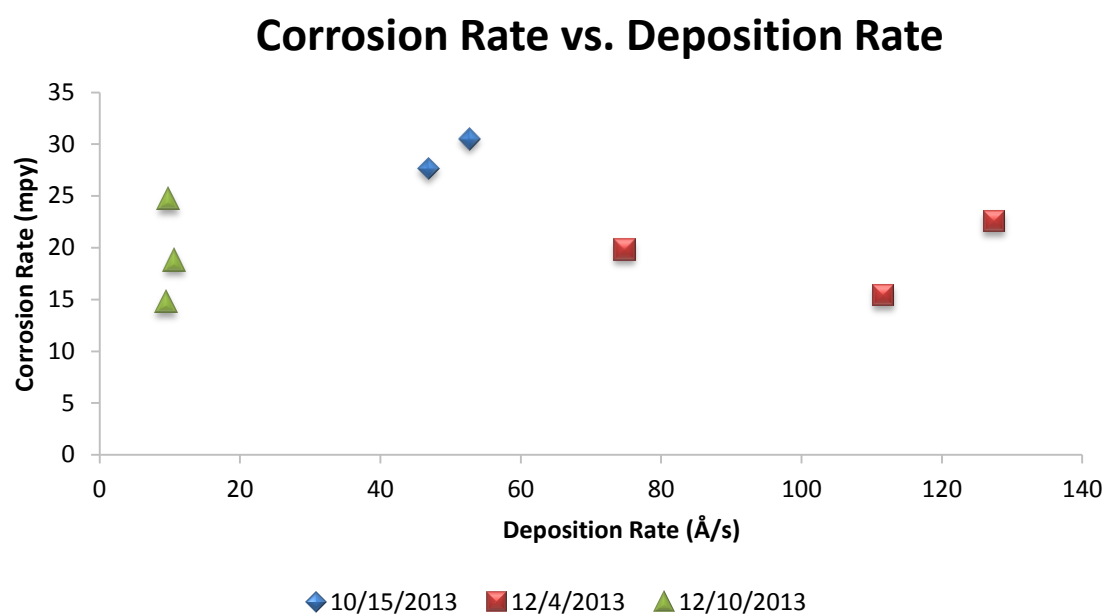
Figure 4-5 Corrosion Rate vs. Deposition Rate for pure Mg thin films. Observation of this plots leads to the conclusion that deposition rate does not affect the corrosion rate of the thin film sample.

Corrosion Rate vs. Thickness
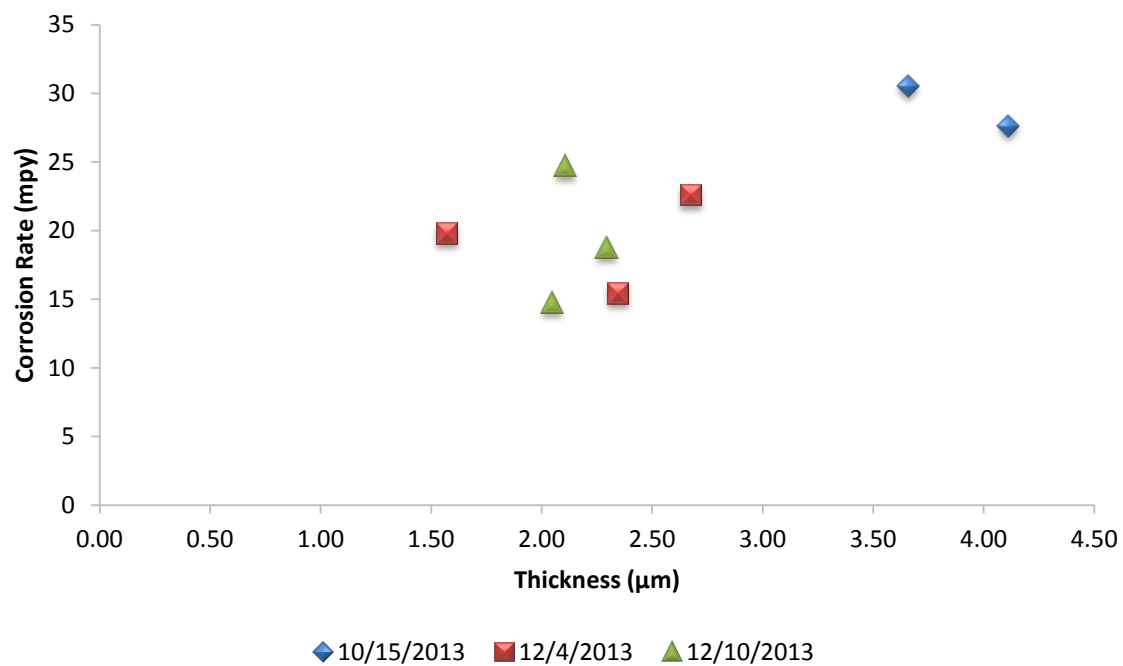
Figure 4-6 Corrosion Rate vs. Thickness for pure Mg thin films. Observation of this plots leads to the conclusion that thickness does not affect the corrosion rate of the thin film sample.

Corrosion Rate vs. Position
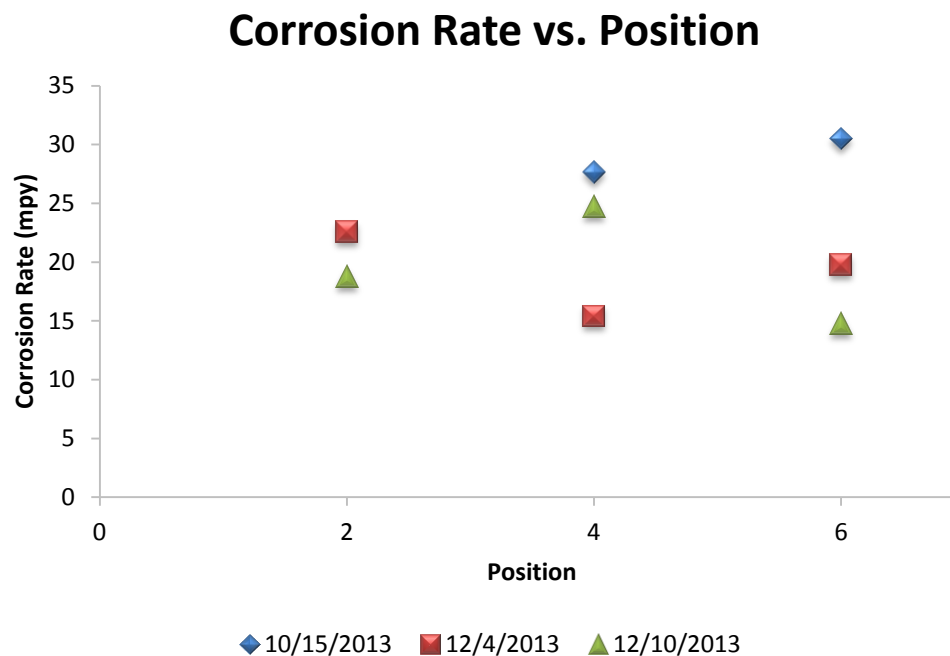
Figure 4-7 Corrosion Rate vs. Position for pure Mg thin films. Observation of this plots leads to the conclusion that position does not affect the corrosion rate of the thin film sample.

The open circuit potential for these films was also compared to the deposition rate, thickness, and position. The findings for the OCP vs. thickness imply that there is no correlation between these OCP and thickness for thickness from 1.57 to 4.11μm (Figure 4-9). The graph of OCP vs. Deposition Rate implies that with decreasing deposition rate the OCP decreases from -1.685V at 126.6 Å/s to -1.902V at 9 Å/s. (Figure 4-8). The graph of OCP vs. Position (Figure 4-10) seems to imply that OCP decreases with increasing position (from -1.902V at Position 6, which has an angle of 32° to -1.69V at Position 2, which has an angle of 0°). That is to say that OCP increases with increasing deposition distance and deposition angle. This relationship between OCP matches the findings by Stormer et al. [11].Stormer found that corrosion rate increased with increasing deposition angle and pressure. However, it was concluded that this was due to an increase in surface roughness (surface area) for 10 nm at low angle and low pressure to 200 nm at high deposition angle and high pressure. The OCP (corrosion potential) is not affected

by the size of the area so this increase in surface roughness does not explain the increase in OCP.

Stormer concluded that the increase in OCP was a result of a finer microstructure with smaller

column diameter, which results in a large number of grain boundaries exposed to the electrolyte.

At low deposition angle the hcp basal planes grow parallel to the surface, so that most of the

exposed area consists of these densely packed (0001) planes. Increasing the deposition angle

results in a disruption of this surface morphology and side faces of the columns are exposed to the

electrolyte and the potential decreases because these other faces are more reactive.

Sikora et. al. [29] observed that the open circuit potential of nanocrystalline AA5083

alloy had was 100mV than that of conventional AA5083. This result could be due to the grain

size of the nanocrystalline material being much smaller (80-200nm) than the grain size of the

conventional alloy (40µm). A similar trend is demonstrated for the pure Mg thin films. The films

have a lower OCP by over 200mV (-1.6V for bulk Mg to about -1.8V for pure Mg films) and the

open circuit potential is reduce further with increasing deposition angle, which increases the self-

shadowing that occurs during deposition and results in thinner columns and smaller grains. This

results in an increase in the ratio of grain boundaries to in-grain surface area and this causes a

decrease in open circuit potential as the grain boundaries are more reactive.

Open Circuit Potential vs Deposition Rate
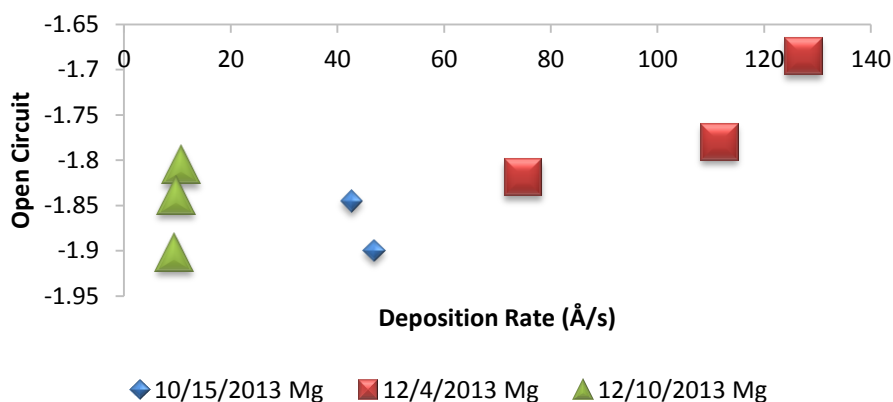
Figure 4-8 Open Circuit Potential vs. Deposition Rate for pure Mg thin films. Observation of this plots leads to the conclusion that deposition rate does not affect the open circuit potential of the thin film sample.

Open Circuit Potential vs. Thickness
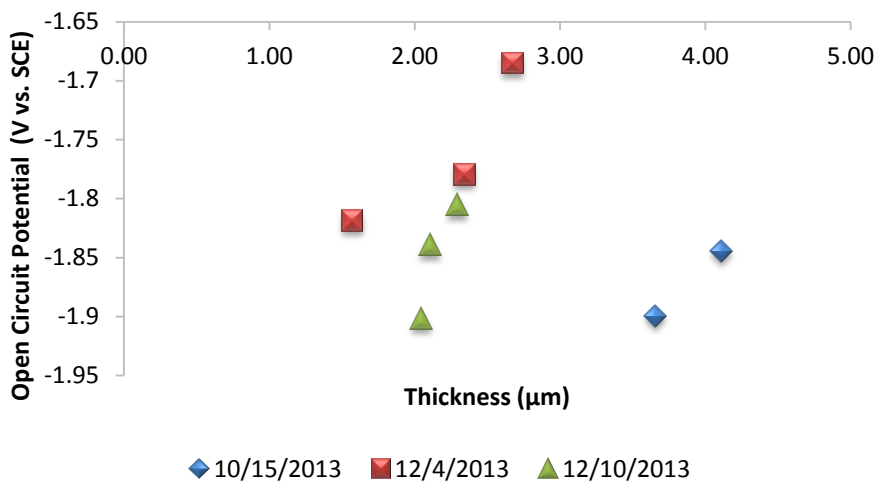
Figure 4-9 Open Circuit Potential vs. Thickness for pure Mg thin films. This figure does not show any observable trend between thin film thickness and open circuit potential.

Open Circuit Potential vs Position

◆ 10/15/2013 Mg   ■ 12/4/2013 Mg   □ 12/10/2013 Mg
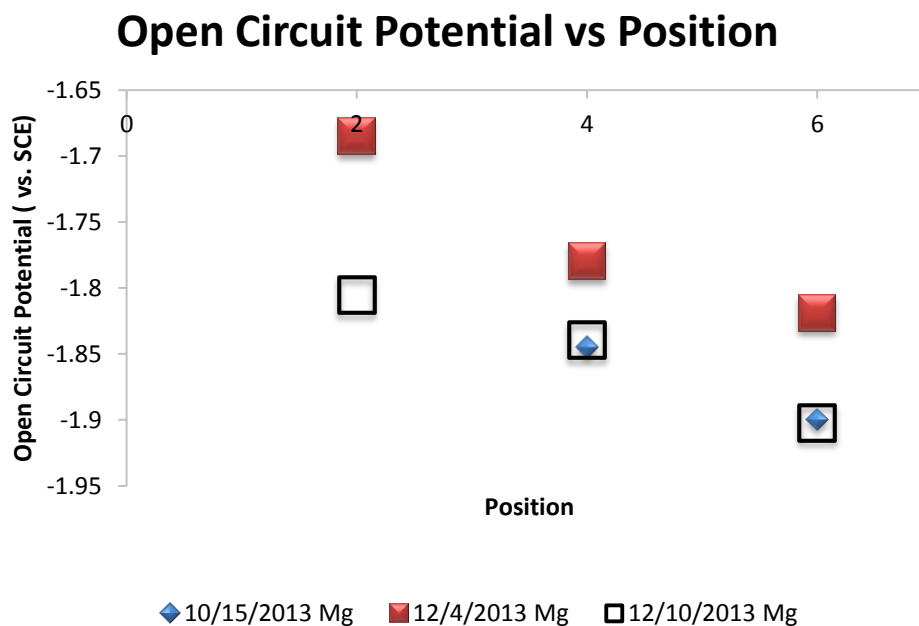
Figure 4-10 Open Circuit Potential vs. Position for pure Mg thin films. As the position increases the open circuit potential decreases. This is most likely an effect of the increasing deposition angle of the thin film as discussed in Chapter 2.

The fact that there is no correlation between the corrosion rate and deposition rate or thickness means that corrosion rate can be compared for films of differing thicknesses and deposited at different deposition rates as these parameters do not have a significant effect on the electrochemical properties. The decrease in open circuit potential with increasing deposition angle means that open circuit potential can be manipulated for pure Mg depositions. This could be beneficial as materials with low open circuit potentials (active materials) offer corrosion protection materials with higher open circuit potentials (less active or noble materials).

4.2 Pure Magnesium Thin Films

In this section, observations about thin film morphology from FESEM imaging and structural analysis from XRD will be discussed for each deposition. The analysis for each technique was carried out as described in Chapter 3.

4.2.1 Morphology and Structure

Pure Mg films were prepared with different deposition rates as described in the previous section. The morphology and structure of these thin films were analyzed using FESEM imaging and GIXRD analysis. The 12/10/2013 deposition was performed with the lowest deposition rate of the pure Mg samples. At first glance, the films appear to be a dull gray (as seen in Figure 4-11).
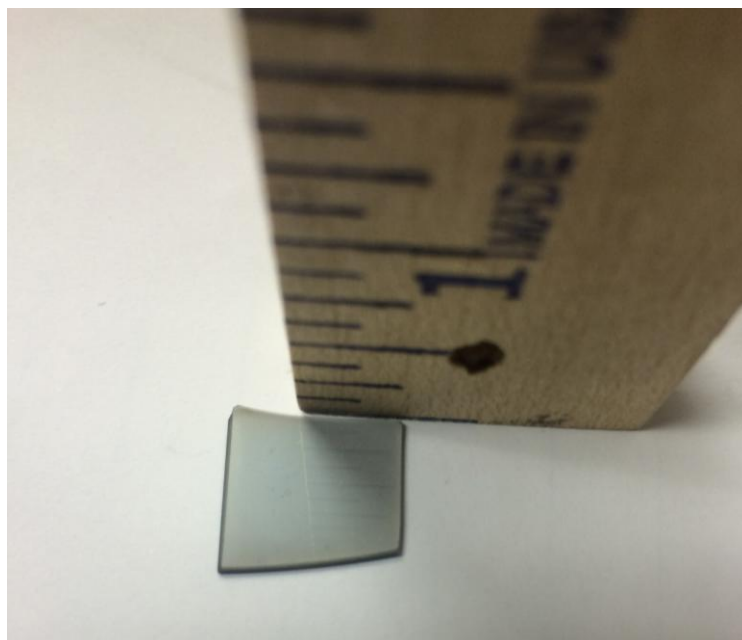
Figure 4-11 Picture of a pure Mg thin film. This film was deposited on 12/10/2013 and is from Position 1. The gray color of the film can be seen as well as the reflection of the ruler in the surface of the thin film.

The pure Mg thin films are not as reflective as Mg-Al thin films, which will be shown in Section 4.3. The samples from this run show a columnar growth structure that is characteristic of magnesium thin films. The columns in these samples are relatively thick with a column width of about 500nm. The side-by-side cross sections can be compared in Figure 4-12. The samples from the 12/10/2013 deposition are dense compared to pure Mg samples with faster deposition rates. The surface of this film is relatively smooth; however, it is becoming rougher as the deposition angle increases from Position 1 to Position 7. The edges of the hexagonal plates that are characteristic of the hexagonal close-packed magnesium crystal structure can be seen on the surface in Figure 4-13.

Cross Sections of Pure Mg Thin Films at 14,000 Times

Position 1 Deposition Rate: 10.86 Å/s

Position 3 Deposition Rate: 9.97 Å/s

Position 5 Deposition Rate: 9.47 Å/s

Position 7 Deposition Rate: 9.27 Å/s
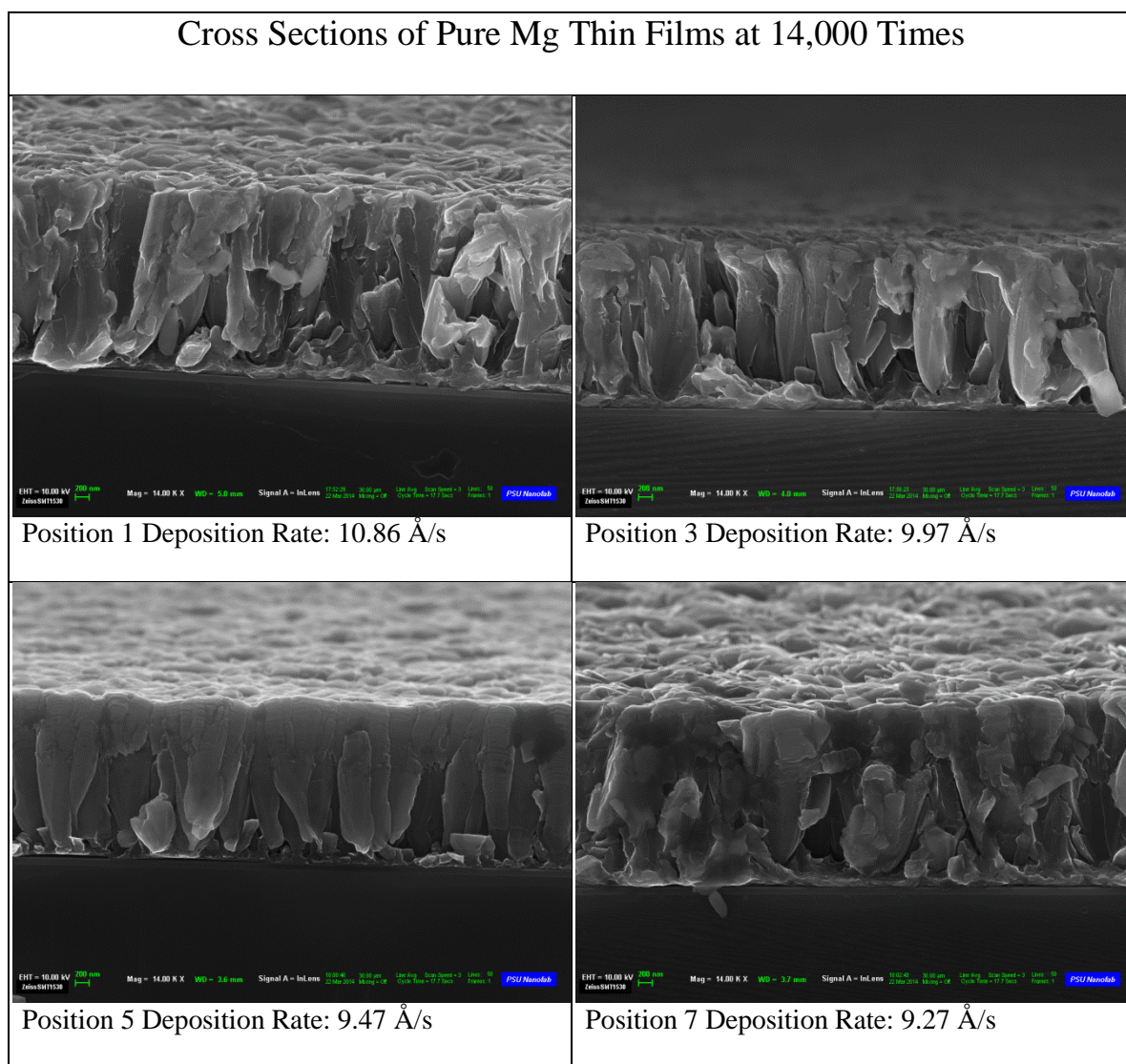
Figure 4-12 Cross-sections of pure Mg thin films grown at a target deposition of 7 Å/s. The films are imaged at a magnification of 14,000 times and a tilt of 10° to reveal the surface features of the film. These films are dense compared to Mg films deposited at higher rates. The slower rate has given the films time to grow in a dense and uniform structure. The surface is smooth compared to other pure Mg thin films. The films shown here were deposited on 12/10/2013. The deposition rates and position of each sample is shown below the picture.
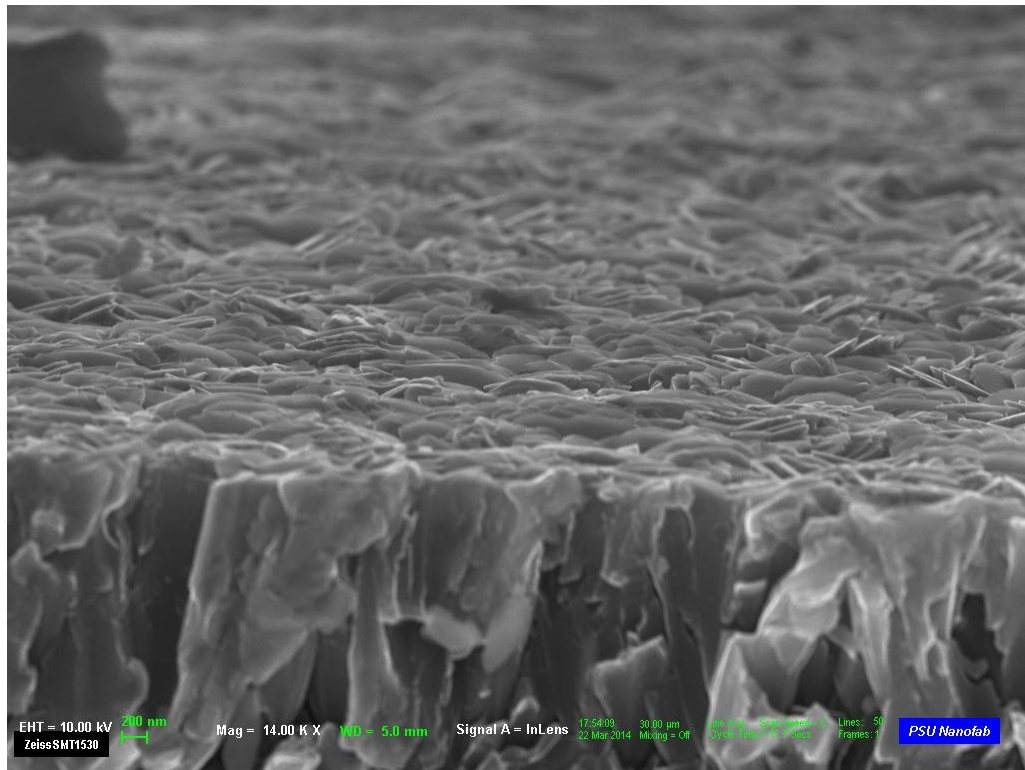
Figure 4-13 The surface of the 12/10/2013 Position 1 pure Mg thin film sample is pictured at 14,000 times magnification. The deposition rate for this film was 10.86 Å/s. The edges of the hexagonal plates are characteristic of magnesium structure can be seen. The film is relatively smooth compared to pure Mg thin films with higher deposition rates, such as those shown in Figure 4-16.

The growth mechanism of the thin film can be seen particularly well for the cross section of Position 5, which is shown in a larger image in Figure 4-14. In this figure the columnar growth of the thin film can be seen clearly. In this case, the columns are narrow at the base of the film and increase in width as they grow towards the surface of the film. This growth is characteristic of Zone 2 of the structure zone model mentioned in Chapter 2. Zone 2 exhibits a thick columnar growth due to a mixture of shadowing effects and surface diffusion. The x-ray diffraction pattern for this film matches the profile for a pure magnesium hexagon close-packed structure. The (002) peak is significantly higher than the other Mg peaks, but all of the Mg peaks are present in the pattern, which can be seen in Figure 4-15.
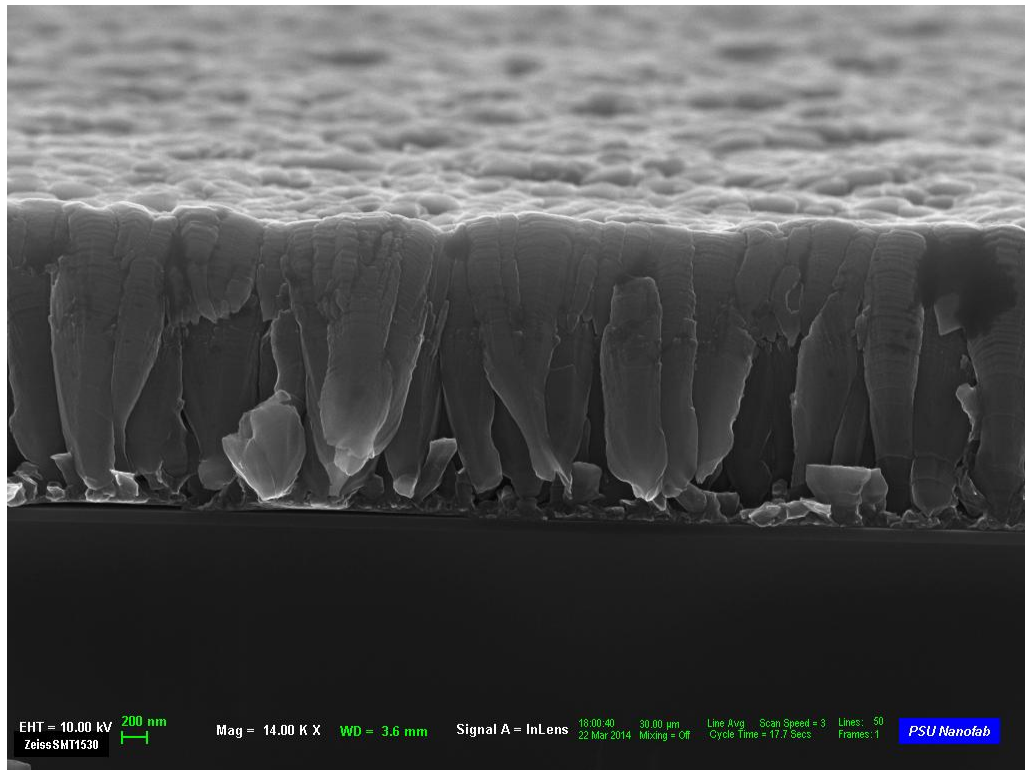
Figure 4-14 FESEM image of the cross section a pure Mg film deposited on 12/10/2013. The image was taken at a 14,000 times magnification and an angle of 10° in order to reveal the surface of the thin film. This image shows the columnar growth of a pure Mg thin film with relatively thick columns. The columns are narrow at the base of the film and they increase in width as they grow toward the surface of the film.
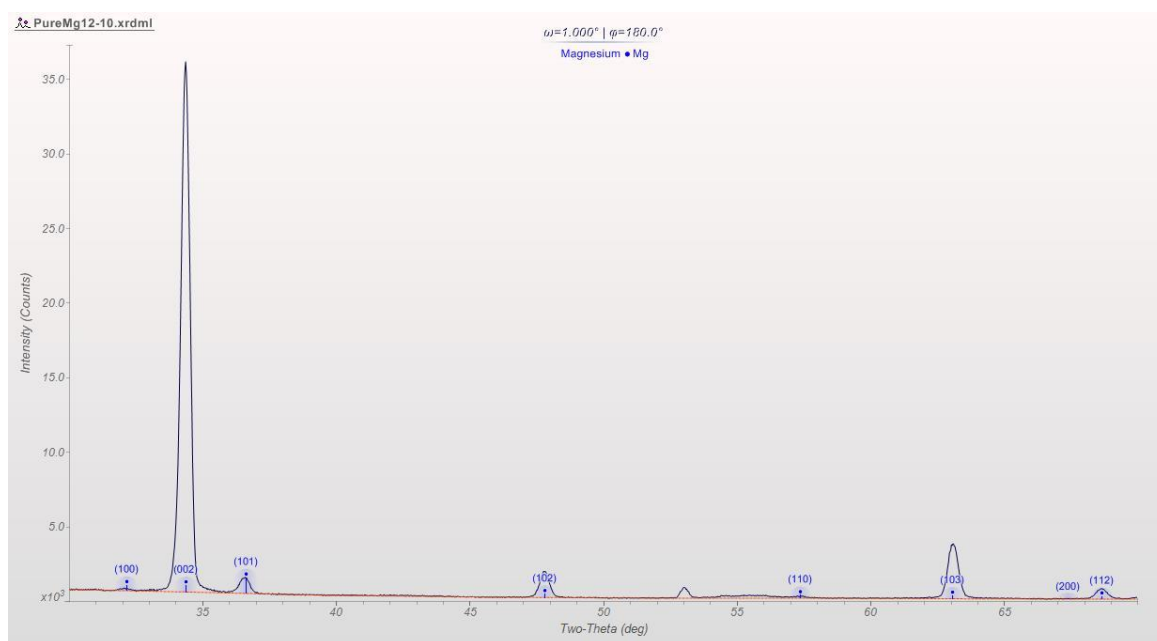
Figure 4-15 XRD Pattern of the 12-10 Position 1 thin film. The pattern matches the profile of a pure Mg alpha phase. The (002) peak shows a much higher intensity than the other Magnesium peaks, which implies that the film has a significant preferred orientation. The unidentified peak at a 2 theta of 53° corresponds to the single crystal Si substrate.

The 12/4/2013 pure Mg thin film was deposited at a target rate of 75 Å/s. The cross sections of the samples from this deposition are shown in Figure 4-16. The cross section of the film shows a columnar structure with narrow columns that stay narrow as they grow towards the films surface. This growth is characteristic of Zone 1 of the structure zone model. The deposition is occurring rapidly and so the effects of shadowing are high and surface diffusion is very low. The result is a film that is less dense than the 12/4 thin film (shown in Figure 4-14). The narrow columns are about 200nm thick as opposed to the 500nm thick columns that the 12/4 thin films exhibit. The surface of the 12/10 thin film is also very rough. The hexagonal plates are prominent throughout the surface of the film and the surface area is much higher than for the 12/10 film. The x-ray diffraction pattern from Position 1 of the 12/4 peak matches the profile of the pure Mg alpha phase (Figure 4-17). The pattern shows similar intensities for reflections off of several different Mg planes. The film shows a preferred orientation to the (102) plane as the peak of this

plane is high relative to the other peaks in the XRD pattern. The (002) peak is not preferred as it was in the 12/10 run. This shows that there was a significant change in the crystal structure of the films with a change in deposition rate from 10.86 to 126.60 Å/s.
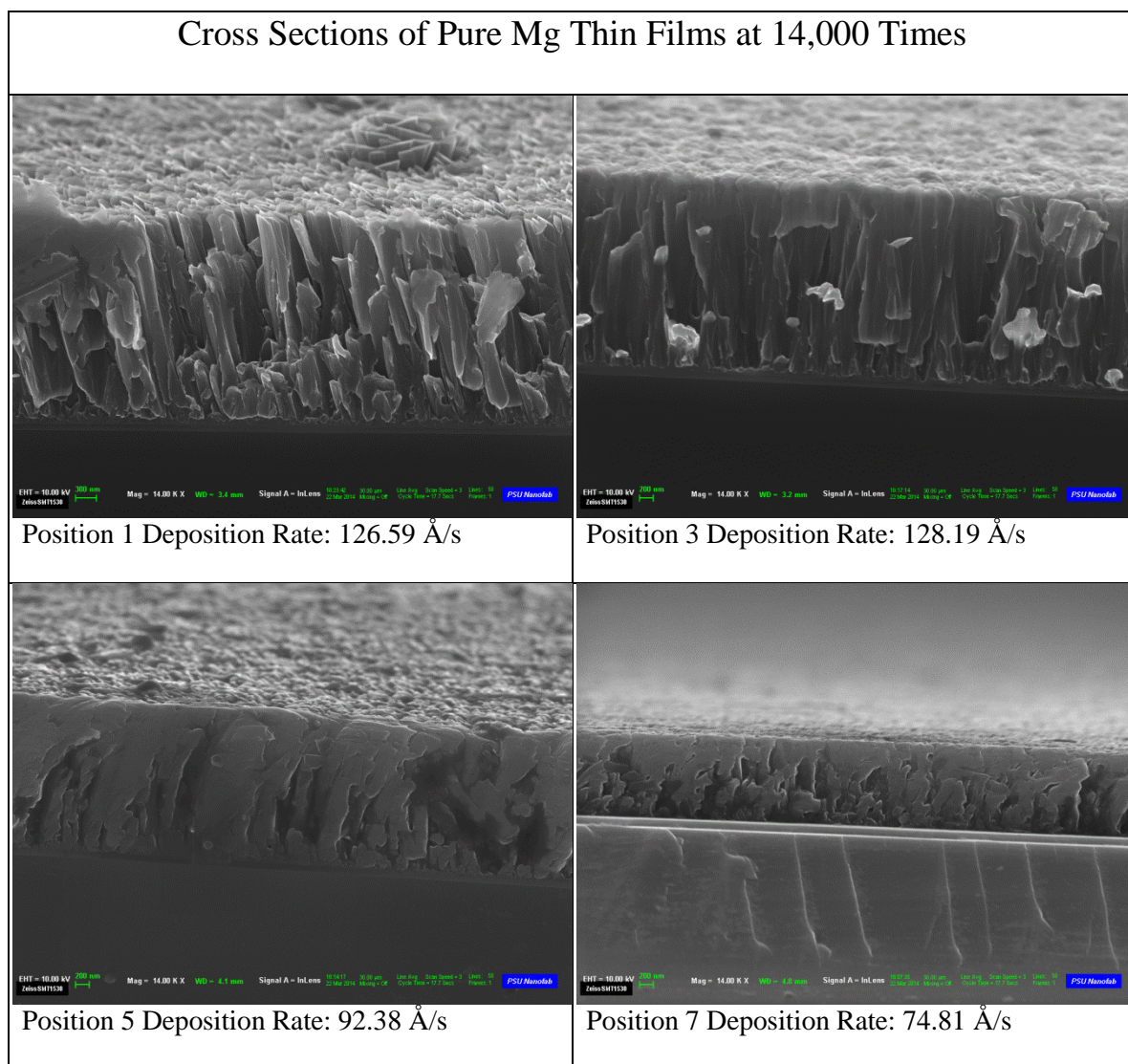
Figure 4-16 FESEM image of the cross section a pure Mg film deposited on 12/4/2013. The image was taken at a 14,000 times magnification and an angle of 10° in order to reveal the surface of the thin film. This image shows the columnar growth of a pure Mg thin film with thin columns. The columns are narrow at the base of the film and they do not increase significantly in width as they grow towards the surface of the thin film.
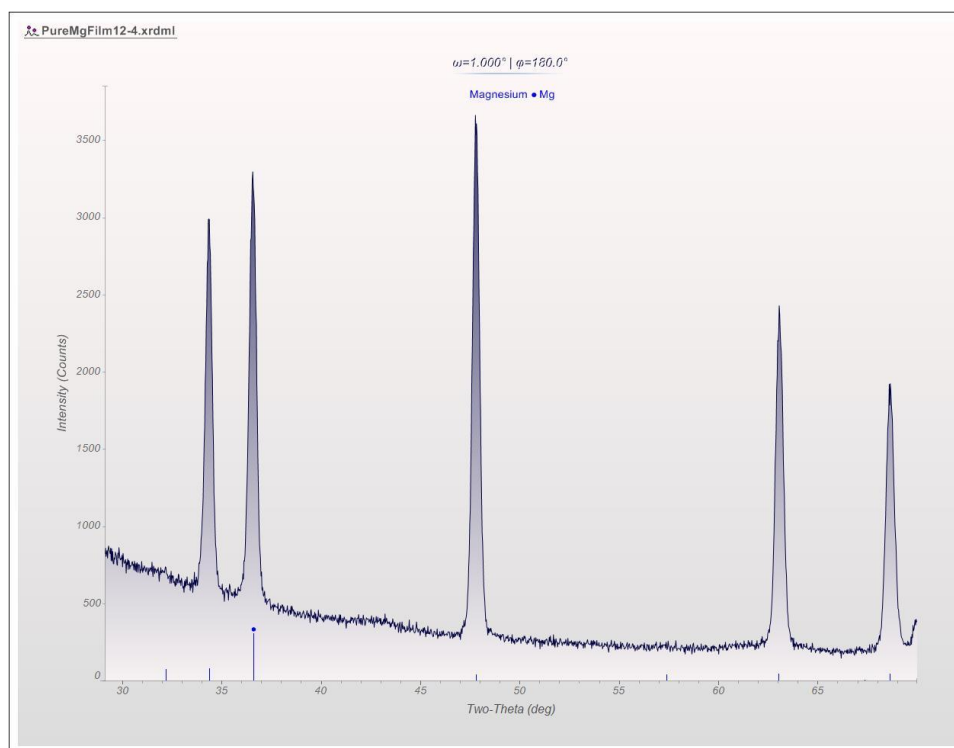
Figure 4-17 XRD Pattern for the 12/4 Position 1 thin film. The pattern matches the profile of a pure Mg alpha phase.

4.2.2 Electrochemical Results

Electrochemical tests were conducted to determine the corrosion resistance of the pure

Mg thin films. Polarization Resistance and EIS were used to determine the corrosion rate and

Potentiodynamic tests were used to determine the corrosion current density. For each run,

samples were taken from Positions 2, 4, and 6 for electrochemical testing. For each position, 3

samples were tested using Polarization Resistance and EIS and two samples were testing using a

Potentiodynamic scan, one each for the cathodic and anodic scans.
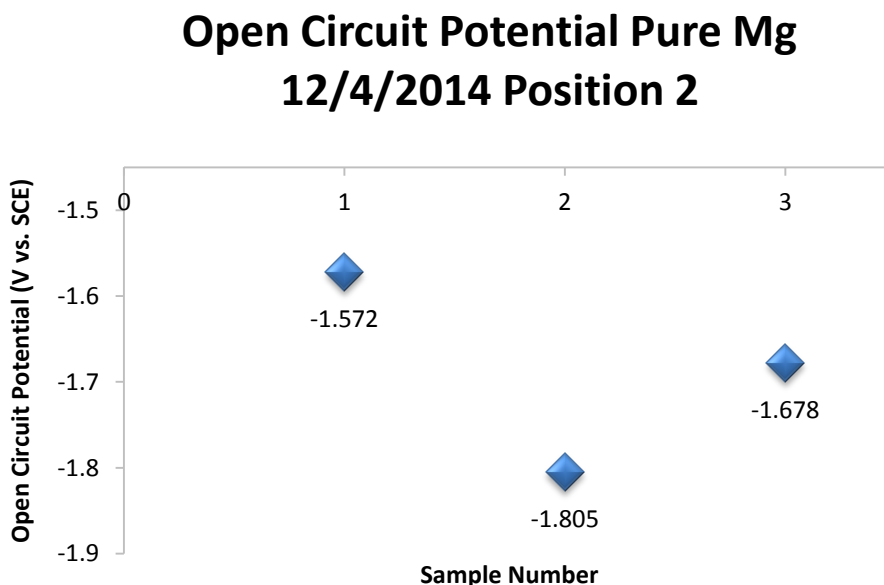
Figure 4-18 Plot of the Open Circuit Potential values determined for Position 2 of a pure Mg deposition run on 12/4/2014. This plot shows the values from three different samples that were averaged to provide a more reliable data point for analysis.

Figure 4-18 shows the open circuit potential values determined for Position 2 of the pure

Mg run. Electrochemical results were collected for 3 different samples and the results were used

to determine a mean value and a 95% Confidence Interval. Figure 4-19 shows the corrosion rates

determine using Polarization Resistance for the same 3 samples from Position 2. These rates were

then averaged to calculate a mean corrosion rate and a 95% Confidence Interval. This process was used to determine the mean electrochemical values for each position that was analyzed. For Potentiodynamic scans, one cathodic scan and one anodic scan was conducted for each position. If three scans were not used to determine a mean value, due to leaking or cracking of a sample, it was noted.

Corrosion Rate Pure Mg 12/4/2014 Position 2
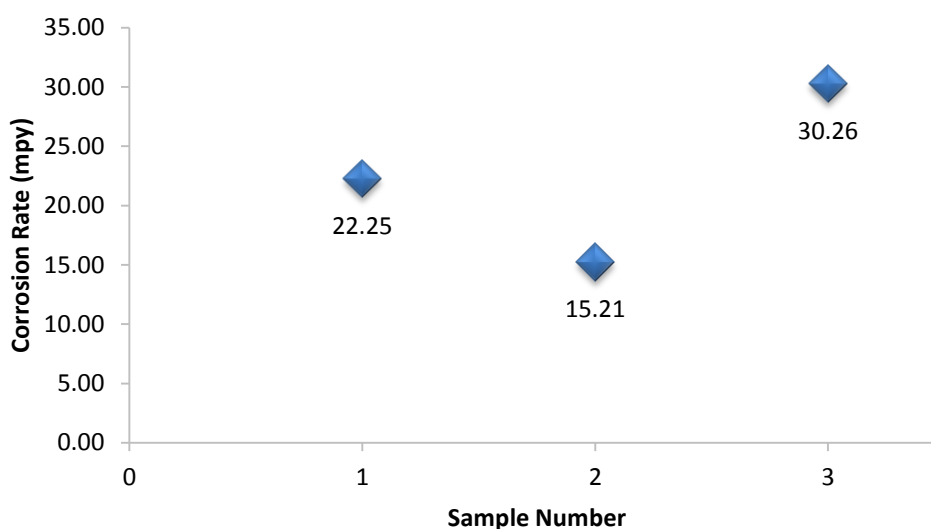
Figure 4-19 Plot of the Corrosion Rate values determined by Polarization Resistance for Position 2 of a pure Mg deposition run on 12/4/2014. This plot shows the values from three different samples that were averaged to provide a more reliable data point for analysis.

For the 12/4/2014 run of pure Mg at a high deposition rate, the corrosion rate results for each sample are shown in Figure 4-20 and Figure 4-21. There is not a trend between position and corrosion rate, which implies that there is not a trend between corrosion rate and deposition angle, deposition rate, or deposition distance because these parameters are determined by the position. The corrosion rates determine for this run do not differ significantly from the corrosion rates determined for other pure Mg depositions.

Mean Corrosion Rate (PR) of Pure Mg
12/4/13
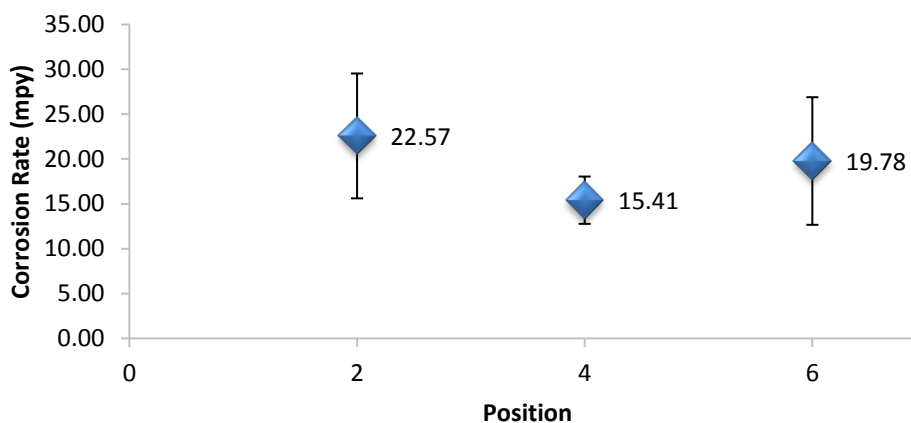
Figure 4-20 Plot of the Mean Corrosion Rate values determined by Polarization Resistance for a pure Mg deposition run on 12/4/2014. This plot shows the mean values for each position. There is no trend for corrosion rate and position. The corrosion rates also do not differ significantly from other pure Mg runs. The error bars shown are based on a 95% Confidence Interval. The error bars for Position 4 are covered by the symbol.

Mean Corrosion Rate (EIS) of Pure Mg
12/4/13
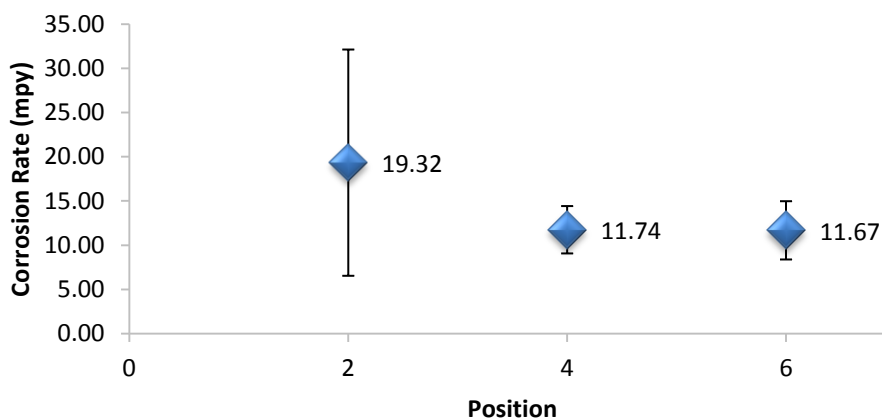
Figure 4-21 Plot of the Mean Corrosion Rate values determined by EIS for a pure Mg deposition run on 12/4/2014. This plot shows the mean values for each position. There is no trend for corrosion rate and position. The corrosion rates also do not differ significantly from other pure Mg depositions. The error bars shown are based on a 95% Confidence Interval. The Confidence Interval Bars for Positions 4 and 6 are cover by the symbol.

The OCP results for the 12/4/2013 deposition are shown in Figure 4-22. The OCP value decreases by 130mV from Position 2 to Position 6. This supports the trend that was observed in section 4.1, that OCP decreases with increasing deposition angle.

Mean Open Circuit Potential of Pure Mg 12/4/2014
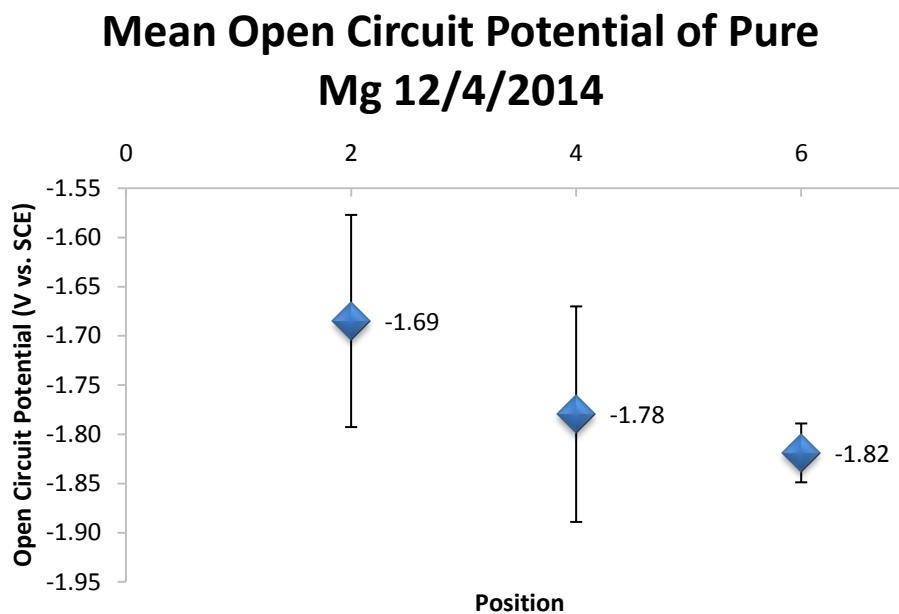
Figure 4-22 Plot of the Mean Open Circuit Potential values for a pure Mg deposition run on 12/4/2014. This plot shows the mean values for each position. The OCP decreases with increasing position, which corresponds to increasing angle of deposition. The error bars shown are based on a 95% Confidence Interval.

The rest of the electrochemical results were placed in plots together so that overall trends can be observed. The position, deposition rate, corrosion rates, and open circuit potential for each pure Mg deposition are shown in Table 4-7. The data presented in this table show the average values calculated from three different samples that were tested at each position.

Table 4-7 Data for pure Mg depositions. The Table is organized by deposition date and position. The deposition and electrochemical data for each position is displayed.

Date	12/4/2013			12/10/2013			10/15/2013		
Position	2	4	6	2	4	6	2	4	6
Thickness (μm)	2.68	2.35	1.57	2.29	2.11	2.04	3.33	4.11	3.66
Deposition Rate (Å/s)	127.4	111.67	74.81	10.62	9.75	9.45	42.68	52.71	46.89
Open Circuit Potential (V. vs. SCE)	-1.690	-1.780	-1.820	-1.806	-1.840	-1.902	-1.608	-1.845	-1.900
Corrosion Rate PR (mpy)	22.57	15.41	19.78	18.76	24.70	14.74	318.40	30.51	18.60
Corrosion Rate EIS (mpy)	19.32	11.74	11.67	11.32	12.81	9.10	78.20	19.18	15.19

Mean Corrosion Rate (PR) of Pure Mg
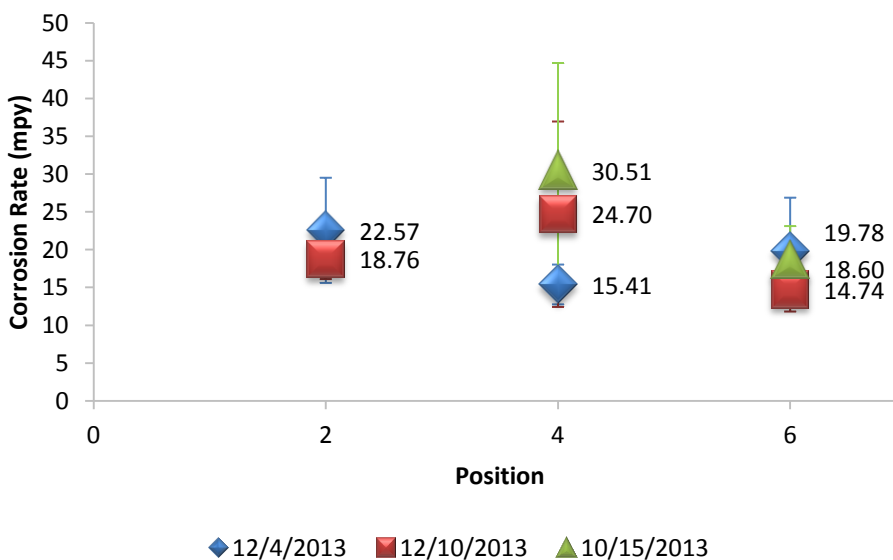
Figure 4-23 Plot of the Mean Corrosion Rate values determined by Polarization Resistance for pure Mg thin films tested in artificial seawater. This plot shows the mean values for each position. There is no trend for corrosion rate and position. The error bars shown are based on a 95% Confidence Interval.

The mean corrosion rate of the pure Mg films is plotted against position in Figure 4-23.

There does not appear to be a correlation between the sample position and the corrosion rate. This

implies that there is little effect on corrosion rate from deposition rate or deposition angle as these

parameters both vary with position. Figure 4-24 plots the Corrosion Rate against Deposition Rate.

Even with a significant change in deposition rate the corrosion rate doesn't change, which shows

that the corrosion rate is driven by other properties of the thin film. The corrosion rates

determined by EIS are lower than the rates determined by Polarization Resistance and they have a

smaller 95% Confidence Interval as shown in Figure 4-25.
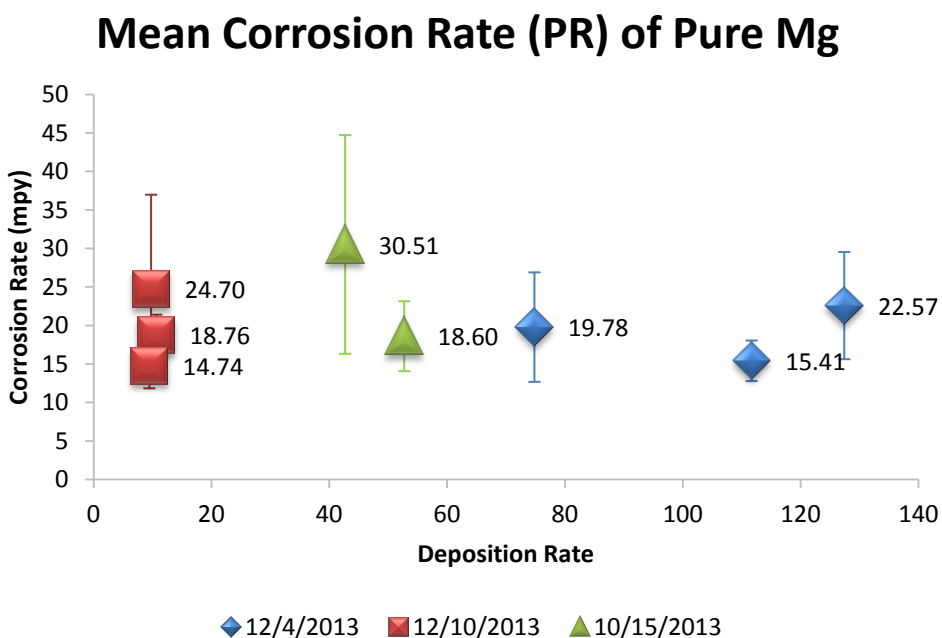
Figure 4-24 Plot of the Mean Corrosion Rate values determined by Polarization Resistance for pure Mg thin films tested in artificial seawater. This plot shows Corrosion Rate vs. Deposition Rate. There is no trend for corrosion rate and deposition rate. The error bars shown are based on a 95% Confidence Interval.

Mean Corrosion Rate (EIS) of Pure Mg
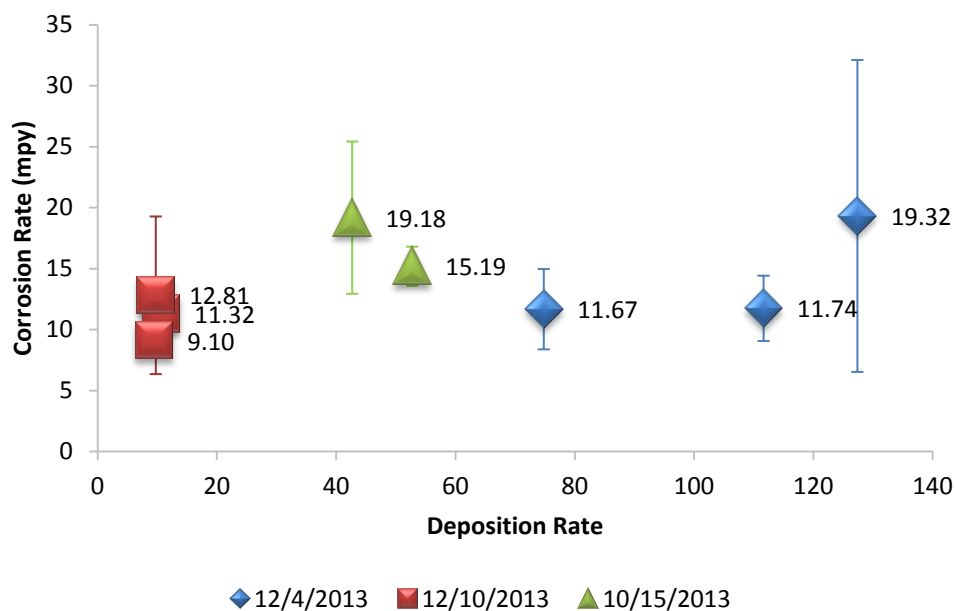
Figure 4-25 Plot of the Mean Corrosion Rate values determined by EIS for pure Mg thin films tested in artificial seawater. This plot shows Corrosion Rate vs. Deposition Rate. There is no trend for corrosion rate and deposition rate. The error bars shown are based on a 95% Confidence Interval.

The open circuit potential of the pure Mg depositions is plotted against deposition angle in Figure 4-26. The open circuit potential decreases as deposition angle increases. Figure 4-27 seems to imply the open circuit potential increases with increasing deposition rate. Both of these trends were discussed in section 4.1. Future work should be done to isolate the deposition angle from the deposition rate in order to determine which parameter has the larger effect on the open circuit potential.

Mean Open Circuit Potential of Pure Mg
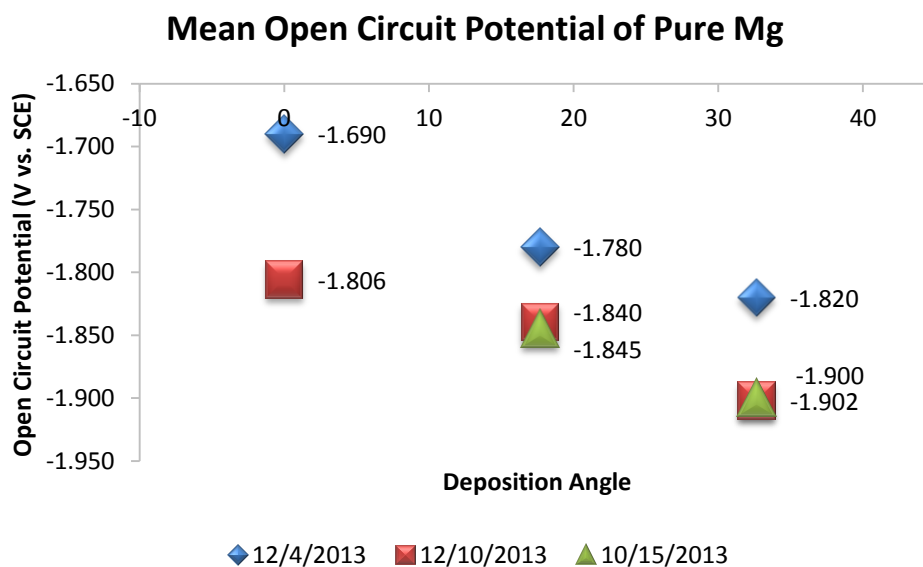
Figure 4-26 Plot of the Open Circuit Potential vs. deposition angle values for pure Mg thin films tested in artificial seawater. This plot shows Open Circuit Potential vs. Deposition Angle. As the deposition angle increases the open circuit potential decreases.

Mean Open Circuit Potential of Pure Mg
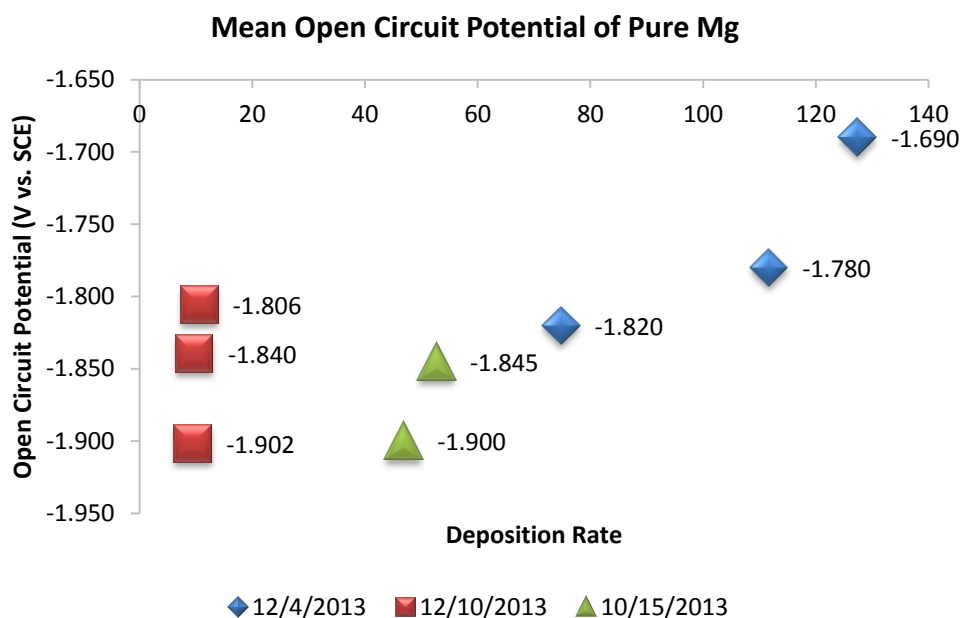
Figure 4-27 Plot of the Open Circuit Potential vs. Deposition Rate values for pure Mg thin films tested in artificial seawater. This plot shows Open Circuit Potential vs. Deposition Rate. As the deposition rate increases the open circuit potential increases.

4.3 Mg-Al Thin Films

4.3.1 Composition, Morphology, and Structure

Binary films consisting of Mg and Al were deposited using two electron beam guns simultaneously. The composition of the films was modified by changing the relative deposition rate of each material. The deposition parameters are presented in Table 4-8. Quantitative composition was determined using EDS analysis. The deposition rate ratio was used to target a composition ratio. This was very successful as the deposition ratio of the 2/26 deposition was 0.338 and the measured composition of Position 4 (the middle position) was 39.27 wt. % Al. For the 6/11 run deposition rate ratio was 0.087 and the composition of Position 4 was 8.04 wt. % Al. This shows that there was success to within 5% of the target composition based on the deposition rate ratios. Once the composition was determined the films were analyzed using FESEM and XRD to observe the microstructure and determine the phases present in the film.

Table 4-8 Data for Mg-Al depositions. The Table is organized by deposition date and position. The deposition parameters for each sample are displayed.

Date	2/26/2014			6/11/2014		
Average QCM Rate for Mg (Å/s)	15.22			22.00		
Average QCM Rate for Al (Å/s)	5.14			1.92		
Deposition Rate Ratio Al/Mg	0.338			0.087		
Position	2	4	6	2	4	6
Angle	0	17.6	32.6	0	17.6	32.6
Thickness (µm)	1.868	1.636	1.339	1.979	1.400	0.865
Deposition Rate (Å/s)	34.58	30.30	24.79	32.98	23.33	14.42

The Mg-Al thin films deposited on 2/26/2014 were analyzed using EDS and found to have a composition ranging from 18 wt. % at Position 1 to 58 wt. % at Position 7 as shown in Table 4-9. This run provided a very wide range of Al composition to analyze via SEM and XRD analysis.

Table 4-9 Composition of 2/26/2014 Mg-Al thin film determined by EDS. The Mg/Al ratio, wt. % Al, and at. % Al has been calculated. The results shown come from averages for each sample that were taken from collection of two EDS spectra for each Position.

Compositional Analysis of 2/26/2014 Mg-Al Thin Film							
	Position 1	Position 2	Position 3	Position 4	Position 5	Position 6	Position 7
wt. % Al/% Mg-ratio	0.22	0.31	0.37	0.65	0.76	1.07	1.42
wt. % Al	18.36	23.49	26.86	39.27	43.22	51.70	58.71
at. % Al	16.34	21.05	24.19	35.96	39.80	48.18	55.26

FESEM images of this Mg-Al run can be seen in Figure 4-29. The Mg-Al films are dense compared to the pure Mg thin films. The surface is very smooth, which explains why the surface of Mg-Al is reflective and shiny like a mirror (the surface is shown in Figure 4-28 Figure 4-30). The hexagonal structure that could be observed in the pure Mg thin films is not present even in Position 1 which contains 18.36 wt. % Al.
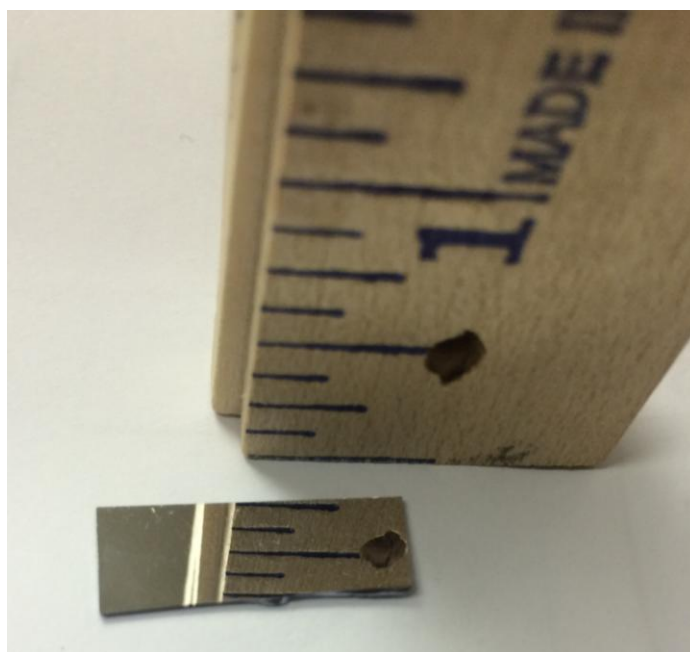
Figure 4-28 Picture of a Mg-Al thin film. This Mg-Al thin film was deposited on 6/11/2014 and is from Position 3, which is 5.62 wt. % Al. The film is very reflective and the reflection of the ruler is very clear.

Cross Sections of Mg-Al Thin Films at 14,000 Times Magnification

Position 1   18.36 wt. % Al

Position 3   26.86 wt. % Al

Position 5   43.22 wt. % Al

Position 7   58.71 wt. % Al
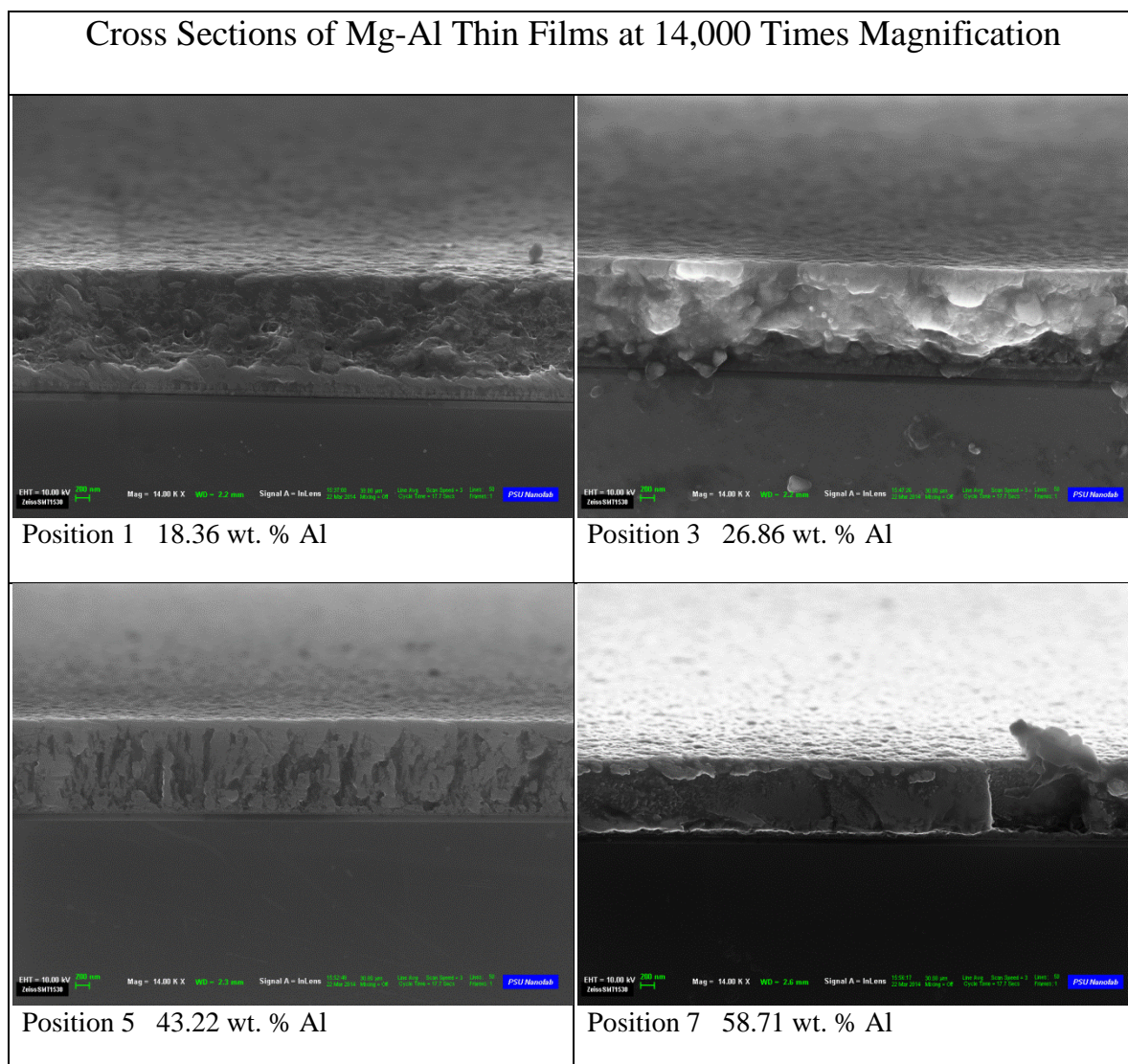
Figure 4-29 FESEM images of the cross section of Mg-Al thin films deposited on 2/26/2014. The image was taken at a 14,000 times magnification and an angle of 10° in order to reveal the surface of the thin film. These images show the dense growth of the Mg-Al binary system. The surface is extremely smooth compared to pure Mg thin films.
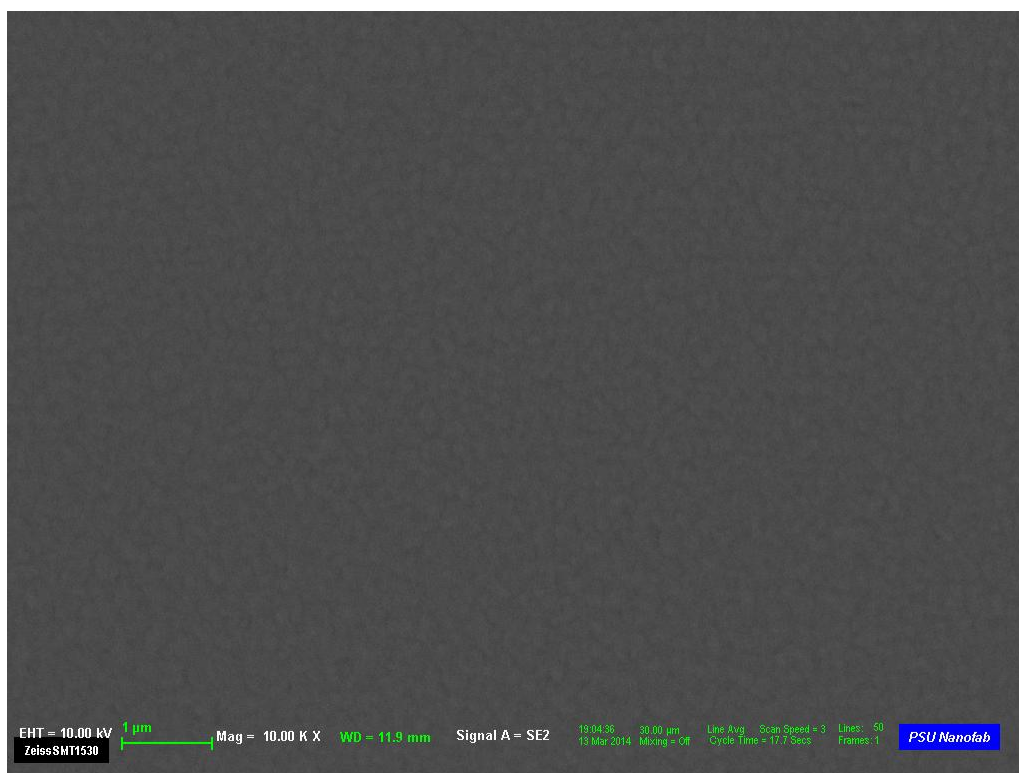
Figure 4-30 FESEM image of the surface of a Mg-Al thin film at 10,000 times magnification. The image is of Position 1 of the 2/26/2014 Mg-Al run, which contains 18.36% Al. The surface is smooth even at 10,000 times magnification. There are no hexagonal plates showing on the surface of the specimen.
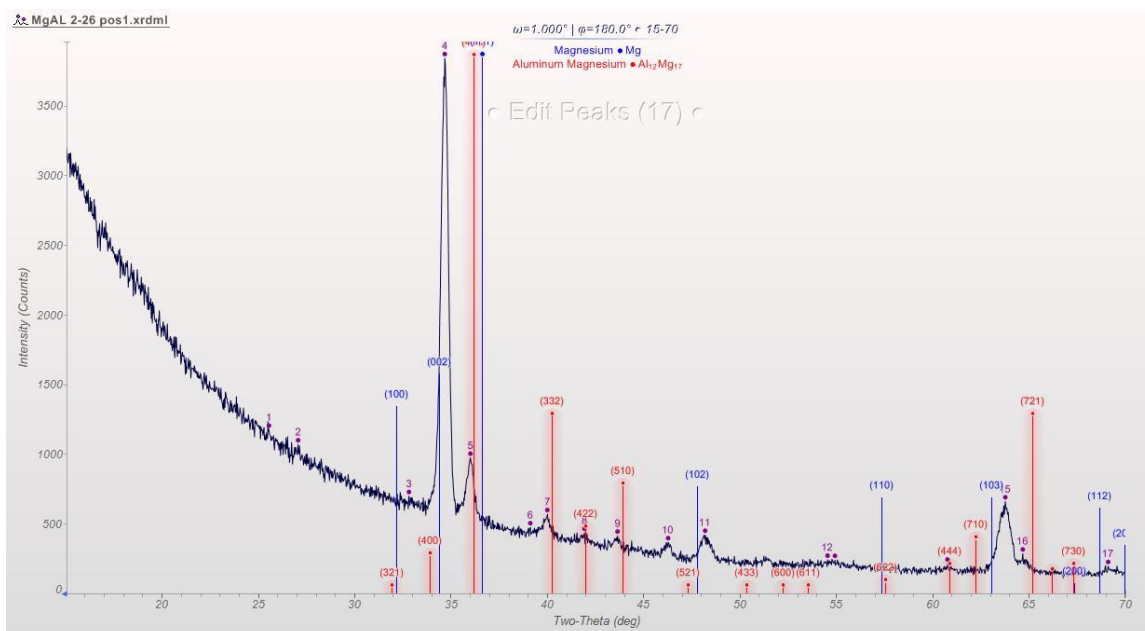
Figure 4-31 XRD Pattern for the 2/26 Position 1 thin film. This film contains 18.36 wt. % Al. The pattern corresponds to a mixed phase film with alpha Mg and $Al_{12}Mg_{17}$ phase.

The XRD pattern of Position 1 reveals that there are two phases present in this thin film. The alpha Mg phase is present mixed with the $Mg_{12}Al_{17}$ phase. The peaks for the alpha Mg phase decrease and the peaks for the $Mg_{12}Al_{17}$ increase as Al content increases. By the time the Al content has increased to 43.22 wt. % in Position 5 the film is dominated by the $Mg_{12}Al_{17}$ phase as seen in Figure 4-32.
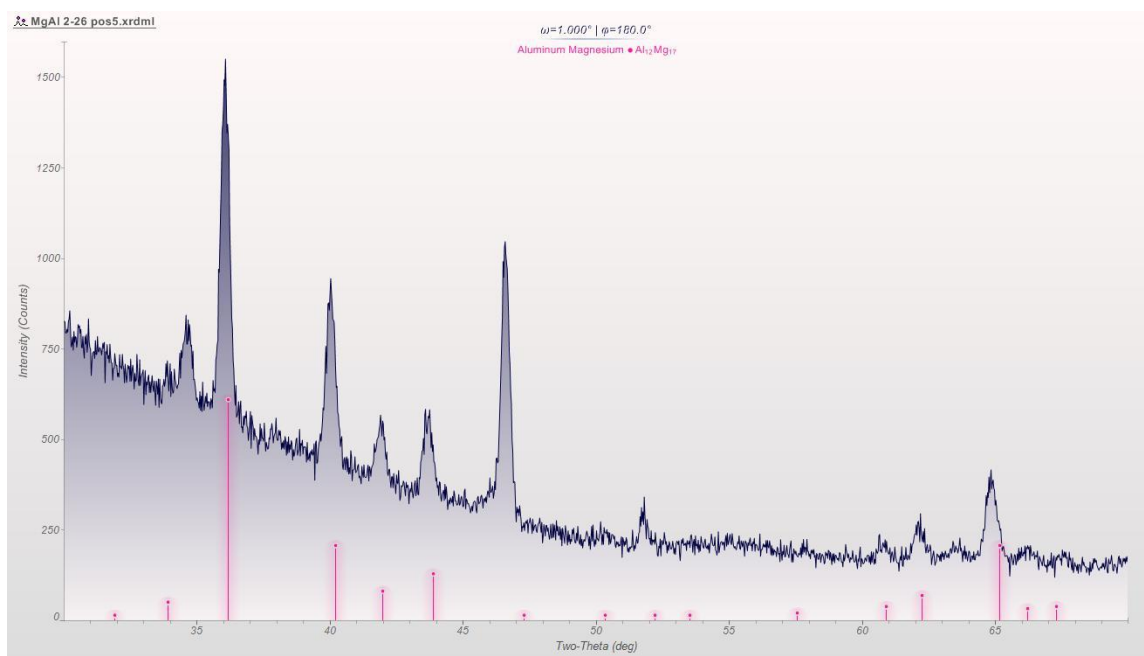
Figure 4-32 XRD Pattern for the 2/26 Position 5 thin film. This film contains 43.22 wt. % Al. The pattern shows only the $Mg_{17}Al_{12}$ diffraction pattern.

The Mg-Al deposition performed on 6/11/2014 was done with intention of having significantly less Al content. The EDS analysis showed that the Al content ranged from 2.97 wt. % to 24.7 wt. % (Table 4-10). The FESEM cross-sections show that at just 2.97 wt. % Al the film structure is completely different from what was observed for the pure Mg thin films. The films are dense and have a smooth surface.

Table 4-10 Composition of 6/11/2014 Mg-Al thin film determined by EDS. The Mg/Al ratio, wt. % Al, and at. % Al has been calculated. The results shown come from averages for each sample that were taken from collection of two EDS spectra for each Position.

Compositional Analysis of 6/11/2014 Mg-Al Thin Film							
	Position 1	Position 2	Position 3	Position 4	Position 5	Position 6	Position 7
wt. % Al/% Mg-ratio	0.03	0.04	0.06	0.09	0.11	0.20	0.33
wt. % Al-quantitative	2.97	3.41	5.62	8.04	9.94	16.95	24.70
at. % Al-quantitative	2.29	2.54	4.16	5.57	6.81	11.64	17.21
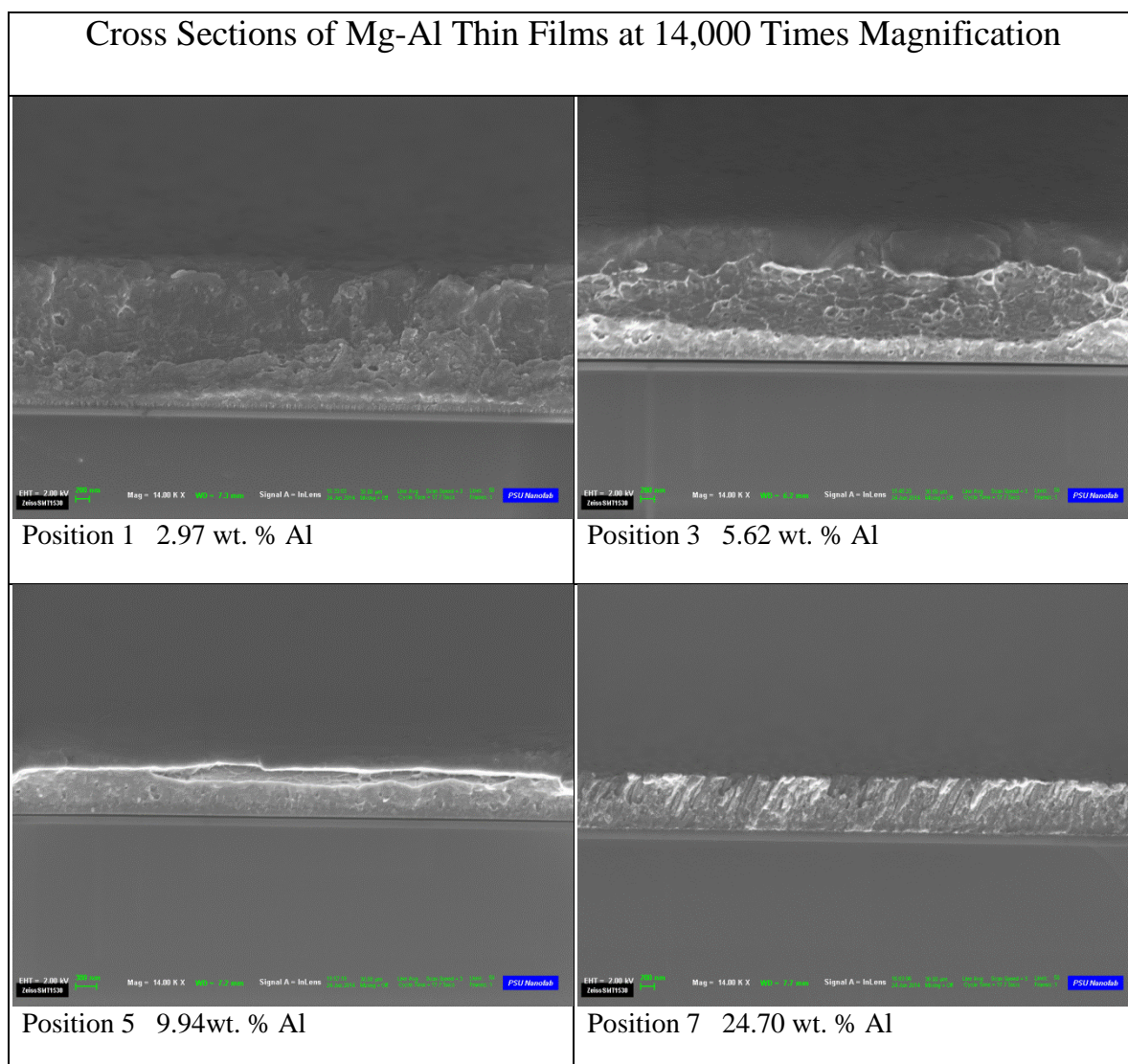
Figure 4-33 FESEM images of the cross section of Mg-Al thin films deposited on 6/11/2014. The image was taken at a 14,000 times magnification and an angle of 10° in order to reveal the surface of the thin film. These images show the dense growth of the Mg-Al binary system. The surface is extremely smooth compared to pure Mg thin films. The effects of the Al in the film can already be seen at just 2.97 wt. % Al.

The X-ray diffraction pattern for Position 1 of the 6/11/2014 runs matches that of an alpha Mg structure with a preferred orientation lining up to the (002) plane (Figure 4-34). It appears that a very small portion of the $Mg_{17}Al_{12}$ phase is present in the film, which is known to show an increased corrosion resistance by enhancing the performance of the passive layer. The diffraction pattern for Position 5 is shown in Figure 4-35. Position 5 is 9.94 wt. % Al and none of the peaks for the alpha Mg phase can be observed in its diffraction pattern. At 9.94% the $Mg_{17}Al_{12}$ phase has dominated the thin film. This result is inconsistent with the diffraction pattern that was collected for Position 1 of the 2/26/2015 thin film that was 18.36 wt. % Al and showed a mixture of the alpha Mg and $Mg_{17}Al_{12}$ phase. This could be a result of different deposition angle for the different positions having an effect on the film growth and structure, which matches the effect of deposition angle on peak height for the pure Mg films. The XRD patterns of Position 1, 3, 5 and 7 are overlaid in Figure 4-36. As the Al content increases there is a decrease in the alpha Mg present in the film and an increase in the $Mg_{17}Al_{12}$ phase. There is a strong preferred orientation of the (721) $Mg_{17}Al_{12}$ peak, in Position 3 and Position 5. The structure for positions 3 and 5 should be similar to the structure of positions 4 and 6 of this deposition, for which we see a large decrease in the open circuit potential compared to other Mg-Al films and low corrosion rates. In future work, the multiple deposition angles should be analyzed for thin films of the same composition in an effort to replicated the same preferred orientation of the (721) $Mg_{17}Al_{12}$ peak and confirm the correlation between this structure and the low open circuit potential.
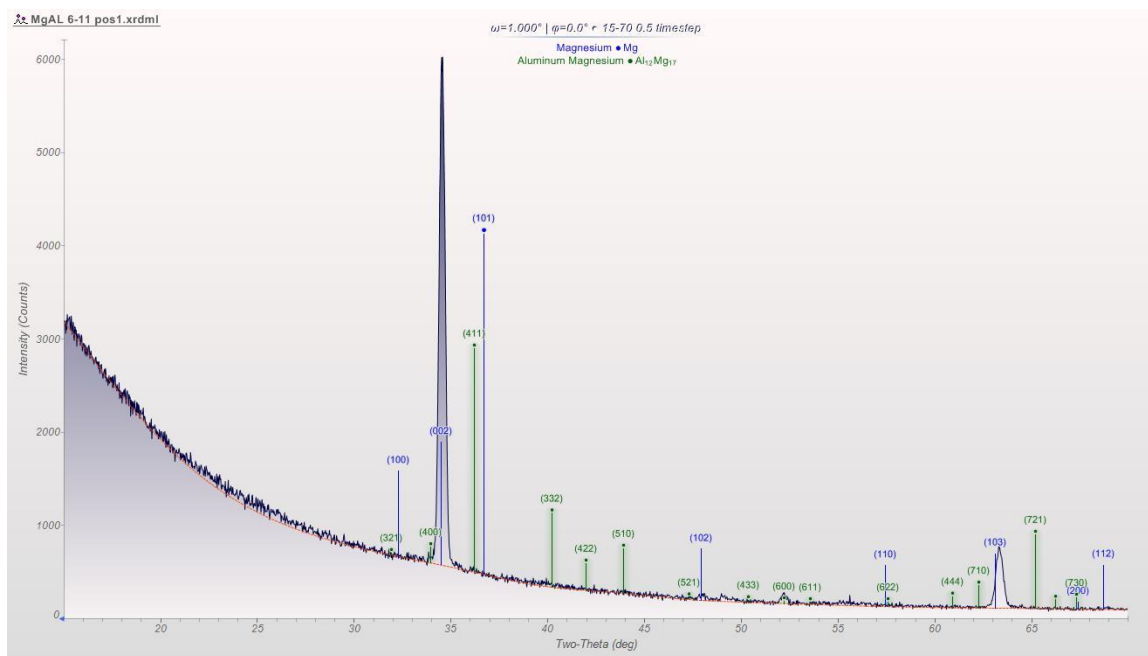
Figure 4-34 XRD Pattern for the 6/11 Position 1 thin film. This film contains 2.97 wt. % Al. The pattern matches the pattern for alpha Mg phase. The Mg₁₇Al₁₂ is also shown and very small peaks for this phase are present.
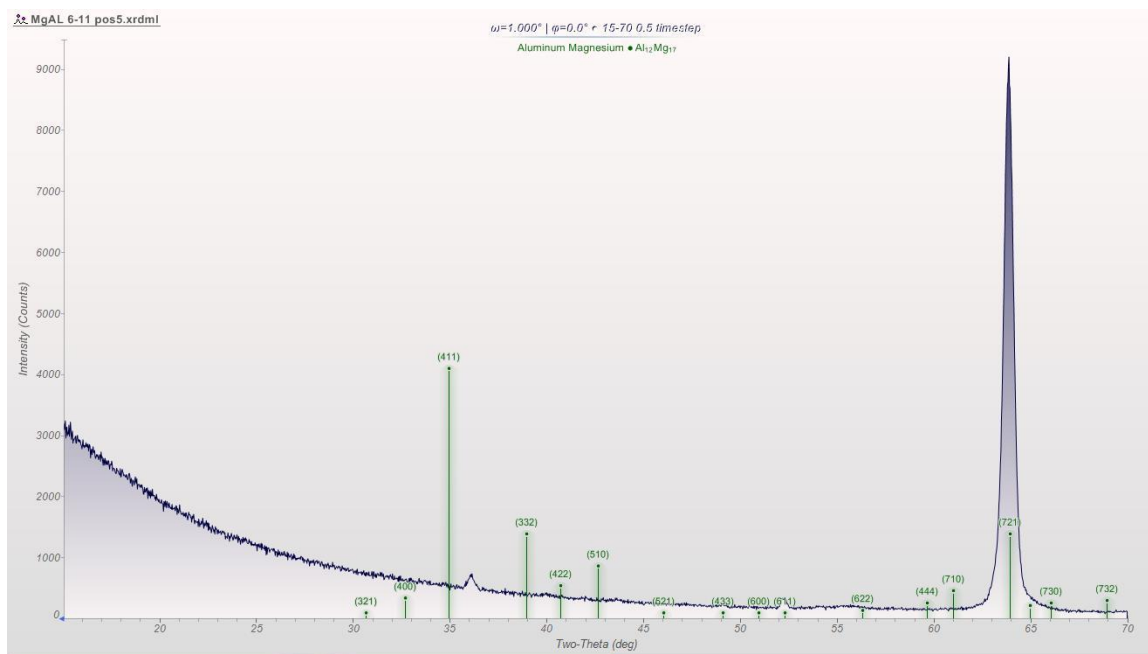
Figure 4-35 XRD Pattern for the 6/11 Position 5 thin film. This film contains 9.94 wt. % Al. The pattern matches the pattern for $Mg_{17}Al_{12}$ phase. The alpha Mg phase does not appear to be present in the film.
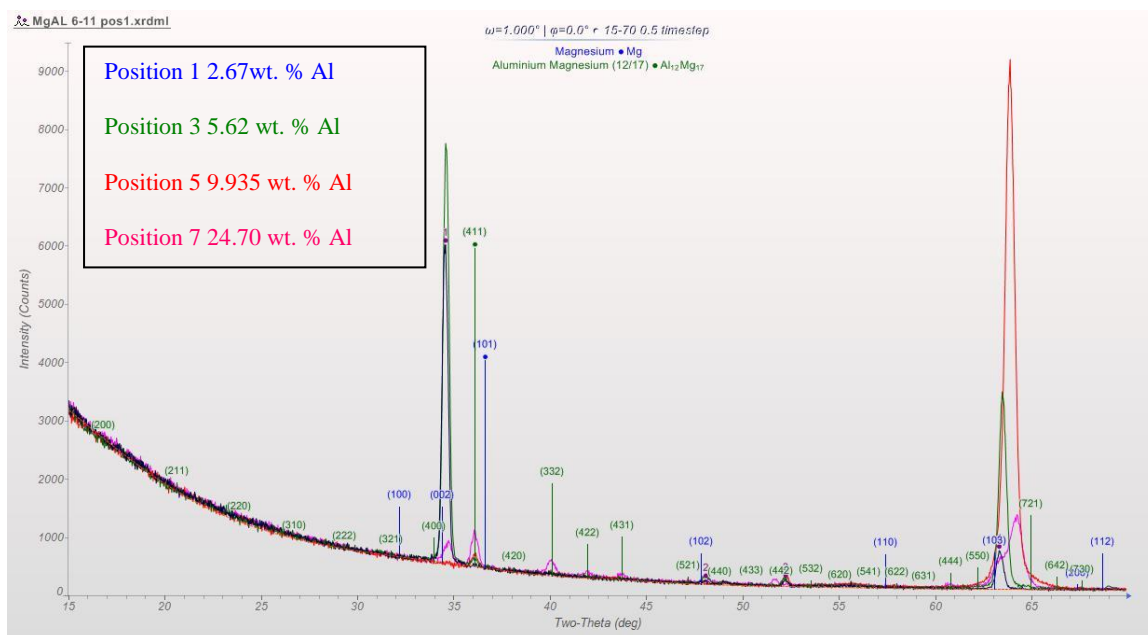
Figure 4-36 XRD Patterns for the 6/11 Mg-Al thin films. The patterns for alpha Mg and $Mg_{17}Al_{12}$ are shown in the figure. With increasing Al content we see a decrease in the (002) alpha Mg peak and an increase in the (721) $Mg_{17}Al_{12}$ peak. The peaks are slightly shifted because of the preferred orientation and probable shift in the lattice constants for the thin films.

4.3.2 Electrochemical Results

For the Mg-Al thin films the corrosion rate is driven by the Al content. With increasing

aluminum content the corrosion rate decreases significantly as shown in Figure 4-37 and Figure

4-38. The highest corrosion rate determined for the Mg-Al films was Position 4 of the 6/11/2014

deposition, which has composition of 8.04 wt. % Al and a corrosion rate of 8.48 mpy determined

by polarization resistance. This is lower than the lowest corrosion rate determined by polarization

resistance for the pure Mg thin films, which was 14.74 mpy for Position 6 of the 12/10/2013

deposition.

Mean Corrosion Rate (PR) of Mg-Al

**Figure 4-37 Plot of the Mean Corrosion Rate values determined by
Polarization Resistance for Mg-Al thin films tested in artificial seawater. This plot
shows Corrosion Rate vs. Weight Percent Aluminum. The corrosion rate decreases
with increasing Al content. The error bars shown are based on a 95% Confidence
Interval. The sample with no error bar had only one electrochemical sample due to
cracking of the thin film.**

Mean Corrosion Rate (EIS) of Mg-Al
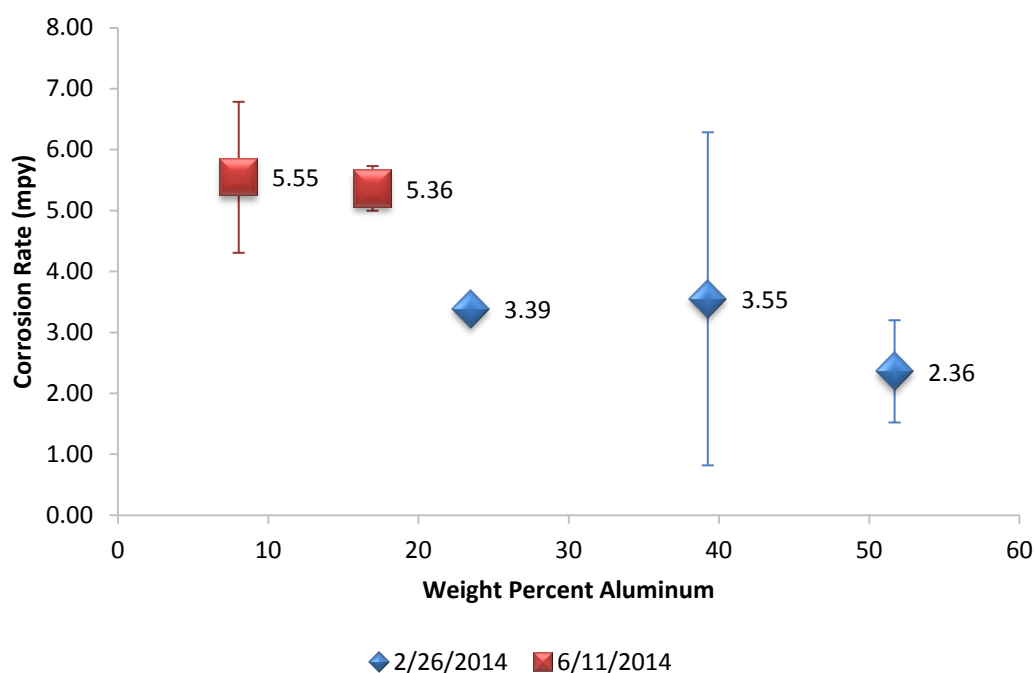
Figure 4-38 Plot of the Mean Corrosion Rate values determined by EIS for Mg-Al thin films tested in artificial seawater. This plot shows Corrosion Rate vs. Weight Percent Aluminum. The corrosion rate decreases with increasing Al content. The error bars shown are based on a 95% Confidence Interval. The sample with no error bar had only one electrochemical sample due to cracking of the thin film.

The corrosion rates determined using EIS are lower than the corrosion rates determined using polarization resistance, but both results support a trend of decreasing corrosion rate with increasing aluminum content. This is due in part to a decrease in surface area resulting from the smooth surface of the Mg-Al films compared to the very rough surface of the pure Mg films and in part to the increased corrosion resistance that the $Mg_{17}Al_{12}$ phase offers. The open circuit potential decreases with increasing deposition angle from Gun 1, which is what was observed for the pure Mg thin films. The open circuit potential values for the 2/26 deposition, which had higher Al content, are higher than the values for the 6/11 deposition. When comparing the open circuit potential values for samples from the same deposition the trend of decreasing open circuit potential with increasing deposition angle can be observed (Figure 4-39). In Figure 4-40 the OCP

is plotted against composition. The plot of OCP vs. Composition is interesting because all of the OCP values fall within 50 mV of -1.575V except for Position 4 and Position 6 which have a significantly lower OCP of -1.829V and -1.856V respectively. The composition for Position 4 is 8.04 wt. % Al and Position 6 is 16.96 wt. % Al. Future work needs to be done to determine why the OCP values for the two samples are so low. Possible reasons are that the effect of deposition angle has lowered OCP value and that with increasing Al content the effect of deposition angle from Gun 1 is diminished. An increase in OCP value with an increase in Al is expected as the OCP for bulk Al alloys is -1.000V and the OCP value of bulk Mg is -1.6V. This is not the trend that is observed in the plot. This implies that the effect of deposition angle is still contributing to the OCP value even at higher Al content.
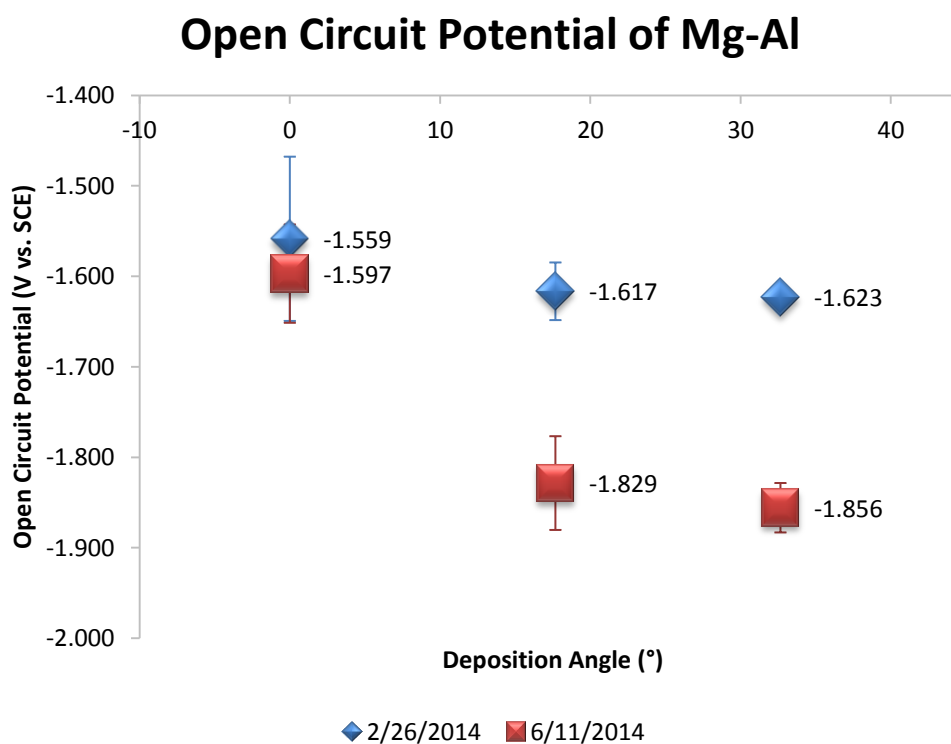
Figure 4-39 Plot of the Open Circuit Potential vs. Deposition Angle values for Mg-Al thin films tested in artificial seawater. This plot shows Open Circuit Potential vs. Deposition Angle. As the deposition angle increases the open circuit potential decreases.

Open Circuit Potential of Mg-Al
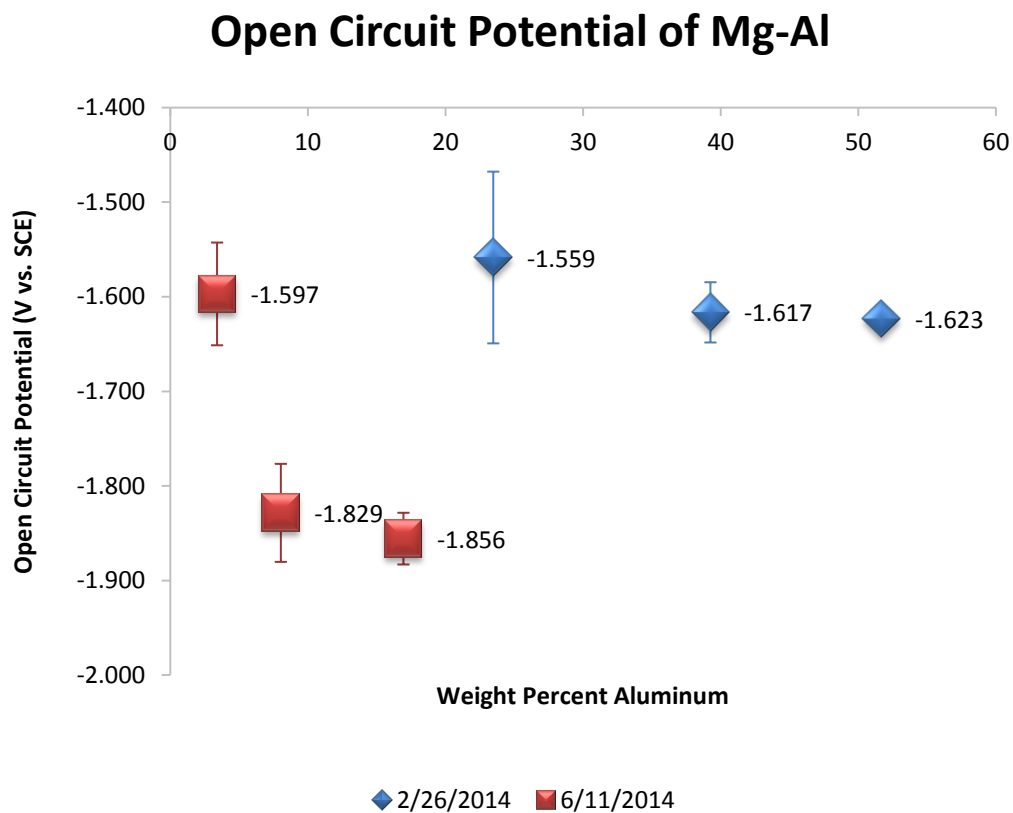
Figure 4-40 Plot of the Open Circuit Potential vs. Weight Percent Aluminum values for Mg-Al thin films tested in artificial seawater. There does not appear to be an overall trend with OCP and aluminum concentration. The trend of decreasing OCP for each deposition set is due to the changes in deposition angle.

4.3.3 Additional Mg-Al Electrochemical Results

To reinforce the trends observed in the previous chapter. Results can be included from work done by Anthony Naccarelli for his Master's Thesis. Data can be provided for two additional Mg-Al thin films that were deposited to lower compositions. The electrochemical data for these runs is presented in Table 4-11.

Table 4-11 Data for Mg-Al depositions. The Table is organized by deposition date and position. Electrochemical tests were performed by Anthony Naccarelli.

Date	10/19/2013			10/24/2013		
Position	2	4	6	2	4	6
Angle	0	17.6	32.6	0	17.6	32.6
Thickness (μm)	2.030	1.720	1.610	2.080	1.810	1.520
Open Circuit Potential (V. vs SCE)	-1.775	-1.778	-1.802	1.640	-1.797	-1.770
Corrosion Rate PR (mpy)	17.740	20.650	18.600	16.630	10.560	10.990
Corrosion Rate EIS (mpy)	10.12	12.26	11.12	8.94	6.94	7.37
wt. % Al Content	1.3	2.5	3.9	1.5	2.5	4.5

The electrochemical results for the 10/19 and 10/24 runs were added to the results presented in section 4.3.2. The plots of all Corrosion Rate vs. Composition for PR and EIS are show in Figure 4-41 and Figure 4-42. For both PR and EIS and decrease in corrosion rate with increasing Al content is observed. For EIS the corrosion rates are lower than those calculated using PR.

Corrosion Rate (PR) vs. Al Content
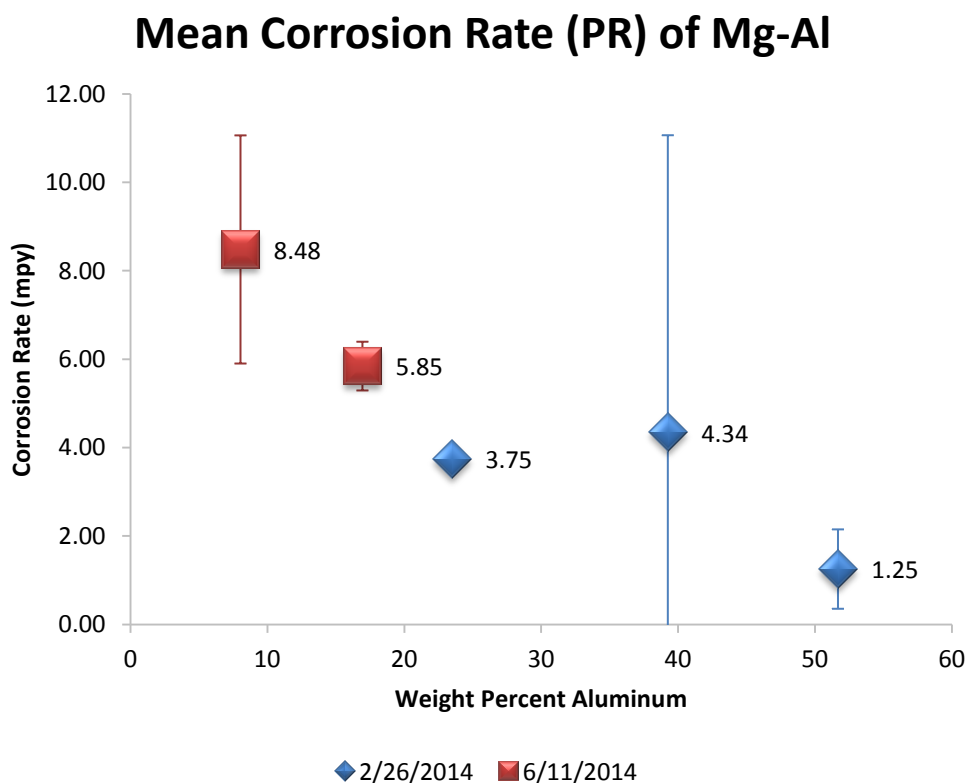## (All Mg-Al Films)
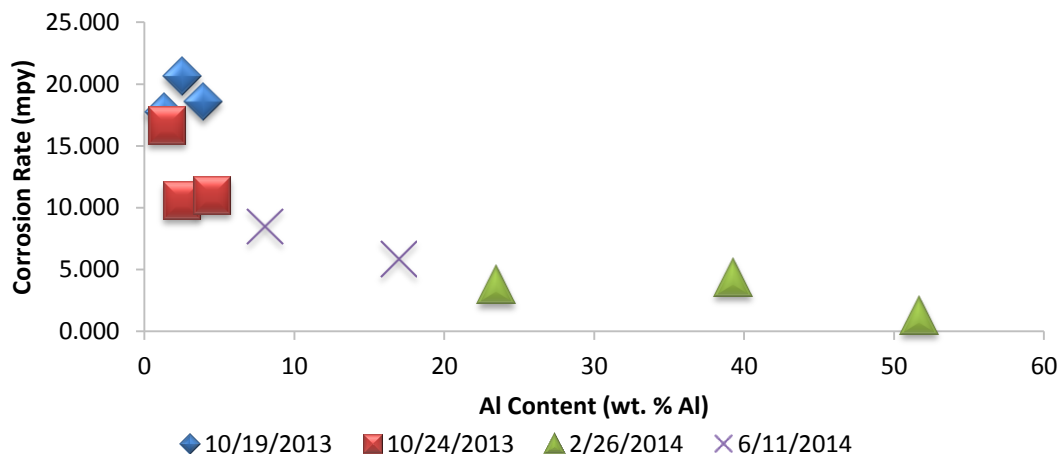
Figure 4-41 Plot of the Mean Corrosion Rate values determined by Polarization Resistance for Mg-Al thin films tested in artificial seawater. This plot shows Corrosion Rate vs. Weight Percent Aluminum. The corrosion rate decreases with increasing Al content.

Corrosion Rate (EIS) vs. Al Content
(All Mg-Al Films)
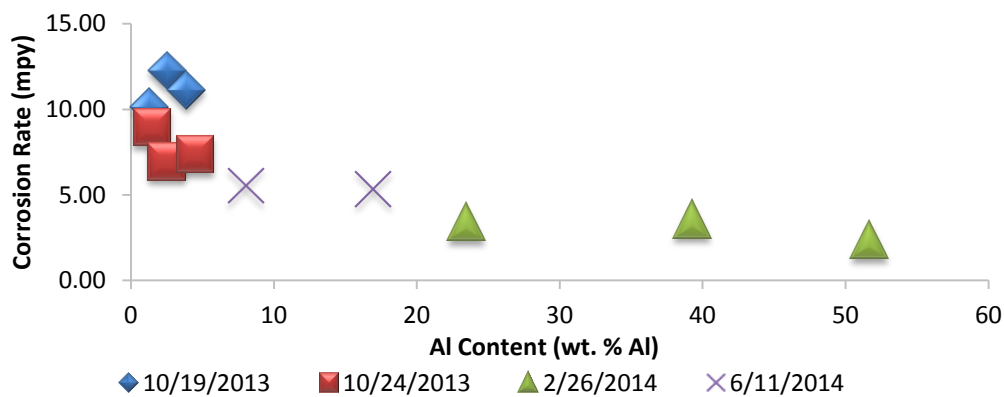
Figure 4-42 Plot of the Mean Corrosion Rate values determined by Electrochemical Impedance Spectroscopy for Mg-Al thin films tested in artificial seawater. This plot shows Corrosion Rate vs. Weight Percent Aluminum. The corrosion rate decreases with increasing Al content.

The Open Circuit Potential vs. Deposition is shown in Figure 4-43. The trend of decreasing OCP with increasing angle can be observed for each deposition run. The decrease ranges from 27mV for the 10/19 deposition to 259mV for the 6/11 deposition. It is impossible to remove the effect of increasing Al content and decrease in deposition rate that is also observed with increasing position and isolate the effect of deposition angle. The effects of deposition angle and composition for Mg-Al thin films needs to be isolated in future work.
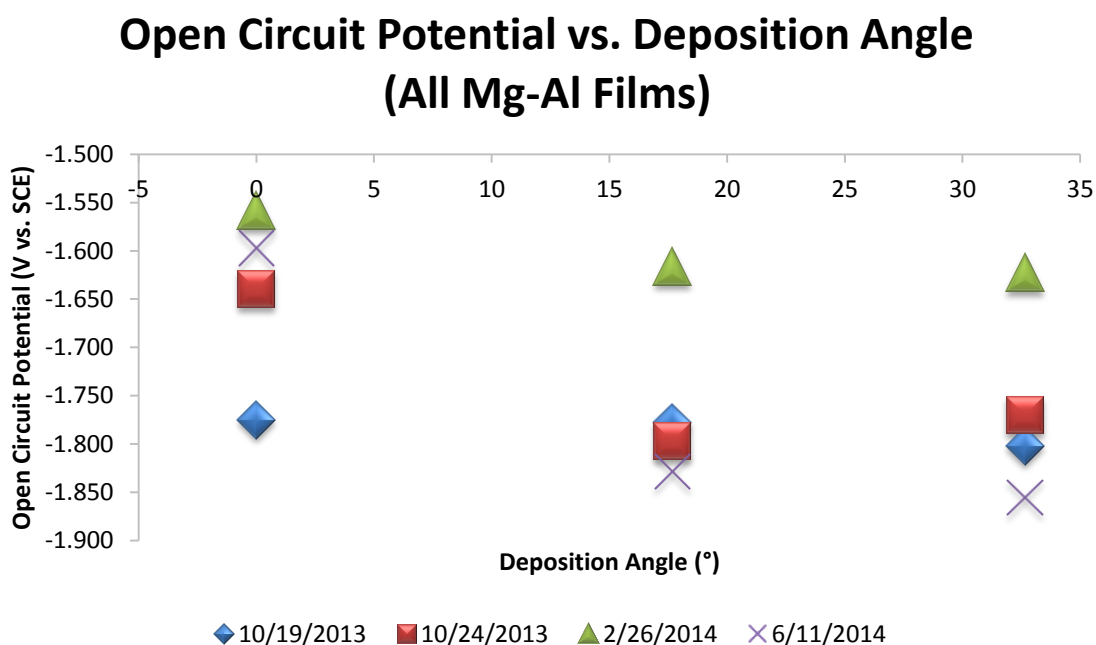
Figure 4-43 Plot of the Open Circuit Potential vs. Deposition Angle values for Mg-Al thin films tested in artificial seawater. This plot shows Open Circuit Potential vs. Deposition Angle. As the deposition angle increases the open circuit potential decreases.

The Open Circuit Potential for all Mg-Al thin films is plotted against composition in Figure 4-44. The trend that is observed is that there is a decrease in open circuit potential with increasing Al content as expected. However, the results from 6/11 Position 4 and Position 6 show a significant drop in open circuit potential compared to the other Mg-Al thin films. Position 4 has an OCP value of -1.829 V and Position 4 has an OCP value of -1.856 V. Both of these values are much lower than the OCP value of Position 2 of the 2/26 run which has an OCP value of -1.559

V and an Al content of 23.48%. The OCP results from the two outlying 6/11 positions are closer to the results thin films with an Al content of less than 5 wt. %, but the corrosion rates of these films are lower. These films break the trend of increasing OCP value with increasing Al content while still exhibiting lower corrosion values (8.48 mpy for Position 4 and 5.85 mpy for Position 6) than lower Al content films (which have corrosion rates ranging from 20.65mpy to 10.56 mpy). Future work should be done in attempt to replicate the 6/11 run. The low open circuit potential and corrosion rate of the 6/11 Position 4 and Position 6 runs are desirable as they allow for the corrosion protection of materials with a higher open circuit potential.

Open Circuit Potential vs. Al Content (All Mg-Al Films)
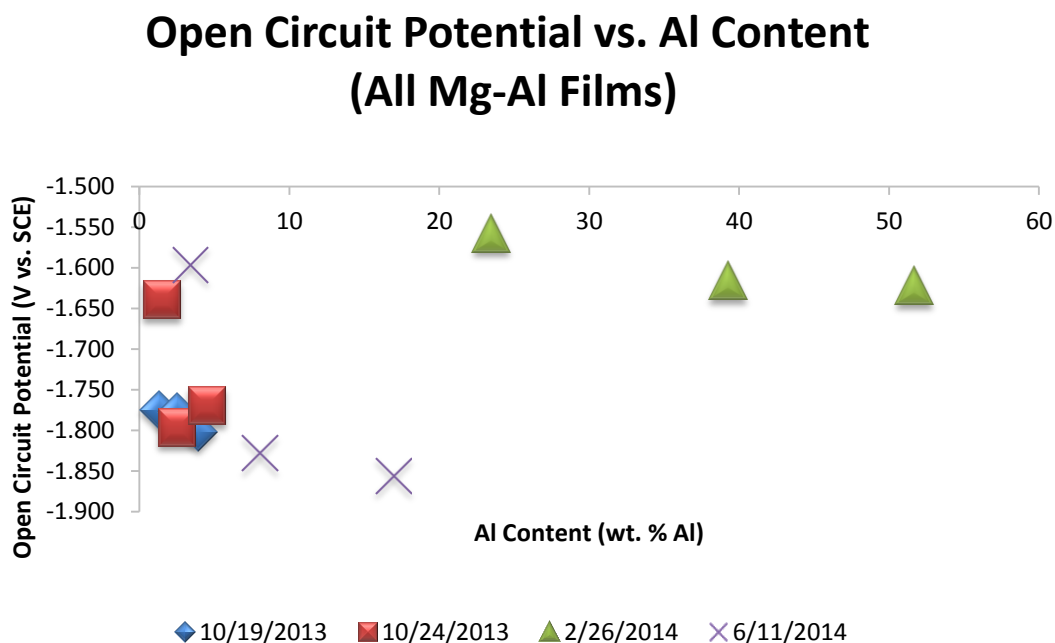
Figure 4-44 Open Circuit Potential vs. Composition. The open circuit potential is higher for higher Al content and lower for lower Al content. It is difficult to identify a trend because it is broken by the two outlying date points from the 6/11/2014 run, which have a lower open circuit potential.

Chapter 5

Summary and Conclusions

The first part of this thesis was devoted to understanding the geometric affects of our particular EBPVD system for both pure materials and for dual-gun alloy deposition. For the deposition calibration, it was found that the thicknesses measured by the surface profilometer were much higher than those measured by the QCM during depositions. The actual thickness was about double the QCM thickness for samples in Position1 and films in Position 7 were often half the thickness of samples in Position 1, for the QCM located over gun 1 which was directly under position 2. Therefore, the actual deposition rate (calculated from the measured thickness) was much higher than what was measured by the QCM during deposition. These trends were consistent for all single gun depositions. The decrease in thickness and deposition rate from Position 1 to Position 7 is due to an increase in deposition distance and deposition angle. Deposition rate is highest at a deposition angle of $0°$ (direction of deposition is normal to the plane of the substrate) and decreases with increasing deposition angle (Table 4-2). These results line up with expectations due to the plume shape of the vapor as described in the cosine model presented in Chapter 3.

For pure magnesium thin films, films deposited at a lower rate (less than 10Å/s) showed a dense structure with thick columnar growth characteristic of zone 2 of the structure zone model as seen by cross-sectional FESEM micrographs (Figure 4-14). These thick columns indicate that surface diffusion occurred during the growth of the film and the films had a preferred orientation to the (002) plane (Figure 4-15). For more rapidly deposited (more than 20Å/s) magnesium thin films narrow, isolated columns were observed to be formed, characteristic of zone 1 of the structure zone model, and a preferred orientation to the (102) plane was observed (Figure 4-16

and Figure 4-17). This implies an increased effect of shadowing and less surface diffusion during growth for films deposited at a high rate. This columnar growth resulted in a rough surface that was not reflective.

For pure magnesium films, there was no observable trend between corrosion rate and deposition rate or film thickness for deposition rates ranging from 9.57 Å/s to 126.6 Å/s and thicknesses ranging from 1.57 μm to 4.11 μm. This means that the corrosion results of films deposited at different rates and to different thicknesses can be compared. Open Circuit Potential of the pure magnesium thin films seemed to decrease with increasing deposition angle (from 0° to 32.6°) and decreasing deposition rate (Figure 4-26 and Figure 4-27). These two trends could possibly enable tailoring of the open circuit potential for a sacrificial layer. This is significant because of the tendency for metals with lower open circuit potential to corrode preferentially when paired with a metal of higher open circuit potential. Thus, the deposited film could act as a sacrificial layer for another metal provided it had the proper open circuit potential. It was also found that a change in deposition angle led to a change in the X-ray spectra collected using GIXRD. As deposition angle increased the size of the (002) peak decreased. It is unclear whether this has any affect on the corrosion properties of the films.

For the Mg-Al binary thin films, it was found that corrosion rate decreased with increasing aluminum content (Figure 4-41 and Figure 4-42). It was also observed that as the aluminum content increased so did the presence of the $Mg_{17}Al_{12}$ phase, which offers enhanced corrosion resistance. Further, the Mg-Al thin films showed a decrease in open circuit potential (of up to 259 mV within a single deposition) with increasing deposition angle measured from Gun 1 (Figure 4-39). We believe this could be related to an effect induced by deposition angle as seen for pure magnesium. This is because the magnesium deposition rate was always at least 4 times higher than the aluminum deposition rate and thus the deposition angle effect would be

dominated by the magnesium deposition. Mg-Al thin films did not show the columnar growth that pure magnesium thin films did. The growth of Mg-Al was dense, even at low Al content, and showed characteristics of zone 3 growth of the structure zone model. It is possible that the change in growth was a result of the increase in deposition temperature that results from the melting of the Al source material. As a result, Mg-Al thin films appeared to be much denser and had very smooth, reflective surfaces.

The samples from Position 4 and Position 6 of the 6/11 deposition had the lowest open circuit potentials of any Mg-Al thin films with open circuit potentials of -1.829 V and -1.856 V respectively. These films also showed low corrosion rates of 8.48 mpy for Position 4 and 5.85 mpy for Position 6. These electrochemical characteristics are desirable for a protective coating as the low open circuit potential will cause the film to corrode preferentially to materials with higher open circuit potential.

Chapter 6

Future Work

Analysis of our experimental evaporation system and subsequent deposition of pure magnesium and magnesium/aluminum alloy films showed some interesting results with respect to deposition position in the chamber. In addition, new information was gained on the relationship of deposition rate and film thickness to corrosion properties, stoichiometry and crystal structure for these films. However, this research also raised a number of new questions that were beyond the scope of this thesis. Following are some suggestions for additional research that would supplement what has been presented in this work.

- In the future, it would be illuminating to conduct experiments that isolate deposition distance, deposition angle and deposition rate. In this work, the deposition angle, deposition distance and deposition rate were linked because of the method used to mount the substrates in the chamber. One simple experiment would be to construct a holder that would keep all substrates perpendicular to the source material and at the same distance. Then, only the disparity in rate caused by the cosine distribution would affect the film thickness. This could be evaluated for different deposition rates. This would only be useful for single composition films.

- ICP analysis should be performed on pure Mg films to see if the decrease in open circuit potential is due to a decrease in impurities as a result of deposition angle or distance. Further, an even more sensitive technique such as secondary ion mass spectroscopy might be used to evaluate impurity concentration.

- It would be valuable to design experiments that account for the substrate temperature during deposition. The temperature was assumed to be at ambient temperature for all of the depositions performed in this work. In reality, the melting of aluminum raises the temperature in the chamber. This could have a significant effect on the growth of the thin films and could be a factor in the observed dense growth of the Mg-Al thin films in this research.

- Mg-Al thin films of the same composition should be deposited at different distance and deposition angles to isolate the geometric effects from the effect of composition.

- It would be enlightening to measure the surface roughness of deposited films in order to accurately compare the surface areas and corrosion rates of thin films.

- Quantitative analysis from XRD could allow for the determination of the concentration of phases present within a thin film sample, which could then be potentially correlated with corrosion characteristics such as OCP or corrosion rate.

Works Cited

1] B. L. Mordike and T. Ebert, "Magnesium Properties — applications — potential," *Materials Science and Engineering,* vol. 302, pp. 37-45, 2001.

2] K. Guo, "A review of magnesium/magnesium alloys corrosion and its protection," *Recent Patents on Corrosion Science,* vol. 2, pp. 13-21, 2010.

3] E. Ghali, "General and Localized Corrosion of Magnesium Alloys: A Critical Review," *Journal of Materials Engineering and Performance,* vol. 13, no. 1, pp. 7-23, 2004.

4] G. Hamu, D. Eliezer, W. Dietzel and K. Shin, "Stress corrosion cracking of new Mg-ZnMn wrought alloys containing Si.," *Corrosion Science,* vol. 50, pp. 1505-1517, 2008.

5] "Properties of Pure Metals, Properties and Selection: Nonferrous Alloys and Special-Purpose Materials," *ASM Handbook,* vol. 2, pp. 1099-1201, 1990.

6] Z. Rong-chang, Z. Jin, H. Wei-Jiu, W. Dietzel, K. U. Krainer, C. Blawert and K. Wei, "Review of studies on corrosion of magnesium alloys," *Transactions of Nonferrous Metals Society of China,* vol. 16, pp. 763-771, 2006.

7] C. Olk and D. Haddad, "Growth and Characterization of a Combinatorial Array of Mixed-Phase Magnesium-Aluminum Thin-Film Alloys," *MRS Proceedings,* vol. 1056, 2007.

8] K. Appusamy, S. Blair and A. Nahata, "Low-loss magnesium films for plasmonics," *Materials Science and Engineering: B,* vol. 181, no. D, pp. 77-85, 2014.

C. Blawert, D. Manova and M. Stormer, "Correlation between texture and corrosion
9] properties of magnesium coatings produced by PVD," *Surface and Coatings Technology,*
vol. 202, no. 11, pp. 2236-2240, 2008.

S. M. Pursel, J. D. Petrilli, M. W. Horn and B. A. Shaw, "Effect of alloy addition
10] and growth conditions on the formation of Mg- based bioabsorbable thin films,"
Nanostructured Thin Films, vol. 7041, pp. 704113-1 - 704113-11, 2008.

M. Stormer, C. Blawert, H. Hagen, V. Heitmann and W. Dietzel, "Structure and
11] Corrosion of Magnetron Sputtered Pure Mg Films on Silicon Substrates," *Plasma Processes
and Polymers,* vol. 4, no. S1, pp. S557-S561, 2007.

Y. He and Y. Zhao, "Mg Nanostructures Tailored by Glancing Angle Deposition,"
12] *Crystal Growth & Design,* vol. 10, no. 1, pp. 440-448, 2010.

J. A. Thornton, "Structure-Zone Models Of Thin Films," *SPIE Proceedings,* vol. 95,
13] p. 0821, 1988.

CRC Handbook of Chemisty and Physics, 94th edition, CRC Press, 2013.
14]

T. D. Kelly and G. R. Matos, "Historical statistics for mineral and material
15] commodities in the United States," U.S. Geological Survey Data Series, 2013. [Online].
Available: http://minerals.usgs.gov/ds/2005/140/. [Accessed 23 September 2013].

"Properties of Pure Metals," *ASM Handbook,* vol. Vol 2, p. 1099–1201, 1990.
16]

X. Yu-Qing, L. Xing-Cun, C. Qiang, L. Wen-Wen, Z. Qiao and S. Li-Jun,
17] "Characteristics and properties of metal aluminum thin films prepared by electron cyclotron
resonance plasma-assisted atomic layer deposition technology," *Chinese Physics B,* vol. 21,

no. 7, p. 078105, 2012.

A. J. Learn, "Evolution and current status of aluminum metallization," *Journal of*
18] *The Electrochemical Society,* no. June, pp. 894-906, 1976.

H.Friedrich and S. Schumann, "Research for a "new age of magnesium" in the
19] automotive industry," *Journal of Materials Processing Technology,* vol. 117, no. 3, pp. 276-
281, 2001.

S. Kleiner, E. Ogris, O. Beffort and P.J.Uggowitzer, "Semi-Solid Metal Processing
20] of Aluminum Alloy A356 and Magnesium Alloy AZ91: Comparison Based on Metallurgical
Consideration," *Advanced Engineering Materials,* vol. 5, no. 9, pp. 653-658, 2003.

B. Smola, I. Stulikova, F. v. Buch and B. Mordike, "Structural aspects of high
21] performance Mg alloys design," *Materials Science and Engineering A,* vol. 324, no. 1-2, pp.
113-117, 2002.

O. Lunder, "Effect of Mn Additions on the Corrosion Behavior of Mould-Cast
22] Magnesium ASTM AZ91," *Corrosion,* vol. 43, no. 5, p. 291, 1989.

S. Cho, B. Chun, C. Won, S. Kim, B. Lee and H. Baek, "Structure and properties of
23] rapidly solidified Mg-Al alloys," *Journal of Materials Science,* vol. 4, pp. 4311-4320, 1999.

S. Cai, T. Lei, N. Li and F. Feng, "Effects of Zn on microstructure, mechanical
24] properties and corrosion," *Materials Science and Engineering C,* vol. 32, pp. 2570-2577,
2012.

I. Fuke, V. Prabh and S. Baek, "Computational Model for Predicting," *Journal of*
25] *Manufacturing Processes,* vol. 7, no. 2, 2005.

D. e. Newbury and W. M. Ritchie, "Is Scanning Electron Microscopy/Energy
26] Dispersive X-ray," *Scanning,* vol. 35, pp. 141-168, 2013.

N. Ritchie, D. Newbury and J. Davis, "EDS measurements of X-ray intensity at
27] WDS precision and accuracy using a silicon drift detector," *Microsc Microanalysis,* 2012.

V. Scott and G. Love, Quantitative Electron Probe Microanalysis, 2nd Edition,
28] Chichester: Ellis Horwood, 1994.

E. Sikora, X. Wei and B. Shaw, "Corrosion Behavior of Nanocrystalline Bulk Al-
29] Mg-Based Alloys," *The Journal of Science and Engineering Corrosion,* vol. 60, no. 4, pp.
387-398, 2004.

Appendix A Thin Film EDS Data

Material	Date Deposited		Position 1	Position 2	Position 3	Position 4	Position 5	Position 6	Position 7
Mg-Al	2/26/2014	wt. % Mg-raw-a	80.2	74.93	72.04	59.97	55.26	46.31	40.33
		wt. % Mg-raw-b	79.73	74.94	71.83	58.82	55.39	47.17	39.52
		wt. % Mg-raw-avg	79.965	74.935	71.935	59.395	55.325	46.74	39.925
		wt. % Al-raw-a	17.61	22.85	26.21	37.97	42.23	50.04	56.94
		wt. % Al-raw-b	18.35	23.16	26.63	38.83	42	50.02	56.61
		wt. % Al-raw-avg	17.98	23.005	26.42	38.4	42.115	50.03	56.775
		wt. % Al/% Mg-ratio	0.224848	0.306999	0.367276	0.646519	0.761229	1.070389	1.422041
		wt. % Al-quantitative	18.35724	23.4888	26.8618	39.2658	43.2214	51.6999	58.7125
		at. % Al-quantitative	16.33938	21.0523	24.1861	35.9619	39.8029	48.1798	55.2612
Mg-Al	6/11/2014	wt. % Mg-raw-a	97.05	96.57	94.48		90.07		75.23
		wt. % Mg-raw-b	97.02	96.62	94.28	91.96	90.06	83.05	
		wt. % Mg-raw-avg	97.035	96.595	94.38	91.96	90.065	83.05	75.23
		wt. % Al-raw-a	2.95	3.43	5.52		9.93	16.95	24.68
		wt. % Al-raw-b	2.98	3.38	5.72	8.04	9.94		
		wt. % Al-raw-avg	2.965	3.405	5.62	8.04	9.935	16.95	24.68
		wt. % Al/% Mg-ratio	0.030556	0.03525	0.05954	0.08742	0.11030	0.20409	0.32806
		wt. % Al-quantitative	2.965	3.405	5.62	8.04	9.935	16.95	24.7022
		at. % Al-quantitative	2.286168	2.53704	4.16060	5.57287	6.81395	11.6380	17.2124

Appendix B Thin Film Electrochemical Data

Pure Magnesium Thin Films

Date	12/4/2013			12/10/2013			10/15/2013		
Position	2	4	6	2	4	6	2	4	6
Thickness (μm)	2.68	2.35	1.57	2.29	2.11	2.04	3.33	4.11	3.66
Deposition Rate (Å/s)	127.4	111.67	74.81	10.62	9.75	9.45	42.68	52.71	46.89
Open Circuit Potential (V. vs. SCE)	-1.690	-1.780	-1.820	-1.806	-1.840	-1.902	-1.608	-1.845	-1.900
Corrosion Rate PR (mpy)	22.57	15.41	19.78	18.76	24.70	14.74	318.40	30.51	18.60
Corrosion Rate EIS (mpy)	19.32	11.74	11.67	11.32	12.81	9.10	78.20	19.18	15.19

Mg-Al Thin Films

Date	2/26/2014			6/11/2014		
Position	2	4	6	2	4	6
Angle	0	17.676	32.654	0	17.676	32.654
Thickness (μm)	1.868	1.636	1.339	1.979	1.400	0.865
Deposition Rate (Å/s)	34.58	30.30	24.79	32.98	23.33	14.42
Open Circuit Potential (V. vs SCE)	-1.559	-1.617	-1.623	-1.597	-1.829	-1.856
OCP 95% CI	0.090777	0.031849	0.00196	0.054	0.052	0.027
Corrosion Rate PR (mpy)	3.75	4.34	1.25		8.48	5.85
PR 95% CI		6.723957	0.897963		2.58	0.55
Corrosion Rate EIS (mpy)	3.39	3.55	2.36		5.55	5.36
EIS 95% CI		2.733755	0.839214		1.239035	0.366582
wt. % Al Content	23.48	39.26	51.69	3.405	8.04	16.95

Date	10/19/2013			10/24/2013		
Position	2	4	6	2	4	6
Angle	0	17.6	32.6	0	17.6	32.6
Thickness (μm)	2.030	1.720	1.610	2.080	1.810	1.520
Open Circuit Potential (V. vs SCE)	-1.775	-1.778	-1.802	1.640	-1.797	-1.770
Corrosion Rate PR (mpy)	17.740	20.650	18.600	16.630	10.560	10.990
Corrosion Rate EIS (mpy)	10.12	12.26	11.12	8.94	6.94	7.37
wt. % Al Content	1.3	2.5	3.9	1.5	2.5	4.5